# Biocompatibility – Mechanical Property – Microstructure Relationship in Conventional and Potential Biomedical Alloys

**by**

**Sıdıka Mine Toker**

**A Thesis Submitted to the**
**Graduate School of Sciences and Engineering**
**in Partial Fulfillment of the Requirements for**
**the Degree of**

**Doctor of Philosophy**
**in**
**Mechanical Engineering**

**Koç University**

**August 2014**

Koç University

Graduate School of Sciences and Engineering

This is to certify that I have examined this copy of a Ph.D. thesis by

Sıdıka Mine Toker

and have found that it is complete and satisfactory in all respects,
and that any and all revisions required by the final
examining committee have been made.

Committee Members:

_____

Demircan Canadinç, Ph.D. (Advisor)

_____

Erdem Alaca, Ph.D.

_____

Özgür Birer, Ph.D.

_____

Seda Kızılel, Ph.D.

_____

Burç Mısırlıoğlu, Ph.D.

Date: 08.08.2014

**ABSTRACT**

The aim of the work presented herein is to investigate the biocompatibility – mechanical property – microstructure relationship in conventional and potential biomedical alloys. For this purpose, well known and potential biomedical alloys were analyzed in terms of the aforementioned parameters by constructing a relationship between them, and the gained knowledge was also partially extended to structural materials.

Initially, biocompatibility of NiTi shape memory alloys (SMAs) was investigated in relation to alloy geometry and body location dependency. In this analysis, it was observed that different alloy geometries yield different surface properties due to the particular processing route applied to obtain a certain geometry, which affects biocompatibility response of the alloy. Moreover, each geometry appeared to be safer for a different body location, showing that biocompatibility response of NiTi SMAs vary depending on alloy geometry, surface properties and body location. Next, biocompatibility of a NiTi SMAs used for a different application, NiTi orthodontic archwires was analyzed, with a focus on the evaluation of the biocompatibility testing method of NiTi orthodontic archwires, by comparing *ex situ* tested archwires with the ones retrieved from patients. The outcomes of this analysis evidence the importance of incorporation of actual loading conditions into *ex situ* experiments for a more realistic biocompatibility testing procedure. In order to incorporate actual mechanical conditions into the *ex situ* testing of NiTi orthodontic archwires, an archwire bound to brackets on a dental mold was also tested *ex situ* and compared to an *ex situ* tested undeformed wire. The results of this set of experiments indicated that actual loading conditions that orthodontic archwires are normally subjected to can be successfully simulated by providing wire-bracket contact in *ex situ* experiments and the wire-bracket contact sites constitute critical points for the nucleation of corrosion products due to the stress concentration and stress assisted corrosion created at these locations.

As the biocompatibility analysis on NiTi SMAs demonstrated, surface properties, microstructure and mechanical loading conditions constitute important parameters for determining the biocompatibility response of metallic biomaterials. For further investigating the microstructure – mechanical property relationship and its correlation to biocompatibility, mechanical deformation response of a potential biomedical alloy, namely the NbZr alloy, was examined under impact loading for various microstructures, specifically for various degrees of anisotropy. This analysis demonstrated that impact response of metallic materials, which constitutes a critical type of mechanical loading condition for implants, strongly depend on microstructural properties. In order to further clarify the role of microstructure on the impact response of metallic materials, the impact behavior of a structural metallic material, namely a high-manganese austenitic steel was investigated. The reason for the preference of this type of alloy was its complex microstructure with intense slip-twin interactions. The outcomes of this investigation indicated that under impact loading, either slip or twin mechanism gets activated, unlike the slip-twin interactions that normally dominates deformation under conventional modes of loading. This behavior is attributed to the unusually high deformation rate of this type of loading and presented guidelines for the understanding of the role of each microstructural mechanism on the deformation response of metallic materials.

Overall, the findings of the current thesis emphasize the importance of analyzing the biocompatibility-microstructure-mechanical property relationship for a successful assessment of biocompatibility of biomaterials. Moreover, the work presented herein clearly demonstrates that adopting the corresponding knowledge to the design procedure of new biomedical applications is of utmost importance for the safety of patients.

## ÖZET

Burada sunulan çalışmanın amacı, geleneksel ve potansiyel biyomedikal alaşımlarda, biyouyumluluk-mekanik özellik-mikroyapı ilişkisini incelemektir. Bu amaçla, bilinen ve potensiyel biyomedikal alaşımlarda bu özellikler, aralarında bağlantı kurularak incelendi ve elde edilen bilgiler yapısal metalik malzemelerin davranışlarının anlaşılmasında da faydalı oldu.

Öncelikle, şekil bellekli Nikel-Titanyum (NiTi) alaşımlarının biyouyumlulukları, geometri ve vücut bölgesine olan bağlantısı açısından incelendi. Bu analizde, farklı geometrilerin, o geometriyi elde etmek için uygulanan işleme yöntemine bağlı olarak farklı yüzey özellikleri gösterdikleri ve bunun alaşımın biyouyumluluğunu etkilediği gözlendi. Ayrıca, her geometrinin farklı bir vücut bölgesi için daha uygun olduğu, bu bulgunun da NiTi şekil bellekli alaşımlarının biyouyumluluk davranışının, alaşımın geometrisi, yüzey özellikleri ve vücut bölgesine bağlı olarak değiştiğini gösterdiği tespit edildi. Bunun ardından, farklı bir uygulama için kullanılan NiTi şekil bellekli alaşımlar olan, NiTi ortodontik tellerin biyouyumlulukları, NiTi ortodontik tellerin biyouyumluluk test yönteminin değerlendirmesi üzerinde durularak, *ex situ* test edilen tellerle hasta ağzından çıkan tellerin kıyaslanması ile incelendi. Bu analizin sonuçları, gerçek yükleme koşullarının *ex situ* deneylere katılmasının, daha gerçekçi biyouyumluluk testi uygulamaları açısından önemini ortaya koydu. Gerçekçi mekanik koşulların NiTi ortodontik tellerin *ex situ* test edildiği ortamda simüle edilebilmesi için, bir ortodontik tel bir diş modeli üzerinde braketlere bağlanarak ayrıca *ex situ* olarak test edildi ve *ex situ* test edilen deforme edilmemiş bir tel ile kıyaslandı. Bu deneylerin sonuçları, ortodontik tellerin normalde maruz kalacağı gerçek yükleme koşullarının, *ex situ* deneylerde tel-braket teması sağlanarak başarılı biçimde simüle edilebileceğini ve tel-braket temas noktalarının, bu bölgede oluşan gerilim yoğunluğu ve gerilime bağlı korozyon sebebiyle, korozyon ürünlerinin birikmesi için kritik noktalar oluşturduğunu gösterdi.

NiTi şekil bellekli alaşımlar üzerinde yapılan biyouyumluluk analizlerinin gösterdiği üzere, yüzey özellikleri, mikroyapı ve mekanik yükleme koşulları, metalik biyomalzemelerin biyouyumluluklarının belirlenmesi açısından önemli değişkenlerdir. Mikroyapı-mekanik özellik ilişkisinin daha ileri düzeyde incelenmesi ve biyouyumlulukla aralarında bağlantı kurulması için, devam eden incelemelerde, potensiyel bir biyomedikal alaşım olan Niobyum-Zirkonyum (NbZr) alaşımının darbe yükleri altındaki mekanik davranışı, farklı derecede anizotropi derecelerine sahip mikroyapısal durumlar için incelendi. Bu analiz, implant malzemeleri için kritik bir mekanik davranış durumu olan metalik malzemelerin darbe yükü altındaki davranışının mikroyapısal özelliklere son derece bağlı olduğunu gösterdi. Mikroyapının metalik malzemelerin darbe davranışı üzerindeki rolünün daha ayrıntılı açıklanabilmesi için, yapısal bir metalik malzeme olan bir yüksek manganezli östenitik çelik türünün darbe davranışı incelendi. Bu alaşım türünün seçilmesinin sebebi, içindeki yoğun kayma ve ikizleme mekanizmaları etkileşimleri nedeniyle sahip olduğu karmaşık mikroyapı idi. Bu incelemenin bulguları, geleneksel yükleme modları altındaki davranışı domine eden kayma-ikizleme etkileşimlerinden farklı olarak, darbe yüklemesi altında kayma veya ikizleme mekanizmalarından yalnız birinin aktive olduğunu gösterdi. Bu davranış, bu yük tipi altında oluşan olağandışı deformasyon hızına bağlandı ve her bir mikroyapısal mekanizmanın metalik malzemelerin deformasyon davranışında olan rolünün anlaşılması açısından önemli bilgiler sağladı.

Sonuç olarak bu tezde sunulan sonuçlar, biyouyumluluk-mikroyapı-mekanik özellik ilişkisinin incelenmesinin biyomalzemelerde başarılı bir biyouyumluluk analizi yapmak açısından önemli olduğunu göstermektedir. Ayrıca, söz konusu bilgi birikiminin biyomedikal uygulamaların tasarım aşamasında kullanılmasının, hasta güvenliğini arttıracağı açıkça görülmektedir.

**Dedicated to my family…**

**ACKNOWLEDGEMENTS**

First of all, I would like to thank my advisor, Dr. Demircan Canadinç, for his precious guidance and continuous support throughout this thesis. With his open-minded and creative approach and deep knowledge, I was able to learn and contribute much more than I could imagine during my thesis work. Through his trust in me and his continuous encouragement, the whole PhD procedure got much easier for me. He was not only a great advisor in terms of research, but also the coolest mentor to give the best advices about any issue in life. Moreover, as he definitely knows how to bring in fun to research, we, as a group, had the chance to have the best times during our PhDs, unlike the painful procedure described by many others. I feel so lucky to have known Dr. Canadinç, not only as my thesis advisor, but also as a person who has been a great inspiration and became another brother to me.

I would like to express my gratitude to my thesis progress supervision committee members; Dr. Erdem Alaca and Dr. Özgür Birer for their valuable comments and guidance throughout my thesis. I would like to thank Dr. Özgür Birer once more for his collaboration with us, his experimental support and valuable contributions to this work. I also would like to express my appreciation to all my dissertation committee members; Dr. Demircan Canadinç, Dr. Erdem Alaca, Dr. Özgür Birer, Dr. Seda Kızılel and Dr. Burç Mısırlıoğlu for their participation.

I am very grateful to Dr.-Ing Hans Jurgen Maier, for letting me visit his research groups both in Paderborn and Hannover. I learned a lot from him and his groups and I feel very lucky to have the chance to join this international research. I also would like to thank Dr. Gregory Gerstein for his valuable TEM observations and contributions to this research and his friendly attitude during my visit to Hannover. I also would like to thank our dentist collaborators; Dt. Damla Şahbazoğlu and (my dear cousin and dentist) Dt. Doruk Şaher for their contributions.

It is very hard to describe how lucky I have been to work in Advanced Materials Group (AMG) and have the best memories one could ever hope for during a PhD. First of all, I would like to thank once more to my advisor Dr. Canadinç for building this sincere and friendly environment in our group. As each of our group members is a unique character, I would like to thank every AMG member one by one. I would like to start by thanking Berkay Gümüş, "kardeşim, Berçut, Berkut" the guy who knows everything and more. My whole PhD procedure would be much harder if I wasn't able to ask him "literally" everything. His presence, support and true friendship mean a lot to me. I also feel very lucky to have known Burak Bal, "atkuşcuğum", as he is one the most interesting persons I ever met. Although our personal perspectives about the basic things in life conflicted sometimes, his presence in our lab made it so much fun, and I am very thankful to him for his friendship. Benay Uzer, "Benoyumumm" the source of excitement, enthusiasm and appetite in our lab, also brought joy into our group with her sincerity and friendship, which I truly appreciate. I am grateful for the sincere friendship of Cemre Özmenci, "Cemreaaa" the creative mind and the dreamer in our lab. I am sure we will altogether visit Cuba someday, thanks to her efforts. I am thankful to the AMG girls also for bringing a "girl union" into our lab. "We can do it!" I would like to thank Morad Mirzajanzadeh, a true "babiş" with his politeness and thoughtful attitudes and his great ability to teach us the Azerbaijani language. He has been a great friend. Finally, I would like to thank Orkun Önal, my first officemate, for his friendship. I will miss the incredible environment in our office and I am already looking forward to the AMG reunion. I also would like to thank the honorary members of our group, Seda Canadinç and Nazik Öğretmen, for their valuable friendship and being a part of AMG.

Having a peaceful home in Istanbul was also one of the most fortunate things I came across during my PhD. For that, I first of all would like to thank "pıtırcığım" Ayşen Sarıoğlu, my first friend and roommate at Koç University. We spent two great years with numerous

memories both at home and school, thanks to her devoted, determined, fun and yet "dramatic" personality. During these four years, I was fortunate enough to meet another perfect roommate and a really unique and great person, "Işınsüdü", Işınsu Baylam. Through our distinct conversations, fantastic home rituals (like Behzat Ç. Nights) and unusual eating habits, we reached a whole new level of communication, which may sound meaningless when listened from outside. But it was what made our time together unforgettable and incredibly fun. I am so grateful to Ayşen, Işınsu and all my other and former roommates, Begüm Akalın and Tuğba Öztürk for making me feel home all this time. Finally, I would like to thank the joy of our home, the last one to join us, our beloved cat: Behzat K. He is the toughest, yet the most distinctive personality I've ever met. His incredibly warm and soft presence and his unbelievably smart and abrupt movements, which are probably a challenge to the whole cat community, brought great happiness and joy into my life. Thank you for being our cat Behzat.

Beyond our office and home, I was fortunate to meet great people from the Koç University staff. I would like to express my appreciation to Songül Abla, Türkan, Derya Abla, Emine Hanım, Elif Hanım, Gözde and Hacer Abla, for all their help and friendliness through these four years.

I have always been lucky to have great friends since my childhood and I am so grateful that they were still around me throughout my PhD. I would like to thank Burcu Azapoğlu, Gülen Göktürk, Gülce Çınar, Birsu Aydoğdu, Gözde Alkan and Hande Bozkurt for their presence, support in any area of my life and their precious friendship ever since we were 12. Experiencing a whole new level of life, becoming "partially" adults and starting to explore new places around the world together were new and invaluable memories for me, which made my PhD procedure a lot easier and more fun. I am very thankful to them and to all my other MPAL friends for being there.

I also would like to thank two other old friends from undergrad, Ercüment Moralı and Hasan Sarıoğlu, for their friendship and especially Ercü's trust! in me for successfully finishing the PhD.

I cannot thank my parents Nedret Toker and Mithat Toker enough for their presence and their endless love. With their respect in my decisions, unlimited support and encouragement, I always felt safe and strong enough to achieve what I aimed for. They taught me the value of science and importance of principles, both as my parents and my teachers and among everyone they are the ones to understand me the best for what I am trying to achieve.

Finally, I would like to thank my brother Umut Toker, whose presence has always been the biggest source of happiness to me. He is my best friend, my mentor in all areas of life, the source of ideas I have always followed and my greatest inspiration in life. His support and his trust in me have always given me strength and through our "unserious" perspective of life, we were able to make fun of anything, which made life much easier. As in all aspects of my life, his love, guidance and support made my PhD procedure much easier.

I dedicate this dissertation to my dear family, for their continuous and endless love, support and presence…

## LIST OF TABLES

## LIST OF FIGURES

# 1 CHAPTER 1: INTRODUCTION

## 1.1 Motivation and Background

A biomaterial is defined as a natural or synthetic material, designed to partially or completely replace a biological tissue or organ, and to function in contact with living tissues [1,2]. The major requirement to be satisfied for a biomaterial is biocompatibility, which involves both biological and mechanical compatibility of the biomaterial with the living tissue [1,3-5]. A biologically compatible biomaterial should not cause any adverse reactions in the surrounding tissue and body, such as toxic, allergic, carcinogenic reactions, which mainly requires inertness of the material [1,4-6]. Moreover, depending on the application, the biomaterial should provide proper contact with the tissue such that, it should allow adhesion or ingrowth of the host tissue if the application requires fixation of the material in the specific body location or should not prevent the flow of the body fluids with unnecessary adhesion [6]. On the other hand, mechanical compatibility involves appropriate mechanical properties, such as adequate strength for the specific application, matching Young's modulus with the surrounding tissue, sufficient ductility, fatigue and wear resistance [4-8].

In order to determine whether a potential biomaterial fulfills the necessary requirements for a certain biomedical application, biocompatibility testing is essential. Biocompatibility testing basically involves investigation of the biological and mechanical compatibility of the biomaterial with the contacting tissue, by the application of *ex situ*, *in vitro* and mechanical tests to the selected material, regarding the target biomedical application. The parameters that should be analyzed during the biocompatibility testing of a material vary depending on the material type. Currently, a variety of materials are being used for medical purposes, including metallic, ceramic, polymeric and composite materials, as well as naturally derived materials [5,7]. Each of these material types provides advantages

regarding a certain application and thus, the evaluation of each material should be based on the biocompatibility of the particular material and the requirements of the targeted application. Moreover, depending on biomaterial type of choice, contacting host tissue type and the specific application, advanced and more comprehensive biocompatibility parameters come into picture, in addition to the basic biocompatibility requirements defined above, which require further biocompatibility analysis [6]. Therefore, materials selection is deterministic in terms of the biocompatibility investigation methods.

The biomaterial type of interest in the current study is metallic materials. Metals receive considerable attention in various applications, mainly due to the superior mechanical properties they offer, such as high strength and good fatigue resistance. Metallic biomaterials, specifically biomedical alloys, are used for various biomedical purposes, which include dental and orthopedic implants, cardiovascular devices and surgical tools [4,5,8]. For implants, the main reason for the preference of metallic materials is their load bearing capacity [4,9]. Similarly, for cardiovascular devices and surgical tools, the flexibility and fatigue resistance of biomedical alloys constitute an advantage [10]. Yet, although metallic materials fulfill the necessary mechanical requirements for biomedical applications, their biological compatibility can be insufficient, as metals are highly prone to corrosion [9,11].

Corrosion is the degradation of the metal to oxides, hydroxides, or other compounds as a result of its interaction with liquid or air [1,3]. As the human body contains various fluids with corrosive chemical compositions, it constitutes a very aggressive environment for metallic materials [12,13]. Corrosion of metallic materials within the human body results in metallic ion release into the body, material loss and changes in the chemical structure of the metal, which sacrifice the biocompatibility of the material and cause toxic and adverse reactions in the body [1,3,11,13]. Thus, corrosion resistance constitutes a crucial biocompatibility requirement for metallic biomaterials, in addition to the aforementioned

parameters and should be deeply examined for a complete biocompatibility analysis of metallic biomaterials.

The major factors which determine the corrosion resistance based biocompatibility of a metal in a fluid are the ion release from the metal, and the corresponding tissue response [9, 11-13]. Metallic ion release into the body fluid can be toxic, cause mild or severe adverse reactions in the body and eventually lead to the failure of the biomaterial system [9, 11-13]. Furthermore, during the metal's exposure to the body fluid, depending on the chemical content of the fluid, new structures form on the metal surface, such as oxide layers, which also affect ion release behavior [9, 11-13]. These newly formed structures affect both the host tissue adhesion to the material, and ion release from the metal, by either acting as a protective layer against ion release, or forming defects through which ion release occurs [9, 11-13]. Therefore, it is critical to analyze all the events taking place during a biomaterial's interaction with the surrounding tissue, and especially with body fluids, for understanding the underlying reason of the particular corrosion response of a metal in a body fluid.

The corrosion response of a metallic material is influenced by various factors, including material properties, such as chemical composition, microstructure, geometry, and surface properties of the metal, as well as environmental factors, including pH, temperature, and chemical composition of the surrounding media [12-14]. The material properties, which affect corrosion behavior of a metal are determined by the type of metal, and processing methods applied to give a certain form to the metal [12-17]. Accordingly, the ion release rate and new structure formation behavior is different for various types of metals, depending on the chemical composition, geometry, surface properties and microstructure of the metal [12-17].

Among these factors, surface structure constitutes an important parameter, as the surface of a metal is the first place where fluid-metal interaction starts. Surface structure is

mainly dictated by the processing method applied to obtain a certain shape of the metal. Specifically, the metal surface attains a certain roughness through processing, which is mainly dictated by the shape and frequency of processing marks imposed by the deformation of the metal. This surface roughness affects the microstructure, and thereby, the mechanical properties [15-17]. Metallic materials have complex microstructures, consisting of grains, grain boundaries, dislocations and twins. These microstructural features enable the deformation of metals and evolve in terms of shape and number during deformation [18-20]. Specifically, for metallic materials, plastic deformation occurs by slip process which involves the motion of dislocations in the microstructure [18-20]. During plastic deformation, dislocations interact with grain boundaries, twins and other microstructural features [18-20]. As a result of these interactions, number of grains, grain boundary mismatch angles, density of dislocations and twins in the microstructure are altered, which results in changes in the overall microstructure [18-21]. Moreover, with deformation, the grains attain a certain alignment, which yields anisotropy in the metal [21]. The aforementioned microstructural interactions also determine the hardening and overall mechanical response of the metal thus, microstructure is critical in terms of determining the mechanical compatibility of the metal with the surrounding tissue as well [18-22].

Overall, the microstructure evolution affects the surface properties due to roughness and by yielding a non-uniform distribution of surface energy on the metal, which eventually dictates the corrosion behavior of the material [15-17,22]. Consequently, in terms of defining the biocompatibility of a metallic material, microstructure plays a key role and for a complete understanding of the parameters affecting biocompatibility, the correlation between the biocompatibility, microstructure and mechanical properties of a metallic biomaterial should definitely be constructed.

Biocompatibility of metallic materials has been subject to various studies, where several types of metallic materials were investigated from both material and tissue perspectives, specifically, from material properties, material response, host tissue type and host tissue response aspects [10-15, 23-28]. These include studies on the corrosion performance of implant materials in various body fluids, cell response to metallic biomaterials with various surface properties, mechanical performance of implant materials in contact with body fluids and their mechanical compatibility with the host tissue [10-15, 23-28]. While each of these studies shed light into a different aspect of the biocompatibility issue of biomaterials, they overall put forward the importance of understanding the effect of material related parameters on biocompatibility and the significance of properly simulating clinical conditions for a successful biocompatibility testing.

From this point of view, the current study aims to investigate the biocompatibility of biomedical alloys based on their microstructures and mechanical properties, and establish a correlation between these three parameters. For this purpose, three different metallic materials, including biomedical alloys and conventional metals, were investigated in terms of their microstructures, surface properties and mechanical behaviors under various environments, which simulate clinical conditions in terms of chemical content and potential mechanical loads. For the biomedical alloys, the obtained findings were utilized to make a correlation with the biocompatibility of the material of interest, while for the conventional metallic materials, the outcomes were used to examine the complex microstructural interactions taking place in metallic materials.

## 1.2 Objectives

The current study aims to investigate the biocompatibility of metallic biomaterials by constructing a relationship between microstructure, mechanical property and biocompatibility

in conventional and potential biomedical alloys. For this purpose, three different metallic materials were investigated in terms of their surface properties, microstructure and mechanical behavior, which were then correlated to biocompatibility.

Initially, biocompatibility of a conventional biomedical alloy, namely the Nickel-Titanium (NiTi) shape memory alloy (SMA) was investigated. Although NiTi SMAs have been widely employed in biomedical applications for several decades owing to their shape memory properties, potential Ni release into body fluids is a limiting factor in terms of their biocompatibility, and thus, warrants further investigation. With this motivation, the biocompatibility of NiTi SMAs was investigated via *ex situ* experiments in the first part of this study. Specifically, NiTi SMAs with three different geometries were statically immersed in three fluids simulating different body parts and the alloys and fluids were separately investigated in terms of ion release and new structure formation following the immersion experiments (Chapter 2). The objective of this analysis was to understand the effect of geometry and the surface properties, which are dictated by the processing methods applied to obtain different geometries, on the alloy behavior in each fluid. Moreover, it was also aimed to determine the safest alloy geometry to be utilized in certain body parts and obtain applicable knowledge for the design of new implants specific to different body locations [29].

Following this analysis, NiTi SMAs used in a different application, namely the orthodontic arch wires, were investigated in order to evaluate the biocompatibility testing method used to examine their biocompatibility (Chapter 3). Specifically, commercial orthodontic arch wires which were immersed in artificial saliva, were compared with companion wires that were exposed to actual intraoral conditions. The focus was on the effects of mechanical contact of wires with brackets on the wire surface during exposure to actual intraoral environment and how the observed behavior differs from that in static immersion tests. This part of the current study aimed to compare the *ex situ* environment with

actual clinical conditions for determining the deficiencies in *ex situ* biocompatibility testing methods and contribute to the design of a more realistic biocompatibility testing environment for NiTi orthodontic arhcwires [30].

In the following part of the current work, actual loading conditions were incorporated into the *ex situ* testing environment of NiTi orthodontic archwires. Specifically, undeformed archwires and wires bound to brackets on a dental mold were statically immersed in artificial saliva and their surfaces were comparatively investigated following immersion experiments (Chapter 4). The purpose of this part of the study was to provide a more realistic simulation of the actual clinical conditions and investigate the effects of mechanical contact and stress assisted corrosion on the wire surfaces during immersion. The outcomes of this part showed the importance of incorporation of mechanical contact into the biocompatibility testing environment and analyzing the relationship of biocompatibility with mechanical properties [31].

Next, in order to further investigate the mechanical property-biocompatibility relationship of metallic biomaterials, and to clarify the role of microstructure and particularly anisotropy on the mechanical performance of biomedical alloys, a potential biomedical alloy, namely the Niobium-Zirconium (NbZr) alloy, was investigated. Specifically, the impact responses of both coarse- and ultrafine-grained NbZr alloys with different degrees of anisotropy were examined under various temperatures (Chapter 5). Since impact constituents an important type of loading that implant materials can be subjected to during jumping or falling, it is critical to analyze the impact response of potential implant materials. This analysis aimed to clarify the effect of microstructure, specifically anisotropy, on the impact response of a potential biomedical alloy, and to obtain applicable knowledge for the design of new implants by incorporating the effect of microstructure and anisotropy [32].

For further analyzing the role of microstructure on impact response, the impact behavior of a conventional metallic material, a high-manganese austenitic steel, was investigated under various temperatures (Chapter 6). The reason for the preference of high manganese austenitic steels for this analysis is the complex microstructure of this type of metallic materials, which involves slip-twin interactions. The main objective of this analysis was to understand the microstructural mechanisms, namely slip-twin interactions on the impact response of high manganese austenitic steels. Moreover, with the outcomes of this part of the current study, it is aimed to shed light onto the microstructure-mechanical property relationship in metallic biomaterials and provide comprehensive information on these mechanisms to be utilized in the design of metallic implant materials [33].

Overall, the aforementioned investigations on different metallic materials demonstrated that microstructure is a major parameter in determining the surface properties and mechanical response of metals under various conditions, which consequently dictate the biocompatibility of the metal. Thus, biocompatibility investigation of metallic materials requires consideration of specific chemical and mechanical conditions targeting a particular biomedical application and a particular material. From this point of view, the current study was undertaken with the motivation of providing a deeper understanding of the biocompatibility of metallic materials by constructing a relationship with the microstructure and mechanical properties. For this purpose, potential and well-known biomedical alloys, as well as conventional metallic alloys, were investigated, with a focus on a different aspect of the biocompatibility-microstructure-mechanical property relationship in each chapter of the current study.

## 1.3 References


[1] J. Park, R.S. Lakes, Biomaterials, 3rd ed., Springer, 2007.

[2] S. Bhat, A. Kumar, Biomatter 3 (2013) 1-12.

[3] J. Black, G. Hastings, Handbook of Biomaterial Properties, 1st ed., Chapman and Hall, 1998.

[4] M.B. Nasab, M.R. Hassan, Trends Biomater. Artif. Organs, 24 (2919) 69-82.

[5] J.R. Davis, Handbook of Materials for Medical Devices, 1st ed., ASM International, 2003.

[6] D.F. Williams, Biomaterials 29 (2008) 2941–2953.

[7] A.V. Sabane, JIDAS, 2 (2011) 18-21.

[8] S. Bauer, P. Schmuki, K. Mark, J. Park, Prog. Mater. Sci. 58 (2013) 261‑326.

[9] T. Hanawa, Mater. Sci. Eng. A 267 (1999) 260–266.

[10] G. Mani, M.D. Feldman D. Patel, C.M. Agrawal, Biomaterials 28 (2007) 1689–1710.

[11] T. Hanawa, Mater. Sci. Eng. C 24 (2004) 745–752.

[12] S. Virtanen, I. Milosev, E. Gomez-Barrena, R. Trebse, J. Salo, Y.T. Konttinen, Acta Biomater. 4 (2008) 468‑476.

[13] I. Gurappa, Mater. Characterization 49 (2002) 73–79.

[14] Y. Okazaki, E. Gotoh, Biomaterials 26 (2005) 11–21.

[15] M. Papakyriacou, H. Mayer, C. Pypen, H. Plenk Jr., S. Stanzl-Tschegg, Int. J. Fatigue 22 (2000) 873–886.

[16] R. Huang, Y. Han, Mater. Sci. Eng. C 33 (2013) 2353–2359.

[17] P. Minárik, R. Král, M. Janecek, Appl. Surf. Sci, 281 (2013) 44-48.

[18] Y. T. Zhu, T.G. Langdon, Mater. Sci. Eng. A 409 (2005) 234–242.

[19] Dirk Helm, Alexander Butz, Dierk Raabe, and Peter Gumbsch, JOM 63 (2011) 26-33.

[20] M.A. Meyers, O. Vohringer, V.A. Lubarda, Acta Mater. 49 (2001) 4025–4039.

[21] D. Canadinc, H. Sehitoglu, H.J. Maier, D. Niklasch, Y.I. Chumlyakov, Int. J. Solids Struct. 44 (2007) 34-50.

[22] J. Hou, Q.J. Peng, T. Shoji, J.Q. Wang, E-H. Han, W. Ke, Corrosion Sci. 53 (2011) 2956–2962.

[23] J. Geringer, B. Forest, P. Combrade, Wear 259 (2005) 943–951.

[24] S.H. Teoh, Int. J. Fatigue 22 (2000) 825–837.

[25] J. Geringer, B. Forest, P. Combrade, Wear 261 (2006) 971–979.

[26] Y. Estrin, C. Kasper, S. Diederichs, R. Lapovok, J. Biomedical Mater. Res. A 90 (2008) 1239-1242.

[27] R.D.K. Misra, W.W. Thein-Han, T.C. Pesacreta, M.C. Somani, L.P. Karjalainen, Acta Biomater. 6 (2010) 3339‑3348.

[28] P.K.C Venkatsurya, W.W. Thein-Han, R.D.K. Misra, M.C. Somani, L.P. Karjalainen, Mater. Sci. Eng. C 30 (2010) 1050–1059.

[29] S.M. Toker, D. Canadinc, H.J. Maier, O. Birer, Mater. Sci. Eng. C, 36 (2014) 118–129.

[30] S.M. Toker, D. Canadinc, Mater. Sci. Eng. C, 40 (2014) 142–147.

[31] S.M. Toker, B. Gumus, D. Sahbazoglu, B. Uzer, D. Saher, D. Canadinc, Mater. Sci. Eng. C Submitted (2014).

[32] S.M. Toker, F. Rubitschek, T. Niendorf, D. Canadinc, H.J. Maier, Scripta Mater. 66 (2012) 435-438.

[33] S.M. Toker, D. Canadinc, A. Taube, G. Gerstein, H.J. Maier, Mater. Sci. Eng. A 593 (2014) 120–126.

# 2 CHAPTER 2: EVALUATION OF PASSIVE OXIDE LAYER FORMATION – BIOCOMPATIBILITY RELATIONSHIP IN NiTi SHAPE MEMORY ALLOYS: GEOMETRY AND BODY LOCATION DEPENDENCY [1]

## 2.1 Introduction

Nickel-Titanium (NiTi) shape memory alloys (SMAs) have been widely used for medical purposes within the last few decades, mainly owing to their ability to recover their original shape upon release of applied stress or temperature change without any plastic deformation, and their acceptable biocompatibility in comparison to other metallic biomaterials [2-4]. Biomedical applications making use of NiTi shape memory alloys include orthopedic and dental implants, cardiovascular devices and surgical tools [2-14]. For instance, the Simon filter, a cardiovascular application as well-known as the self-expanding stent, enables filtering of large blood clots, and can be easily placed into the inferior vena cava through a catheter with a minimally invasive procedure by making use of the shape memory effect [5-7]. In the orthopedic field, the examples can be diversified from bone staples to vertebrae spacers, a broad range of medical devices that play an important role in the healing process, facilitated by superelasticity or the shape memory effect [8-11]. These properties are widely used also in dental applications, as in the case of superelastic orthodontic wires that ensure a constant magnitude of applied stress on the teeth throughout the treatment [12-14].

The aforementioned examples and many other medical applications benefiting from the superior shape memory properties of the NiTi alloys in the medical field provide important advantages and new treatment options in various medical cases. However, metallic ion release, and particularly Ni release, is still an issue that requires a deeper understanding for improved safety and biocompatibility of this class of alloys in the human body, especially for long-term treatments. Ni release occurs as a result of the interaction of the alloy with tissue or

body fluids, and is dependent on the type of the alloy, type of the tissue or body fluid surrounding it, as well as the type and morphology of the possible oxide layer(s) forming on the alloy. Each of these parameters has an effect on the way that chemical, mechanical and surface properties of the alloy change within the body, which, in turn, affect the biocompatibility of the material.

Among these parameters, passive oxide layer formation is relatively more critical in terms of affecting the Ni release. As compared to Ni, Ti is chemically a more reactive metal and is able to easily segregate at the surface and form an oxide layer when exposed to atmospheric or aqueous conditions [15, 16]. Ti can form various oxides including TiO, $Ti_2O_3$, and $TiO_2$ [15, 16]. Among these, $TiO_2$ is the thermodynamically the most stable, and thus, the most commonly encountered oxide. Therefore, under aqueous conditions, such as immersion in body fluids, titanium oxides, especially $TiO_2$, are expected to form on NiTi alloys and constitute a passive oxide layer. This passive oxide layer provides a barrier against Ni release [17-22]. Specifically, during the stay of the implant inside the body, the passive oxide layer around it goes through a continuous dissolution and re-formation cycle [23, 24]. This leads to different rates or amounts of Ni release at the dissolution or re-formation phases since the thickness of the oxide layer varies during each phase of the cycle [15-19, 23, 24]. For instance, if the dissolution rate of the oxide layer is larger than its re-formation rate, metal ion release might gradually increase due to the presence of a thinner, and thus, less protective oxide layer [23]. However, as opposed to the general idea that a thicker oxide layer would provide a better prevention against ion release, the possibility of crack formation on the layer increases concomitant with the layer thickness, which might eventually lead to more pronounced ion release [17-19], making the thickness of the oxide layer is a critical parameter for controlling the ion release from the metal. The oxide layer thickness is also affected by the chemical properties of the tissue or body fluid contacting the material, and the time of stay in

the particular body environment. Similarly, other parameters specific to the implant, such as the geometry, the chemical composition of the material(s) used in the design, and the surface roughness imposed upon by processing of the selected materials, also influence the oxide layer thickness. Thus, the design of a biocompatible implant necessitates both the consideration and thorough experimental examination of all of these biological and material-dependent parameters. In many applications utilizing NiTi alloys, the material features a very thin protective oxide layer formed during initial processing, which provides protection against corrosion or random oxidation [17, 18]. However, the presence of a protective oxide layer does not eliminate the necessity of a biocompatibility investigation, as these layers themselves can also be prone to ion release due to potential defects or cracks they may contain.

Biocompatibility of NiTi has been the subject to various studies, where corrosion resistance dictated by Ni release and oxide layer formation has usually been the major criterion defining the biocompatibility [17-22]. Ni release and oxide formation behaviors of the NiTi alloys have been investigated utilizing various methods [14, 19-22, 25-27]. These methods include both static immersion and electrochemical experiments, which were conducted in several simulated body fluids, such as phosphate buffered saline (PBS), physiological solution, artificial saliva and gastric fluid [14, 19-22, 25-27]. Each of these investigations focused on a different aspect of the overall problem, such as the amount of Ni release depending on the alloy compositions, chemical composition of the simulated body fluid of interest, and the type or thickness of the oxide layer present on the alloy surface [14, 17-22, 25-27]. The corresponding results provide information about how Ni release is affected by the aforementioned parameters and conditions; however, it is difficult to draw a solid conclusion regarding the biocompatibility of NiTi, especially in the long term, mainly owing to the fact that the previous works remained focused on very specific cases. To the best of the

authors' knowledge, a systematic investigation of the biocompatibility of NiTi SMAs in various body parts and fluids, and for different geometries has not been forwarded yet.

The current work was undertaken with the motivation of addressing this issue, and thus, the biocompatibility of the NiTi SMA was examined as a function of sample geometry in various fluids that simulate different body parts or fluids. For this purpose, NiTi samples with three different geometries were immersed in three different fluids simulating different body parts. Following the immersion experiments that were carried out for four different time periods, the surfaces of all the samples were investigated via X-ray photoelectron spectroscopy (XPS), scanning electron microscopy (SEM) and energy dispersive X-ray spectroscopy (EDX), in order to evaluate the chemical composition and microstructure of the oxide layers and to identify the phases on these layers. The immersion fluids were examined via inductively coupled plasma optical emission spectrometry (ICP-OES) for the evaluation of possible ion release from the alloys into the fluids. The results indicate that the morphology and chemical composition of the oxide layer and the trend of change in the oxide layer thickness varied for each specimen geometry – immersion fluid combination. The dissolution – re-formation cycle was prevalent for some of the combinations, while the trend was a continuous decrease in the oxide layer thickness in other cases. The variations in this trend for different specimen types in the same liquid showed that specimen geometry has significant effects on the long-term stability of the material surface in the fluid. Overall, the current set of data provides valuable information about how the oxide layer – an important parameter in dictating the ion release, and thus, the biocompatibility of NiTi are affected by various simulated body fluids and alloy properties. Furthermore, the outcomes of the current study also constitute a new set of guidelines to follow while designing implants making use of NiTi SMAs to be employed in treatments targeting a specific body part.

## 2.2 Experimental Procedures

The biocompatibilities of three different groups of NiTi alloy samples were investigated for four different time periods in fluids that simulate three different body parts. The NiTi specimen groups featured three different geometries: two cylindrical specimens with different radii and a plate specimen were used (Figure 2.1), whose dimensions and chemical compositions are summarized in Table 2.1.

**Table 2.1.** Chemical compositions and dimensions of the three different NiTi specimen groups. Chemical compositions are provided in atomic percentage of Ni, where the balance is Ti [1].

| | **Specimen Type** | | **Dimensions** | **Ni content** |
|---|---|---|---|---|
| **Specimen Properties** | Cylindrical | r = 1.75 mm | h = 1.5 cm | 50.7 |
| | | r = 1 mm | h = 2.75 cm | 50.4 |
| | Plate | | 1.3 cm × 0.65 cm | 50.7 |

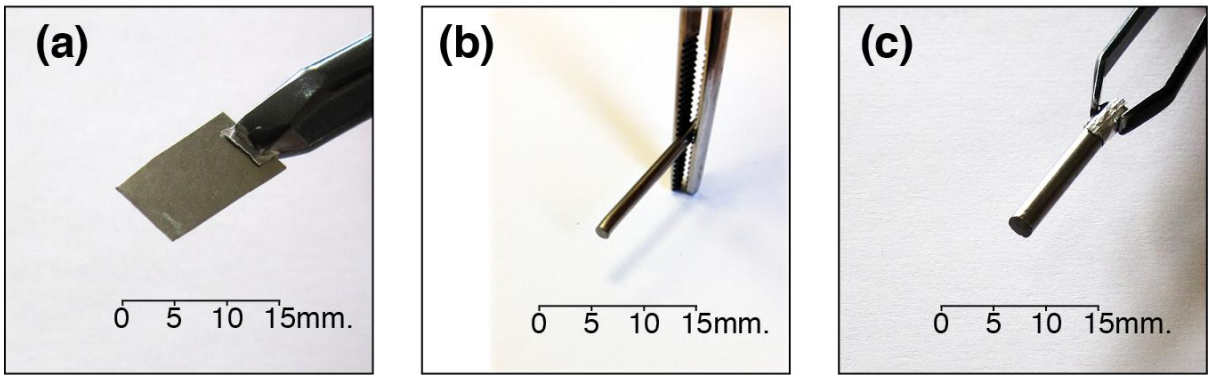


**Figure 2.1.** As-is specimens: **(a)** plate, **(b)** thin wire, and **(c)** thick wire [1].

Each specimen was immersed in 5 ml of fluids simulating three different body parts: gastric fluid (GF), artificial saliva (AS), and conventional simulated body fluid (c-SBF) as

artificial blood. The chemical content and pH values of these fluids are provided in Table 2.2. Normally, the pH of the natural saliva is around 7; however, the dental plaque induces a low pH value [28]. Thus, in order to incorporate effects of acidic environment caused by the dental plaque on dental alloys and simulate the aggressive environment that would potentially result from nutritional habits; a lower pH value was preferred for AS in this study. The immersion periods for each sample in each fluid were chosen as 1, 7, 14 and 30 days. All immersion fluids utilized in the experiments were kept in separate sealed tubes. During all immersion experiments, the fluid temperature was kept constant at 37 °C for simulating the body temperature, where the sealed tubes were immersed in an electronically-controlled water bath. Prior to the experiments, it was ensured that all the prepared fluids were stable solutions. Following the experiments, no salt deposition was observed in any of the fluids, indicating that the fluids were kept stable during the immersion procedure.

**Table 2.2.** Chemical contents of the three simulated body fluids used in immersion experiments [1].

| Solution | Ingredients | Amount of Ingredients (g/l) | pH |
|---|---|---|---|
| Gastric Fluid (GF) | NaCl | 9 | 2 |
| Artificial Saliva (AS) | NaCl | 0.4 | 2.3 |
| | KCl | 0.4 | |
| | $CaCl_2 \cdot 2H_2O$ | 0.906 | |
| | $NaH_2PO_4 \cdot 2H_2O$ | 0.690 | |
| | $Na_2S \cdot 9H_2O$ | 0.005 | |
| | Urea | 1 | |
| Artificial Blood (c-SBF) | NaCl | 8.036 | 7.4 |
| | $NaHCO_3$ | 0.352 | |
| | KCl | 0.225 | |
| | $K_2HPO_4 \cdot 3H_2O$ | 0.230 | |
| | $MgCl_2 \cdot 6H_2O$ | 0.311 | |
| | 1M HCl | 40 ml | |
| | $CaCl_2 \cdot 2H_2O$ | 0.293 | |
| | $Na_2SO_4$ | 0.072 | |
| | TRIS | 6.063 | |
| | 1M HCl | 0.2 ml (for pH adj.) | |

The specimens were cleaned with ethanol in an ultrasound bath, and their surfaces were observed with SEM prior to the immersion experiments (Figure 2.2). It should be noted that the NiTi alloys tested in the current study feature a very thin protective layer that was formed during the initial processing. This type of protective oxide layer is very common for implant materials, and thus, it is more realistic to apply the immersion tests without removing the initial oxide layer as the tested alloys constitute potential implant materials. Therefore, the sample surfaces were not chemically cleaned prior to immersion experiments in the current study.

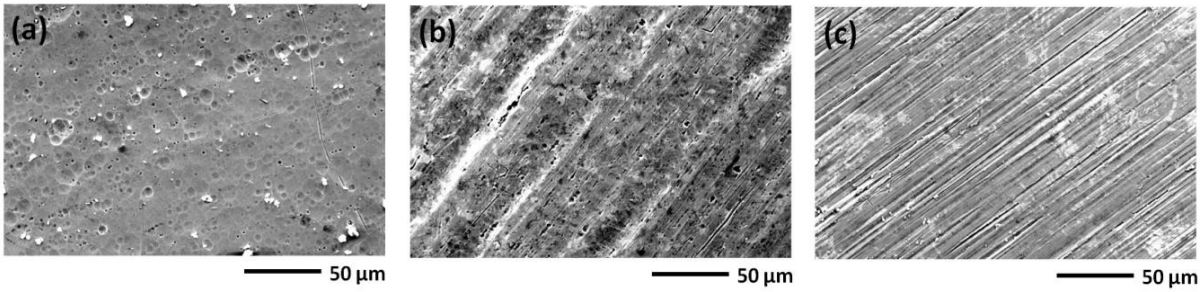


**Figure 2.2.** SEM images of as-is specimens: **(a)** plate, **(b)** thin wire, and **(c)** thick wire [1].

The most evident differences on the as-is specimen surfaces arose from the processing marks. Specifically, the processing marks were in the form of cavities on the plate specimens (Figure 2.2(a)), while both cavities and lines imposed upon by processing were present on the surfaces of the thin wire samples (Figure 2.2(b)). For the thick wires, on the other hand, closely located scratches of large densities were induced by the processing (Figure 2.2(c)). These geometry-related differences between the initial surfaces are important to note since they are also expected to influence the interaction of the samples with the immersion fluids.

Following the immersion procedure, the specimens were systematically examined via XPS, SEM and EDX. The XPS analyses were carried out on a Thermo Scientific K-α X-ray photoelectron spectrometer furnished with a monochromatized Al-$K_\alpha$ source. The base pressure was less than $5x10^{-9}$ Torr and a flood gun was used to avoid charging. The pass

energy was 50 eV, which corresponds to an energy resolution of approximately 0.5 eV. The depth profiling was performed using Ar ions accelerated at 3000 eV with 10 s etch cycles. The relevant peaks were deconvoluted for chemical speciation, and the Al-Scofield atomic sensitivity factors library provided by the manufacturer was utilized for quantification. The Titanium 2p region was fitted to separate the contributions from the $TiO_2$, the non-stocihiometric oxide $TiO_{x<2}$ and the metallic titanium. Post-experimental SEM was carried out on a Zeiss Ultra Plus field emission scanning electron microscope in order to establish a comparison of the tested samples with the as-received ones in order to capture the changes on the specimen surfaces, such as passive oxide layer formation and pitting corrosion, induced by immersion into various body fluids for various time periods. EDX analysis was conducted for the determination of structures with potentially different chemical compositions observed by SEM. Finally, immersion fluids were analyzed with ICP-OES in order to investigate the possible Ni or Ti ion release from the alloys into the fluids. The immersion fluids were diluted with deionized water and 2M $HNO_3$ with a ratio of 1:6. Original immersion fluids were used with the same dilution for calibration of the instrument. The measurements were conducted at wave lengths of 341.476 nm for Ni and 336.121 nm for Ti.

## 2.3 Results and Discussion

### 2.3.1 Passive Oxide Layer Formation and Structural Changes

In order to tabulate the changes in the chemical compositions of the surface elements of the samples upon immersing in the simulated body fluids, thorough XPS analysis was carried out on the tested samples. An example depth profile is presented in Figure 2.3 for the thin wire sample immersed in SBF for 30 days. In order to evaluate the thickness of the oxide layers that formed on the specimen surfaces following a 30-day immersion period, the etch

times where Ni composition begins to saturate, i.e. where the slope of the Ni concentration curve stops increasing and approaches a plateau, were noted as the Ni saturation time in the depth profiles for each 30-day sample. These data provided information about the oxide layer thickness since the Ni signal emerged and increased as the oxide layer on top of the specimen was swept away. The saturation point of the Ni signal corresponds to the etch level where the oxide signal is depleted, such that longer Ni saturation periods refer to thicker oxide layers.

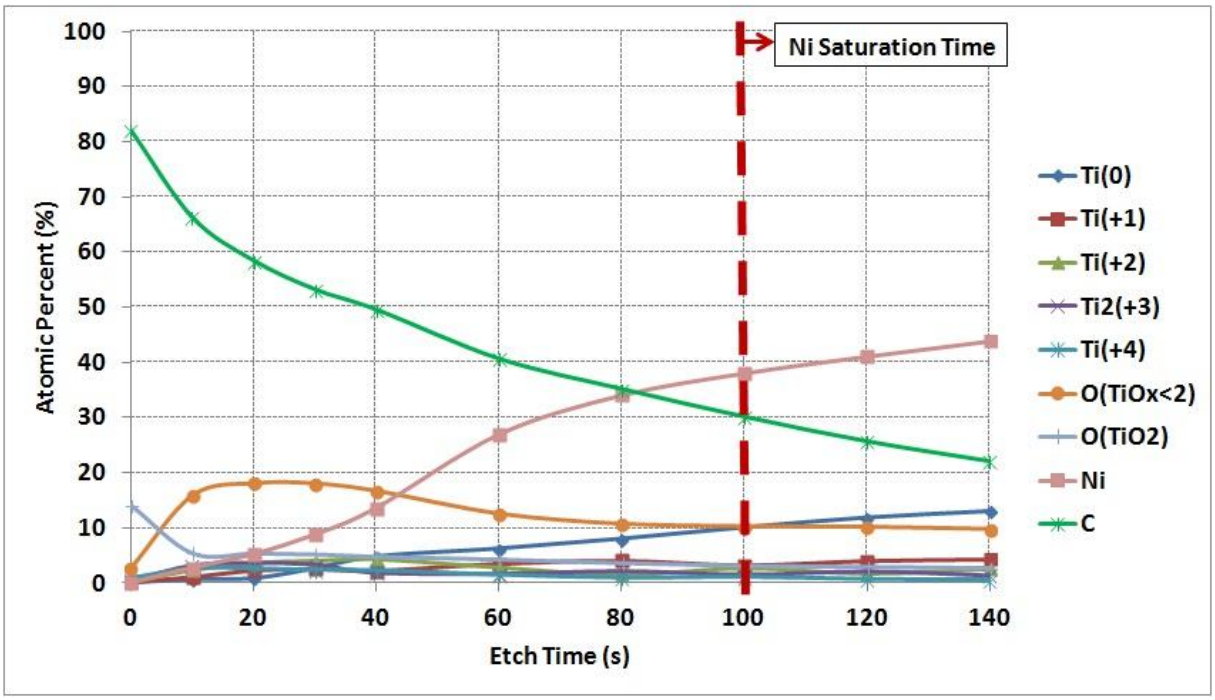


**Figure 2.3.** Example depth profile for the thin wire immersed in SBF for 30 days. The Ti 2p region was deconvoluted to species with oxidation states of 0, +1, +2, +3 and +4. The Ti $2p_{3/2}$ peak was used for quantification. The Ni 2p region consists of metallic nickel signal, which was integrated for quantification. The O 1s region was deconvoluted to separate the contributions of the stoichiometric ($TiO_2$) and non-stoichiometric ($TiO_{x<2}$) oxides. The vertical dashed line represents the beginning of the plateau of the Ni line which indicates the Ni saturation time [1].

The comparison of the Ni saturation times for each 30-day sample and as-is samples is presented in Figure 2.4. The results showed that thicknesses of the oxide layers on the thin and thick wire samples immersed in AS and SBF were very close to each other, while the thicknesses of the oxide layers on the plate samples immersed in AS and SBF were much lower in comparison, however very similar to each other. Considering that the contents of

both AS and SBF give way to the formation of a stable oxide layer, the similarity of oxide layer formation in these fluids is not surprising. This result also points at the dependence of oxide layer formation on geometry and surface properties. As evident from the SEM figures of the as-received samples, thin and thick wire samples contain a large amount of processing marks while the plate specimens exhibit a much smoother surface. Increase in surface roughness results in abundance of higher surface energy regions, which favor the formation of new structures, such as oxide layer and corrosion products on the surfaces [29-35]. As a result, formation of the thicker oxide layers on thin and thick wires, and the much thinner oxide layers on plate samples immersed in AS and SBF for 30 days is a reasonable result.

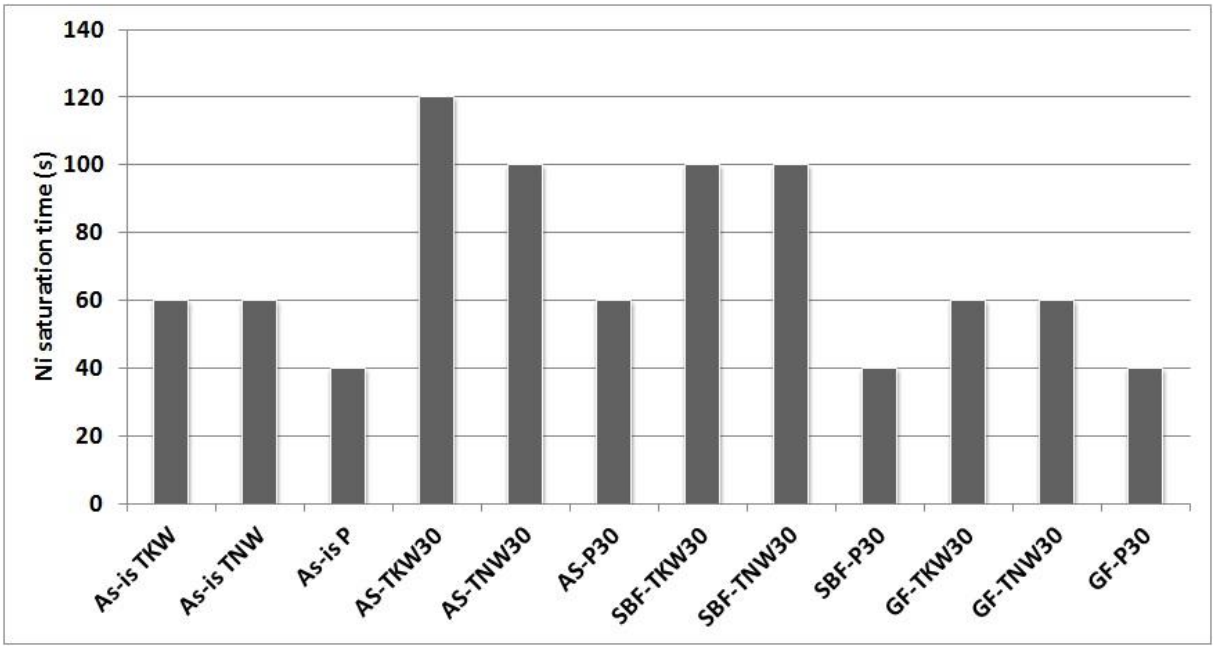


**Figure 2.4.** Ni saturation times for as-is samples and samples immersed in AS, SBF and GF for 30 days. AS: Artificial Saliva; SBF: Simulated Body Fluid; GF: Gastric Fluid; TKW30: Thick wire, day 30; TNW30: Thin wire, day 30; P30: Plate, day 30. Ni saturation time provides an estimation of the oxide layer thickness [1].

As for the samples immersed in GF, Ni saturation times were much lower as compared to thin and thick wires immersed in AS and SBF, as low as those on the as-is samples indicating the presence of a thinner oxide layer on specimens immersed in GF for 30 days. GF is a highly acidic and halogenic fluid, which creates a very aggressive environment and

obstructs the formation of new structures, such as a stable oxide layer. Both AS and SBF have a significant carbon (C) content, and thus, in order to observe any possible C related deposition on the samples immersed in AS and SBF, their C contents at the initial etch level and 140 seconds after etching were also evaluated (Figure 2.5). For the calculation of the atomic percentage of C, only the elements Ni, Ti, C and O were considered to constitute the overall composition. The results indicate a significant amount of C deposition on the thin and thick wires, while this amount was lower for the plate samples. The observed behavior is similar to the case of oxide layer formation on the thin and thick wires and the plate samples, and can also be associated with the surface quality: the increased surface roughness of the thin and thick wires due to the presence of processing marks promoted more C deposition, whereas the smoother surface of plate samples allowed for less C deposition [29-35].

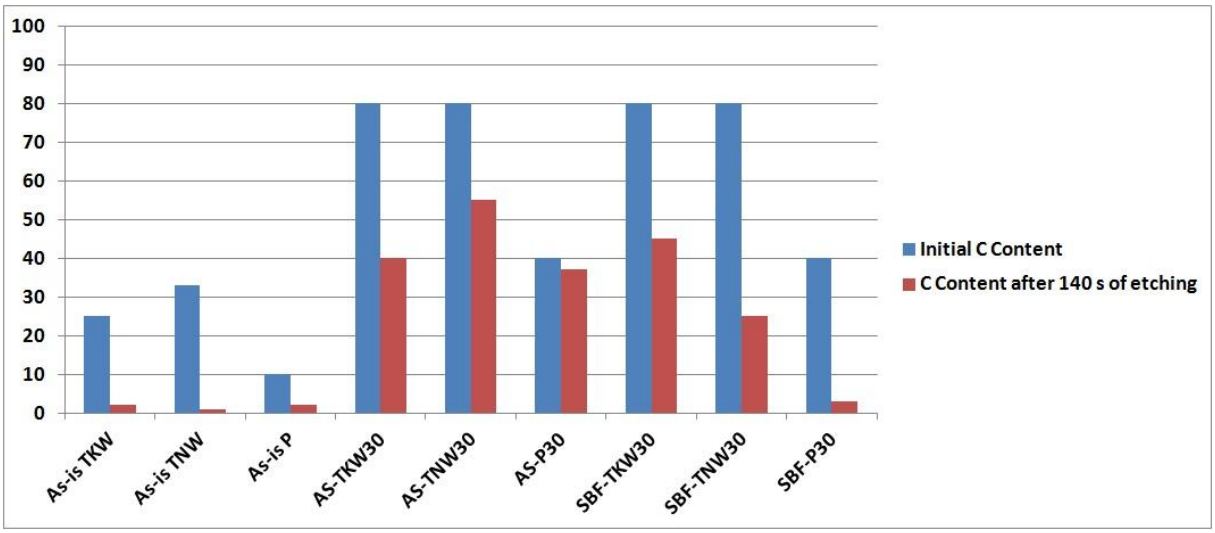


**Figure 2.5.** C contents of as-is samples and samples immersed in AS and SBF for 30 days obtained at the initial level and after 140 seconds of ion etching. Ni, Ti, C and O elements were considered to constitute the overall composition during atomic percentage calculation of C. AS: Artificial Saliva; SBF: Simulated Body Fluid; TKW30: Thick wire, day 30; TNW30: Thin wire, day 30; P30: Plate, day 30 [1].

Observing the depth profiles of all tested samples (example data shown in Figure 2.3), some general conclusions can be drawn. For instance, for all samples, the most significant elemental changes on the specimen surfaces (etch time = 0 s) were observed in the amounts of

Ti and O elements, which represent $TiO_2$ and $TiO_x$. Specifically, where the $TiO_2$ percentage approached zero, the $TiO_x$ percentage increased, indicating that the non-stoichiometric $TiO_x$ layer forms only in the absence of a $TiO_2$ layer. This behavior can be clearly observed in Figure 2.3, where the surface is stoichiomeric $TiO_2$-rich, and the non-stoichiometric $TiO_x$ layer emerges only as the $TiO_2$ layer is swept away upon etching. Normally, $TiO_x$ formation occurs when there is a shortage of oxygen atoms in the system [17]. Thus, under oxygen-rich conditions, similar to those provided by the three simulated body fluids in the current study, the expected result is $TiO_2$ formation. Considering that the valence state of Ti (+4) during the formation of $TiO_2$ is the most stable state of Ti and the expected dominant behavior of $TiO_2$ in the oxygen-rich environment, it can be deduced that formation of $TiO_2$ is favored over $TiO_x$. [36]. As $TiO_2$ is a stoichiometric, and thus, a more stable phase, its favorable formation on the metal surface is beneficial in terms of biocompatibility of the material.

The EDX line profiles obtained from representative regions of the samples are presented in Figures 6-10, which show relative intensities of Ni, Ti, C and O signals. Normally, concentration profiles are used in evaluating EDX data, however; C and O are very hard to quantify by EDX, and thus, in order to compare the relative amounts of the analyzed elements; intensity plots were utilized instead of concentration plots. The representative regions that were examined by the line profile analysis were selected based on the amount of representative structures that needed to be identified. The corresponding SEM images are shown underneath the line profiles, where some images seem blurry due to the very high magnification applied to identify even the smallest structures based on their brightness variations.

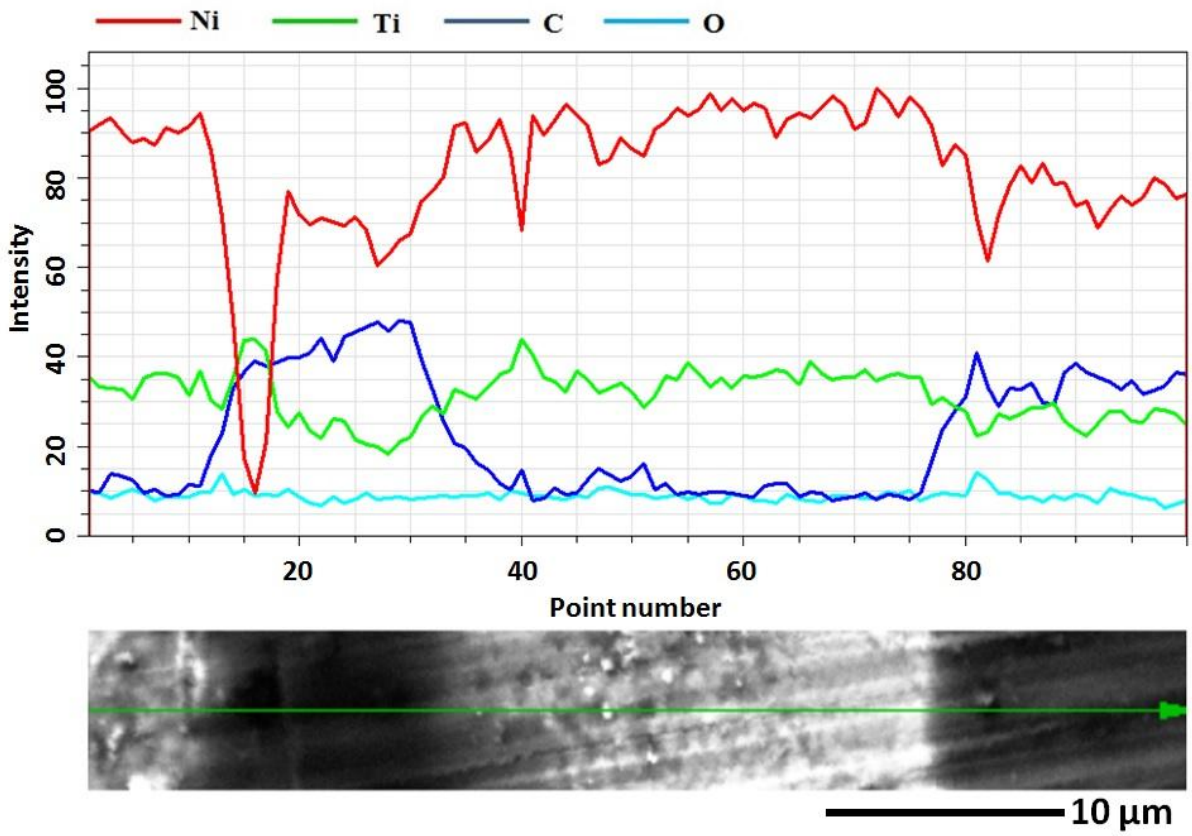


**Figure 2.6.** EDX profile of thick wire immersed in c-SBF for 14 days [1].

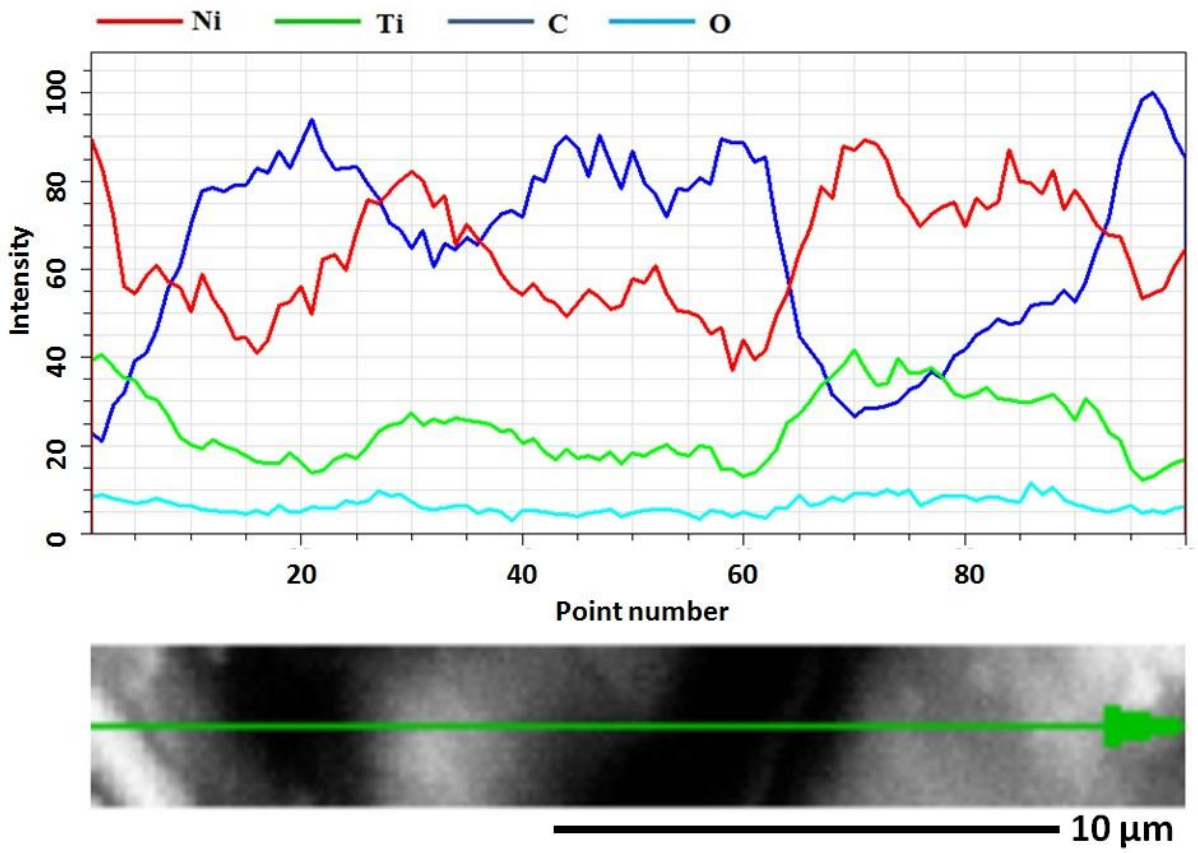


**Figure 2.7.** EDX profile of thick wire immersed in AS for 14 days [1].

The XPS depth profile analysis results demonstrated that the changes of the surface atomic percentages of Ni and Ti in all samples were almost negligible as compared to O signals originating from $TiO_2$ and $TiO_x$ (Figure 2.3). On the contrary, EDX line profiles (Figures 6, 7, 8, 9 and 10) showed that, depending on the fluid, either Ni or Ti revealed signals of larger intensity, while O signals, which are expected to originate from the $TiO_2$ or $TiO_x$ oxide layers, are much weaker as compared to Ni and Ti signals. This inconsistency between the XPS and EDX results is noteworthy and stems from differences in volume probed by these two methods. In particular, XPS provides information about the first 1-10 nm thick layer of the surface [37, 38], while EDX provides data from much thicker layers averaging the top few hundreds of nanometers from the surface [37, 38]. As the thickness of the oxide layer is expected to be about a few nanometers, it is normal that XPS provides

information about the changes in the oxide layer composition. Similarly, as EDX is capable of penetrating into deeper layers, it is expected to yield characteristic peaks from the material itself, which correspond to Ni and Ti signals for the current samples.

The intensity differences of EDX signals of Ni and Ti for the specimens immersed in different fluids indicates that either Ni or Ti interacts more actively with the fluid, depending on the chemical content of the particular fluid. The compounds that formed between Ni and Ti could also be varying during immersion, as a result of the reactions between the fluid, and Ni or Ti. It was previously observed that the oxidation process of NiTi triggers the diffusion of Ni atoms from the surface into the inner layers, where some of these diffusing atoms join the inner $Ni_3Ti$ layer and some exist as free Ni underneath the oxide layer [18]. Similarly, depending on the reactivity of Ni and Ti in the particular fluid, different intermediate phases might be forming from Ni and Ti under the oxide layer, resulting in Ni and Ti signals with diverse intensities.

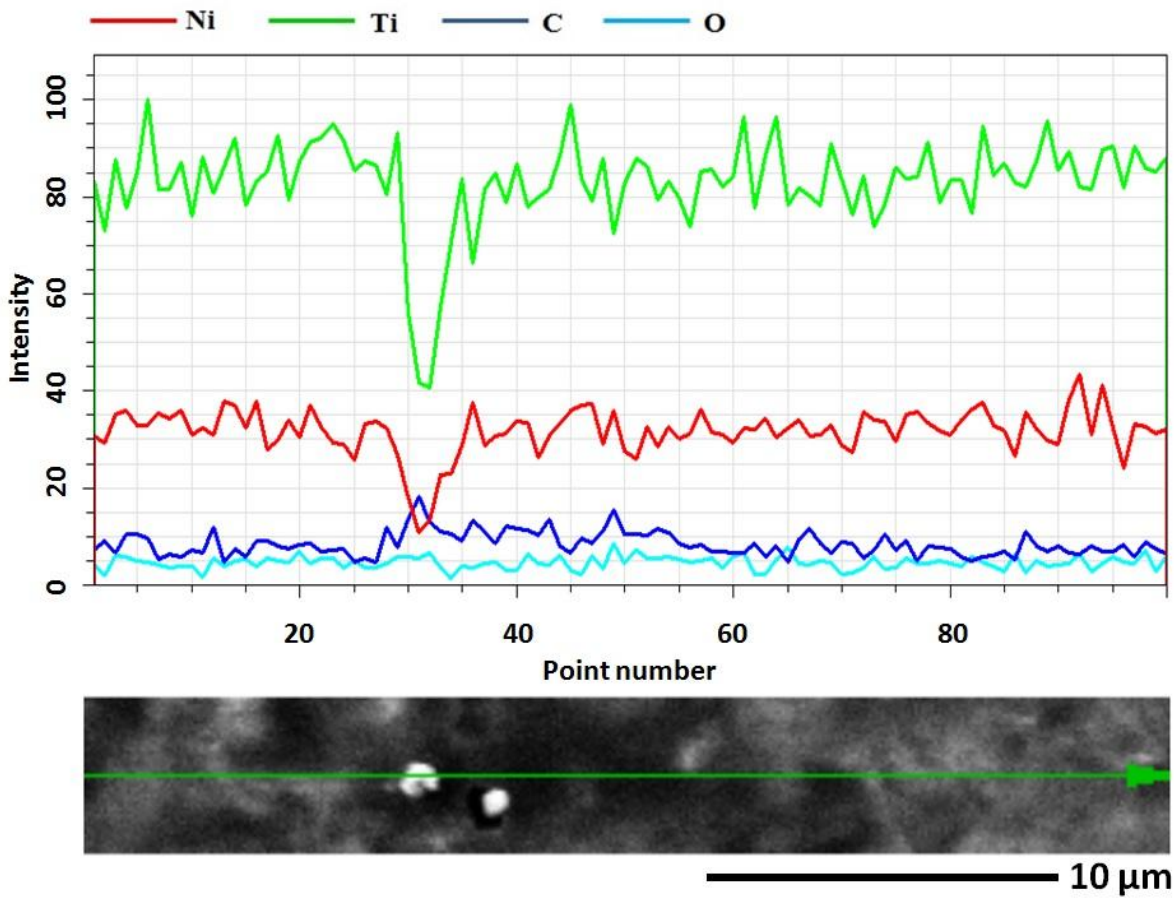


**Figure 2.8.** EDX profile of plate immersed in GF for 14 days [1].

Intensity changes in Ni and Ti signals of the alloys immersed in AS and c-SBF were similar, such that the intensity of Ni signal was much stronger than that of Ti upon immersion in both fluids, with significant amount of fluctuation (e.g. Figures 6 and 7: thick wires immersed in AS and c-SBF for 14 days; Figures 9 and 10: thin wires immersed in AS and c-SBF for 14 days). On the contrary, the alloys immersed in GF demonstrated the exactly opposite behavior of those immersed in AS and c-SBF, such that the Ti signal was more intense and exhibited more fluctuation compared to Ni (Figure 2.8; plate immersed in GF for 14 days). This behavior is a good example of the different interaction tendencies of Ni and Ti in different fluids. As GF is the most aggressive fluid expected to lead to the largest amount of Ni release, the observed intense Ti signal on the plate sample immersed in GF is reasonable since the Ni amount decreases with Ni release to a level below that of Ti. On the other hand,

the more intense Ni signals observed in EDX profiles of thick wires and thin wires immersed in AS and c-SBF for 14 days could originate from either the accumulated Ni under the $TiO_2$ layer or the probable inner $Ni_3Ti$ layer [18].

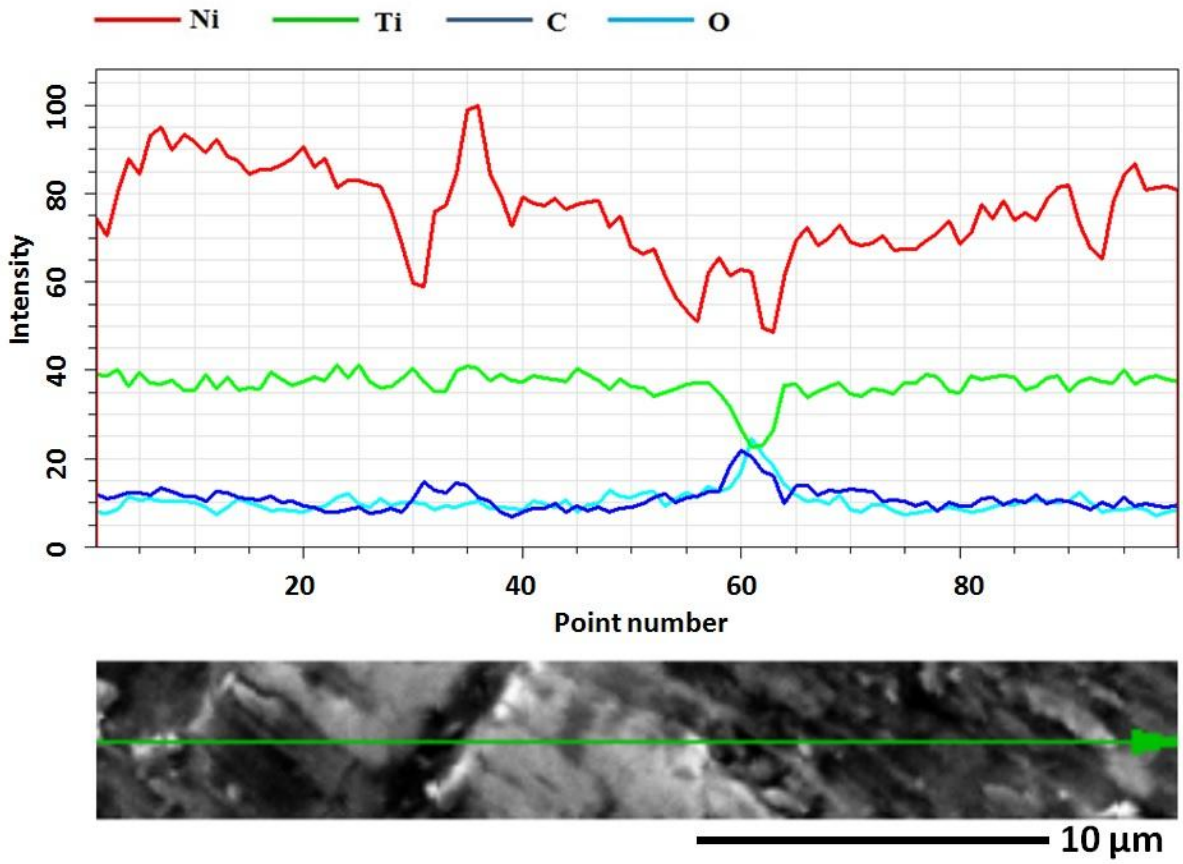


**Figure 2.9.** EDX profile of thin wire immersed in c-SBF for 14 days [1].

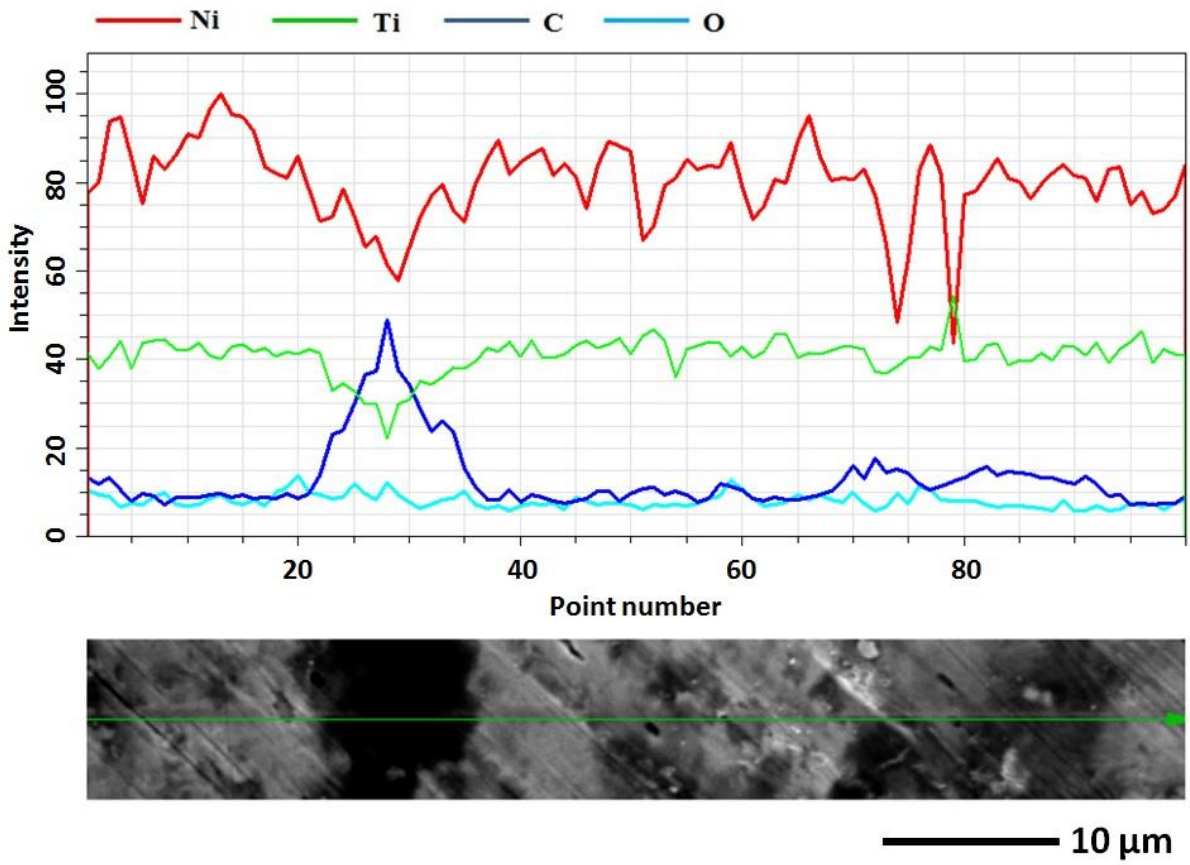


**Figure 2.10.** EDX profile of thin wire immersed in AS for 14 days [1].

The structures that formed on the specimen surfaces during immersion experiments varied depending on the fluid type, specimen geometry and immersion period. For instance, the time-dependent changes on surfaces of the thick wires immersed in c-SBF and AS, plates immersed in GF, and thin wires immersed in c-SBF and AS can be evidenced by the SEM images provided in Figures 11, 12, 13, 14 and 15, respectively. Specifically, formation of a leaf-shaped dark structure was observed on the thick wire samples immersed in c-SFB after day 1 (Figure 2.11(a)). However, the shape and density of this structure was altered with time (Figure 2.11(b)-(d)). Based on the EDX data showing the increase in C content corresponding to the dark areas on the sample surface (Figure 2.6), it can be argued that these dark zones are C containing compounds, which concentrate around the processing marks. Similar leaf-shaped dark structures were also observed on thick wires immersed in AS, however; they exhibited a higher density and remained more stable with time (Figure 2.12(a)-(d)) as

compared to those observed on thick wires immersed in c-SFB. Moreover, the intense C signal increased in the darker areas present in the EDX profile (Figure 2.7), confirming that the dark structures are C containing compounds. The more intense and stable behavior of the dark structures in AS is attributed to the C-rich formulation of AS. These dark structures are concentrated around processing marks on these specimens, as well, which shows that the processing marks provide available sites for the accumulation of new structures.

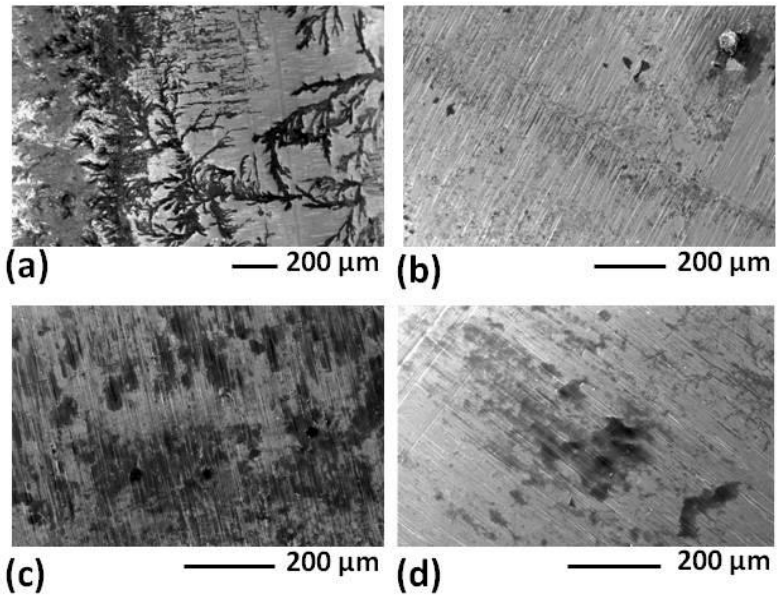


**Figure 2.11.** SEM images of thick wires immersed in SBF for **(a)** 1 day, **(b)** 7 days **(c)** 14 days, and **(d)** 30 days [1].

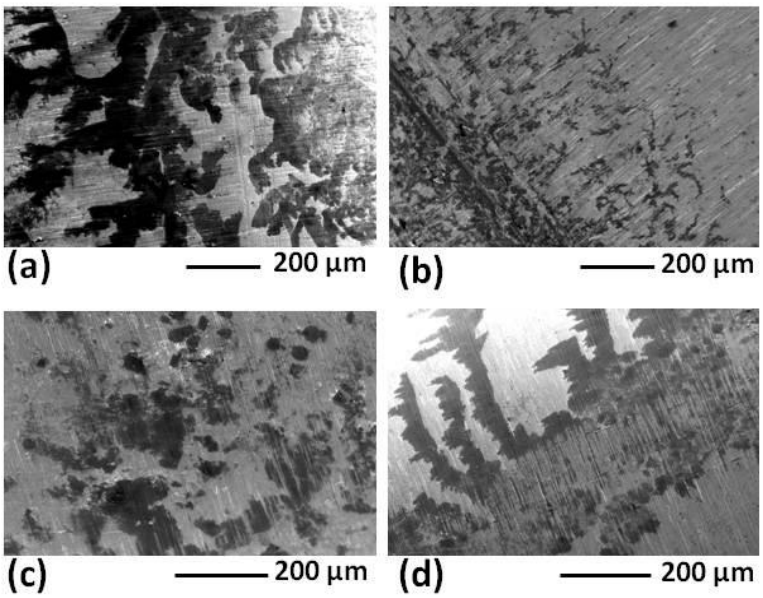


**Figure 2.12.** SEM images of thick wires immersed in AS for **(a)** 1 day, **(b)** 7 days **(c)** 14 days, and **(d)** 30 days [1].

The new phases that formed on the specimen surfaces after immersion are corrosion products, such as oxide layer particles or precipitates, originating from reactions between certain elements from the simulated body fluid with the specimen. Specifically, previous work has shown that structures which act similar to impurities in terms of the integrity of the material, such as grain boundaries, constitute stress concentration sources due to the increased dislocation density around them [29, 30]. As a result they form high-energy regions, which provide available sites for the nucleation of new phases, such as impurities and corrosion products [31-35]. Accumulation of new phases along grain boundaries or processing marks has been reported for various materials in previous studies [31-35]. The processing marks on the materials used in the current study constitute an example to this phenomenon, since they also act as high-energy regions in the material, around which the corrosion products segregate. The differences between the structures that formed on specimens immersed in SBF and AS mainly arise from the differences in the chemical contents of these two fluids, however; a different trend was evident for the GF. The SEM images of the plate specimens

immersed in GF (Figure 2.13) reveal that randomly distributed dark spots formed on the sample surfaces, which seem to have penetrated deeper into the surface, rather than the leaf-shaped dark structures imposed upon by immersion into the c-SFB and AS. These structures are cavities resulting from the acidic attack due to the very low pH of GF, as evidenced by the lack of correspondence between these dark structures and C content in the EDX profile (Figure 2.8). Another factor responsible for the formation of these cavities is the high halogen content of GF (high chloride content), which results in pitting corrosion of local regions on sample surfaces [13]. In addition, as opposed to the thick wires, the localization of the dark spots on the plate surfaces were independent of the processing marks on the specimens, which indicates that the processing marks on thick wires served as more effective sites for new phase accumulation.

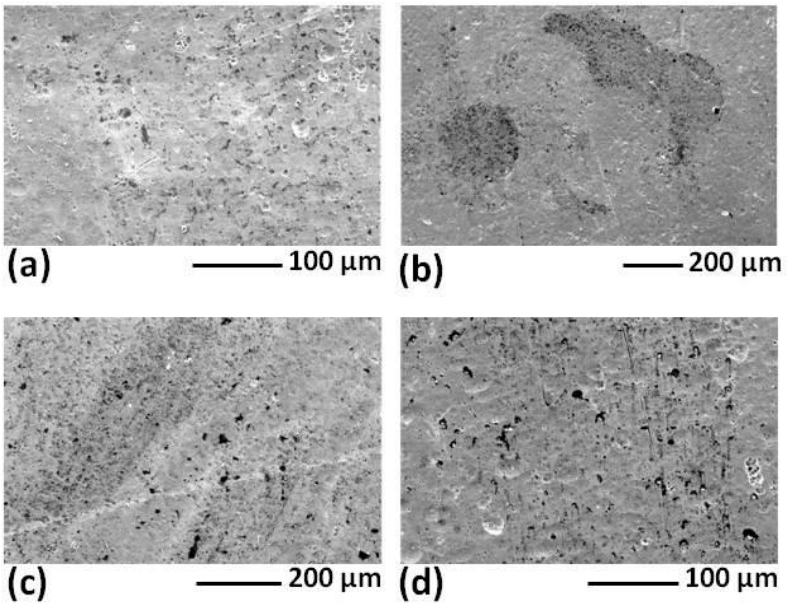


**Figure 2.13.** SEM images of plates immersed in GF for **(a)** 1 day, **(b)** 7 days **(c)** 14 days, and **(d)** 30 days [1].

When the SEM images of thin wires immersed in c-SBF and AS (Figures 14 and 15) are examined, similarities to the thick wires immersed in c-SBF and AS can be identified. For instance, dominance of the dark structures on the thin wire surfaces is evident as in the case of

thick wires. These dark structures assumed an irregular form on the thin wires immersed in c-SBF, while they exhibited a more clear leaf-like shape on the thin wires immersed in AS. The EDX profiles of thin wires immersed in c-SBF and AS indicate that these dark structures are C containing precipitates (Figures 9 and 10). The higher density of the dark structures on thin wires immersed in AS (Figure 2.15) and the more intense C signal around these dark areas on thin wires immersed in AS (Figure 2.10) both stem from the higher C content of the AS as compared to the c-SBF. Since the observed dark structures are C-rich corrosion products, their localization around the processing marks was expected, as also observed in the case of thick wires, since processing marks provide high energy regions for the nucleation of corrosion products. The processing marks were more densely located on the thin wires, which resulted in a denser localization of the corrosion products as compared to those on thick wires.

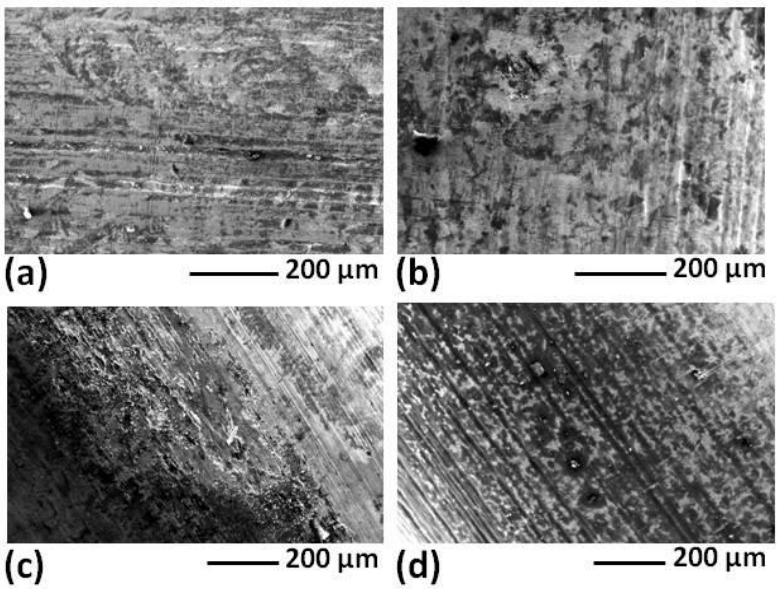


**Figure 2.14.** SEM images of thin wires immersed in SBF for **(a)** 1 day, **(b)** 7 days **(c)** 14 days, and **(d)** 30 days [1].

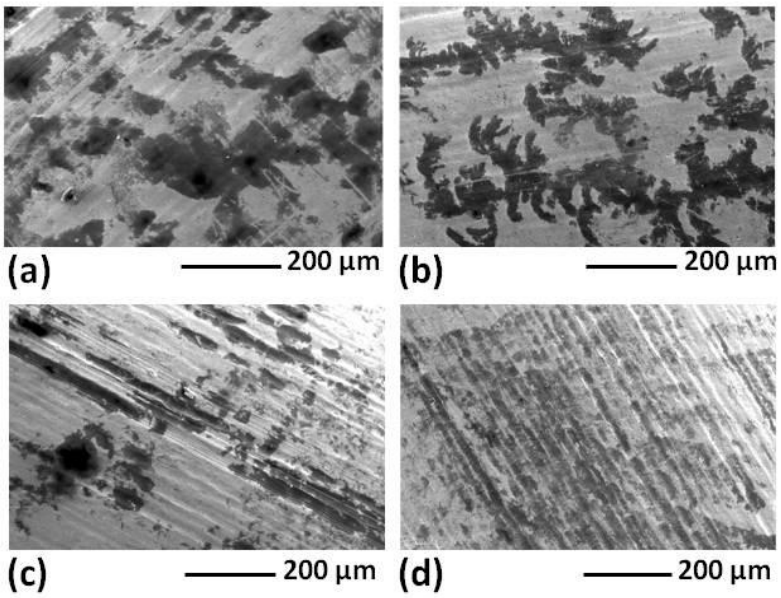


**Figure 2.15.** SEM images of thin wires immersed in AS for **(a)** 1 day, **(b)** 7 days **(c)** 14 days, and **(d)** 30 days [1].

### 2.3.2 Ion Release

Results of the ion release analysis of immersion fluids via ICP-OES are tabulated in Tables 2.3, 2.4 and 2.5 for c-SBF, AS and GF, respectively. These results show that, for all the samples in all immersion fluids, Ti release was less than Ni release for all immersion periods. Comparing the three immersion fluids, the least aggressive fluid for all the alloys was c-SBF, which resulted in Ni release only from the plate alloy upon 30-day immersion (Table 2.3). However, the detected ion release amount was still less than the critical Ni amount that would lead to allergic reactions in the body, which is specified as 600-2500 µg/person [14]: the average blood volume of an adults is about 7 percent of the body weight, or about 5 liters [39], which places the critical Ni amount into the 0.12-0.5 mg/l range. Accordingly, one can deduce that all three alloys considered in the current work would be safe in a blood media in terms of ion release for up to a 30-day interaction period. However, experiments featuring longer immersion times or extrapolation of the current experimental

results to much longer times is necessary in order to ensure the safe utility of these alloys in blood for extended periods of time.

**Table 2.3.** Ni and Ti ion releases in c-SBF. The "-" indicates that measured ion concentration was below the detection limit [1].

| | **„Plate in c-SBF"** | | **„TKW in c-SBF "** | | **„TNW in c-SBF "** | |
|---|---|---|---|---|---|---|
| | *c*(Ni) / $mg \cdot l^{-1}$ | *c*(Ti) / $mg \cdot l^{-1}$ | *c*(Ni) / $mg \cdot l^{-1}$ | *c*(Ti) / $mg \cdot l^{-1}$ | *c*(Ni) / $mg \cdot l^{-1}$ | *c*(Ti) / $mg \cdot l^{-1}$ |
| **Day 1** | - | - | - | - | - | - |
| **Day 7** | - | - | - | - | - | - |
| **Day 14** | - | - | - | - | - | - |
| **Day 30** | 0.096 ± *0.001* | - | - | - | - | - |

**Table 2.4.** Ni and Ti ion releases in AS. The "-" indicates that measured ion concentration was below the detection limit [1].

| | **„Plate in AS"** | | **„TKW in AS"** | | **„TNW in AS"** | |
|---|---|---|---|---|---|---|
| | *c*(Ni) / $mg \cdot l^{-1}$ | *c*(Ti) / $mg \cdot l^{-1}$ | *c*(Ni) / $mg \cdot l^{-1}$ | *c*(Ti) / $mg \cdot l^{-1}$ | *c*(Ni) / $mg \cdot l^{-1}$ | *c*(Ti) / $mg \cdot l^{-1}$ |
| **Day 1** | - | - | - | - | 0.024 ± *0.001* | - |
| **Day 7** | - | - | - | - | 0.030 ± *0.006* | - |
| **Day 14** | - | - | - | - | 0.036 ± *0.004* | - |
| **Day 30** | - | - | 0.060 ± *0.006* | - | 0.054 ± *0.008* | - |

The current results indicate that the most aggressive fluid for all the samples was GF, as evidenced by the increasing Ni and Ti amounts in GF through time (Table 2.5). Considering its highly acidic and halogenic content and the corroded surfaces of the samples immersed in GF apparent from the SEM images of Figure 2.13, the higher ion release in GF compared to

other fluids is an expected result. The ion release in GF up to a 30-day immersion was still lower than the critical Ni ion release, however; it is essential to investigate ion release for longer time periods, especially for aggressive solutions, such as GF, as critical biomedical devices, such as oesophageal and pancreatic stents, are used in a GF environment and are made of self expanding materials, including NiTi alloys [19, 40]. The ion release behaviors of the three alloys were similar to each other in c-SBF and in GF, separately within each fluid. However, in AS, the ion release behavior of the thin wire was significantly different as compared to the plate and the thick wire specimens (Table 2.4). Specifically, ion release began at day 1 and gradually increased through day 30 for the thin wire, while for the thick wire, ion release was observed on only day 30, and no ion release was detected for the plate specimen at all. This behavior is attributed to the high density of processing marks on thin wire, which constitute stress concentration points and possible crack initiation sites that are more prone to corrosion and ion release. The amounts of ion release detected in AS were also lower than the critical value for all samples, however; plate and thick wire samples appeared to be safer for use in AS.

**Table 2.5.** Ni and Ti ion releases in GF. The "-" indicates that measured ion concentration was below the detection limit [1] .

| | **„Plate in GF“** | | **„TKW in GF“** | | **„TNW in GF“** | |
|---|---|---|---|---|---|---|
| | $c$(Ni) / mg·l$^{-1}$ | $c$(Ti) / mg·l$^{-1}$ | $c$(Ni) / mg·l$^{-1}$ | $c$(Ti) / mg·l$^{-1}$ | $c$(Ni) / mg·l$^{-1}$ | $c$(Ti) / mg·l$^{-1}$ |
| **Day 1** | - | - | 0.018 ± *0.005* | - | 0.024 ± *0.001* | - |
| **Day 7** | 0.042 ± *0.001* | 0.006 ± *0.001* | 0.258 ± *0.005* | 0.090 ± *0.002* | 0.168 ± *0.003* | 0.066 ± *0.005* |
| **Day 14** | 0.138 ± *0.005* | 0.102 ± *0.003* | 0.288 ± *0.005* | 0.144 ± *0.005* | 0.264 ± *0.009* | 0.126 ± *0.002* |
| **Day 30** | 0.414 ± *0.007* | 0.318 ± *0.004* | 0.498 ± *0.008* | 0.288 ± *0.005* | 0.444 ± *0.019* | 0.276 ± *0.001* |

Plate samples exhibited lower amounts of ion release as compared to thick wires and thin wires in AS and GF. As AS and GF are both acidic fluids, they are more corrosive especially for specimens with surface defects, such as processing marks. Since plate samples did not possess distinctive processing marks as in the cases of thick and thin wires, they are less prone to these aggressive environments. This clearly indicates that geometry is an important factor contributing to the ion release behavior of the alloys.

When the ion release behaviors of the 30-day samples were evaluated in correlation with the oxide layer thickness data (Figure 2.4), it was observed that less ion release was prevalent through thicker oxide layers of the samples immersed in AS and SBF. Normally, thicker oxide layers are expected to lead to more intense ion release due to the possible mechanical defects they contain. The reason that the opposite behavior was observed for AS and SBF could be the C deposition on samples immersed in AS and SBF, which resulted from the high C content of these fluids. The deposited C could be blocking the mechanical defects of the oxide layer through which ion release is expected to occur. On the contrary, larger amount of ion release was observed from samples immersed in GF, as expected (Figure 2.3). This can be attributed to the C-free chemical content of GF, such that the mechanical defects of the oxide layers on samples immersed in GF remained without being blocked, leading to enhanced ion release despite the thicker oxide layers.

One important point of discussion regarding the oxide layers is that, for many biomedical applications, NiTi alloys usually feature a very thin protective oxide layer formed during initial processing in order to prevent corrosion or random oxidation [17, 18]. However, this layer can also contain defects or can crack prior to or during utility, and thus, may lose its protective property and become prone to ion release through these defects. Thus, it is essential to investigate the ion release and oxide layer formation behavior of NiTi alloys in simulated body fluids regardless of the presence of a protective oxide layer or previous oxidation

procedure for enhanced safety. This constituted one of the major motivations of the current work, and a rightful concern as evidenced by the thorough experimental analysis presented herein.

This issue becomes especially important considering the fact that the current biocompatibility analysis was limited to a maximum time period of 30 days, mainly because 30 days is a representative period of time to observe significant changes (if any) in the alloy properties with the aid of immersion experiments. Accordingly, a 30-day experimentation period can be considered a practical time span to comment on the general biocompatibility behavior of the alloy in selected environments. However, implants are made with the intention of aiding patients for much longer time periods expressed in years or decades, and thus, experiments simulating the long-term alloy behavior are very much needed.

## 2.4 Conclusion

In the current study, biocompatibilities of NiTi alloy samples with three different geometries were investigated in a comparative manner via immersion experiments in fluids that simulate three different human body parts. Specifically, NiTi samples with three different geometries were immersed in three different fluids simulating different body parts, and four different time periods were considered in the experiments. The changes observed in alloy surfaces and chemical contents of fluids upon immersion experiments in simulated body fluids were analyzed in terms of ion release, passive oxide layer formation, and surface layer chemical content. The results indicate that both geometry and processing background significantly affect the biocompatibility since they dictate the starting surface properties. Specifically, the different processing methods that were applied to obtain certain geometries induced substantial differences in the surface properties of the alloys, which significantly influenced the biocompatibility of the material. Thus, the current results can be interpreted,

such that sample geometry and surface quality should be considered as a single major parameter dictating the biocompatibility of the alloy.

Furthermore, each geometry appears to be safer than the others in a certain immersion fluid, implying that they are more suitable for use in the corresponding body parts (e.g. plate in AS and GF, thick wire and thin wire in c-SBF). This also supports the finding that geometry-induced surface properties play a critical role on the biocompatibility of the NiTi alloy. Another important finding is that, despite the fact that all three NiTi alloys exhibited lower ion release than the critical value for medical applications in the three types of fluids upon a maximum immersion period of 30 days, in order to ensure the safety of the biomedical application involving this material, further experimental investigation for longer and realistic periods is warranted by the significant amounts of ion release reported herein.

This study was followed by the biocompatibility analysis of NiTi SMAs used for a different medical application, namely the superelastic orthodontic archwires, where the biocompatibility of these archwires was investigated from a critical point of view based on a comparison of laboratory and clinical conditions.

## 2.5 References

[1] S.M. Toker, D. Canadinc, H.J. Maier, O. Birer, Mater. Sci. Eng. C, 36 (2014) 118–129.

[2] T. Duerig, A. Pelton, D. Stöckel, Mater. Sci. Eng. A 273 (1999) 149–160.

[3] D. Mantovani, JOM 52 (2000) 36-44.

[4] K. Otsuka, X. Ren, Intermetallics 7 (1999) 511-528.

[5] A.Roguin E. Grenadier, S. Linn, W. Markiewicz, R. Beyar, Am. Heart J. 138 (1999) 323-333.

[6] G. Mani, M.D. Feldman D. Patel, C.M. Agrawal, Biomaterials 28 (2007) 1689–1710.

[7] B. Thierry, Y. Merhi, L. Bilodeau, C. Trepanier, M. Tabrizian, Biomaterials 23 (2002) 2997–3005.

[8] A. Bansiddhi, T.D. Sargeant, S.I. Stupp, D.C. Dunand, Acta Biomater. 4 (2008) 773–782.

[9] M.F. Chen, X.J. Yang, R.X. Hu, Z.D. Cui, H.C. Man, Mater. Sci. Eng. C 24 (2004) 497–502.

[10] C.L. Chu, C.Y. Chung, P.H. Lin, S.D. Wang, Mater. Sci. Eng. A 366 (2004) 114–119.

[11] X. Liu, S. Wu, K.W.K. Yeung, Y.L. Chan, T. Hu, Z. Xu, X. Liu, J.C.Y. Chung, K.M.C. Cheung, P.K. Chu, Biomaterials 32 (2011) 330-338.

[12] O. Prymak, A. Klocke , B. Kahl-Nieke, M. Epple, Mater. Sci. Eng. A 378 (2004) 110–114.

[13] X. Li, J. Wang, E. Han, W. Ke, Acta Biomater. 3 (2007) 807–815.

[14] H.H. Huang, Y.H. Chiu, T.H. Lee, S.C. Wu, H.W. Yang, K.H. Su, C.C. Hsu, Biomaterials 24 (2003) 3585–3592.

[15] Y. Oshida, Bioscience and Bioengineering of Titanium Materials, first ed., Elsevier, Great Britain, 2007.

[16] G.S. Firstov, R.G. Vitchev, H. Kumar, B. Blanpain, J. Van Humbeeck, Biomaterials 23 (2002) 4863–4871.

[17] S.A. Shabalovskaya, H. Tian, J. W. Anderegg, Dominique U. Schryvers, W.U. Carroll, J.V. Humbeeck, Biomaterials 30 (2009) 468–477.

[18] H. Tian, D. Schryvers, D. Liu, Q. Jiang, J.V. Humbeeck, Acta Biomater. 7 (2011) 892–899.

[19] D. Vojtech, M. Voderova, J. Fojt, P. Novak, T. Kubasek, Appl. Surf. Sci. 257 (2010) 1573-1582.

[20] G. Rondelli, Biomaterials 17 (1996) 2003-2008.

[21] N. Figueira, T.M. Silva, M.J. Carmezim, J.C.S. Fernandes, Electrochimica Acta 54 (2009) 921–926.

[22] P. Rocher, L. El Medawar, J.-C. Hornez, M. Traisnel, J. Breme, H.F. Hildebrand, Scripta Mater. 50 (2004) 255–260.

[23] T. Hanawa, Mater. Sci. Eng. C 24 (2004) 745–752.

[24] T. Hanawa, Mater. Sci. Eng. A 267 (1999) 260–266.

[25] Y. Okazaki, E. Gotoh, Corrosion Sci. 50 (2008) 3429–3438.

[26] R. Hang, S. Ma, V.Ji, P.K. Chu, Electrochimica Acta 55 (2010) 5551-5560.

[27] J. Khalil-Allafi, B. Amin-Ahmadi , M. Zare, Mater. Sci. Eng. C 30 (2010) 1112–1117.

[28] R.R. Al-Hity, H.F. Kappert, S. Viennot,F. Dalard, B. Grosgogeat, Dent. Mater. 23 (2007) 679–687.

[29] J. Hou, Q.J. Peng, T. Shoji, J.Q. Wang, E-H. Han, W. Ke, Corrosion Sci. 53 (2011) 2956–2962.

[30] T. Tsuru, Y. Kaji, T. Tsukada, Y. Shibutani, Prog. Nucl. Sci. Technol. 2 (2011) 20-23.

[31] R. Huang, Y. Han, Mater. Sci. Eng. C 33 (2013) 2353–2359.

[32] Y. Estrin, E.P. Ivanova, A. Michalska, V.K. Truong, R. Lapovok, R. Boyd, Acta Biomater. 7 (2011) 900–906.

[33] T. Niendorf, D. Canadinc, H.J. Maier, I. Karaman, Scripta Mater. 60 (2009) 344–347.

[34] W. Zhang, M. Li, Q. Chen, W. Hu, W. Zhang, W. Xin, Mater. Des. 39 (2012) 379–383.

[35] P. Minárik, R. Král, M. Janecek, Appl. Surf. Sci. (2013), http://dx.doi.org/10.1016/j.apsusc.2012.12.096.

[36] J.T. Mayer, U. Diebold, T.E. Madey, E. Garfunkel, J. Electron Spectroscopy Relat. Phenom. 73 (1995) 1-11.

[37] C.S. Fadley, J. Electron Spectroscopy Relat. Phenom. 178 (2010) 2–32.

[38] M. Horgnies, E.Darque-Ceretti, H.Fezai, E.Felder, Int. J. Adhesion & Adhesives 31 (2011) 238–247.

[39] A.C. Guyton, J.E. Hall, Textbook of Medical Physiology, eleventh ed., Elsevier Saunders, Philadelphia, 2006.

[40] L. Somogyi, R. Chuttani, J. Croffie, J. DiSario, J. Liu, D.S. Mishkin, R. Shah, W. Tierney, L.M. Wong Kee Song, B.T. Petersen, Gastrointest. Endoscopy, 63 ( 2006) 910-919.

# 3 CHAPTER 3: EVALUATION OF BIOCOMPATIBILITY OF NiTi DENTAL WIRES: A COMPARISON OF LABORATORY EXPERIMENTS AND CLINICAL CONDITIONS [1]

## 3.1 Introduction

Various medical treatments, including dental and orthopedic implants, cardiovascular stents and orthodontic arch wires, widely employ Nickel-Titanium (NiTi) shape memory alloys (SMAs) as biomaterials owing to their superior shape memory effect or the pseudoelasticity property [2-7]. The pseudoelastic property of NiTi is especially important in the case of orthodontic arch wires, since it enables the material to attain relatively large strains without being plastically deformed under applied loading due to austenite-to-martensite phase wtransformation that is reversible upon unloading [2-4]. Specifically, the pseudoelastic NiTi arch wires undergo an austenite-to-martensite phase transformation upon the application of stress beyond the elastic region, such that they can be deformed further to relatively large strains while the stress remains constant [2, 4, 7]. As a result, the ability of pseudoelastic NiTi arch wires to maintain a constant stress state as the teeth are displaced throughout the treatment completely eliminates the costly and relatively uncomfortable readjustments of arch wires made of other alloys [7-10].

Owing to the advantages brought about by the pseudoelasticity, NiTi alloys have been widely used as orthodontic arch wires for decades, however; biocompatibility of these superior alloys is still subject to debate [11, 12]. It is well known that exposure to Ni resulting from the Ni release into the intraoral environment can cause adverse reactions inside and around the oral cavity, such as gingival hyperplasia, inflammation around the lips (angular chelitis), swelling and burning sensations in the oral mucosa, especially in the case of Ni hypersensitivity of the patient [12]. Thus, the factors which affect the biocompatibility of the

arch wires, such as Ni release and passive oxide layer formation on the wire, need to be investigated very carefully and in great detail from several angles, to ensure a safer use of the NiTi alloys in this application. This requires suitable *ex situ* simulation of the conditions that the wires will be subjected to during treatment, which is the intraoral environment.

Previous works focusing on the evaluation of biocompatibility of NiTi wires in *ex situ* conditions mainly relied on static or mechanic immersion experiments in artificial saliva at body temperature [11, 13-16]. However, in actual intraoral conditions, additional factors come into picture, such as the patient's age, gender or nutritional habits [17], which affect the acidity of the environment or relative amounts of ingredient elements of the saliva. In order to realistically simulate the chemical composition and pH of the actual intraoral environment, the following approaches were adopted previously [11, 13-16]: (i) addition of higher amounts of certain ions, such as Fluoride (F) or Chloride (Cl), to simulate certain nutritional habits [13, 15], and (ii) adjusting the saliva acidity to low pH values in order to simulate the aggressive environment caused by dental plaque [11, 16]: while Lee *et al.* concluded that the surface degradation of NiTi wires depend mainly on the chemical composition of the oxide layer [13], Pyrimak *et al.* observed that fatigue resistance of NiTi wires were lower in immersion fluids [14], Furthermore, Li *et al.* demonstrated that corrosion occurs locally in Cl-containing solution, while general corrosion is prevalent in F-containing solution [15], and Huang *et al.* showed that pH and immersion period together dictate ion release [16]. All these findings imply that parameters specific to patient determine both the saliva properties and the corresponding effects on orthodontic wires [11, 13-16].

Even though the aforementioned *ex situ* studies provided valuable information, they focused on the effect of very specific material properties only, and fell short of providing any correlation with clinical conditions. Orthodontic arch wires retrieved from patients were also investigated, demonstrating that formation of a biofilm and precipitation of various organic

constituents may be observed on the wires, as well as changes on the wire surface or microstructure during the intraoral stay [17]. Effects of intraoral exposure on mechanical properties of the retrieved wires were examined, as well, yielding results on the variations of pseudoelastic property throughout the treatment [18]. However, the results of the clinical studies were very patient–oriented, and thus, difficult to draw general conclusions from.

Even though the biocompatibility of orthodontic wires were investigated in artificial or natural intraoral conditions separately, to the best of the authors' knowledge, a comprehensive comparison of the effect of laboratory and clinical conditions on the surface degradation of NiTi dental arch wires has not been forwarded yet. Consequently, the current study was undertaken to evaluate the applicability of the *ex situ* experiments focusing on the biomaterial utility in actual intraoral environment, as well as revealing the differences between the *ex situ* conditions and natural intraoral environment, and deficiencies in biocompatibility testing of orthodontic arch wires. For this purpose, static immersion experiments were carried out on commercial as-is NiTi orthodontic arch wires in artificial saliva, and the *ex situ* tested NiTi orthodontic arch wires were compared with companion wires retrieved from the patient in terms of surface properties through energy dispersive X-ray spectroscopy (EDX) analysis. The results revealed significant differences in both the chemical compositions and surface oxide layer formation behaviors. Outcomes of the current study are expected to contribute to construction of a more realistic testing methodology for biocompatibility analysis of NiTi arch wires, which will also be useful while designing new orthodontic arch wire materials in the future.

## 3.2 Experimental Details

In the current work, dental wires retrieved from patients and those immersed in artificial saliva were investigated and compared in terms of the surface changes that result from exposure to natural and artificial saliva, respectively. While the dental wires retrieved from the patients were exposed to intraoral environment for 30 days, companion dental wires were subjected to static immersion experiments in artificial saliva for periods of 1, 7, 14 and 30 days. The static immersion test samples had a length of 1.5 cm, and each sample was immersed in 0.5 ml of artificial saliva. An immersion test sample and a wire retrieved from patient after intraoral exposure of 30 days are presented in Figure 3.1 (a) and (b), respectively. The temperature was kept constant at 37 °C in the experiments for simulating the body temperature. The wires immersed for different time periods were kept in separate sealed tubes during immersion, and the sealed tubes were immersed in an electronically-controlled water bath. Prior to the experiments, it was ensured that all the prepared fluids were stable solutions and remained stable during the experiments, as evidenced by the fact that no salt deposition was observed in any of the fluids. The chemical content and the pH value of the prepared artificial saliva are presented in Table 3.1. Normally, the pH of the natural saliva is about 7, however; in order to simulate the low pH value induced by the dental plaque and the acidic environment that can be caused by nutritional habits [13, 15, 19], a lower pH value was preferred in the current study. The pH of the artificial saliva was adjusted by slowly adding 1M HCl into the solution, until the targeted pH value of 2.3 was obtained.

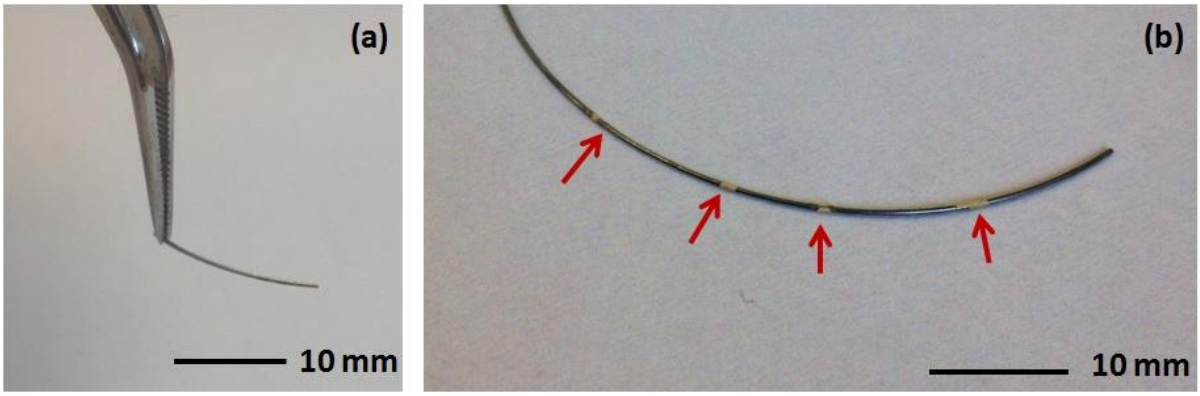


**Figure 3.1.** Orthodontic wires used in the current experiments: **(a)** as-is wire, **(b)** wire retrieved from the patient upon 30 days of intraoral exposure: the noteworthy structures formed on the wire surface upon intraoral exposure are marked with red arrows [1].

**Table 3.1.** Chemical content of artificial saliva used in immersion experiments [1].

| Solution | Ingredients | Amount of Ingredients (g/l) | pH |
|---|---|---|---|
| Artificial Saliva | NaCl | 0.4 | 2.3 |
| | KCl | 0.4 | |
| | $CaCl_2 \cdot 2H_2O$ | 0.906 | |
| | $NaH_2PO_4 \cdot 2H_2O$ | 0.690 | |
| | $Na_2S \cdot 9H_2O$ | 0.005 | |
| | Urea | 1 | |

All samples were cleaned with ethanol in an ultrasound bath prior to the experiments. The surfaces of the as-is wires were observed with scanning electron microscope (SEM) (Figure 3.2(a)) and EDX (Figure 3.3) in detail prior to the immersion experiments. Following the immersion experiments and intraoral exposure, the wires were investigated once more with SEM and EDX, in order to analyze the wire surfaces and determine the chemical compositions of the new structures that form on the wires during the experiments in artificial and natural saliva. The SEM and EDX analyses were conducted on a Zeiss Ultra Plus field emission scanning electron microscope.

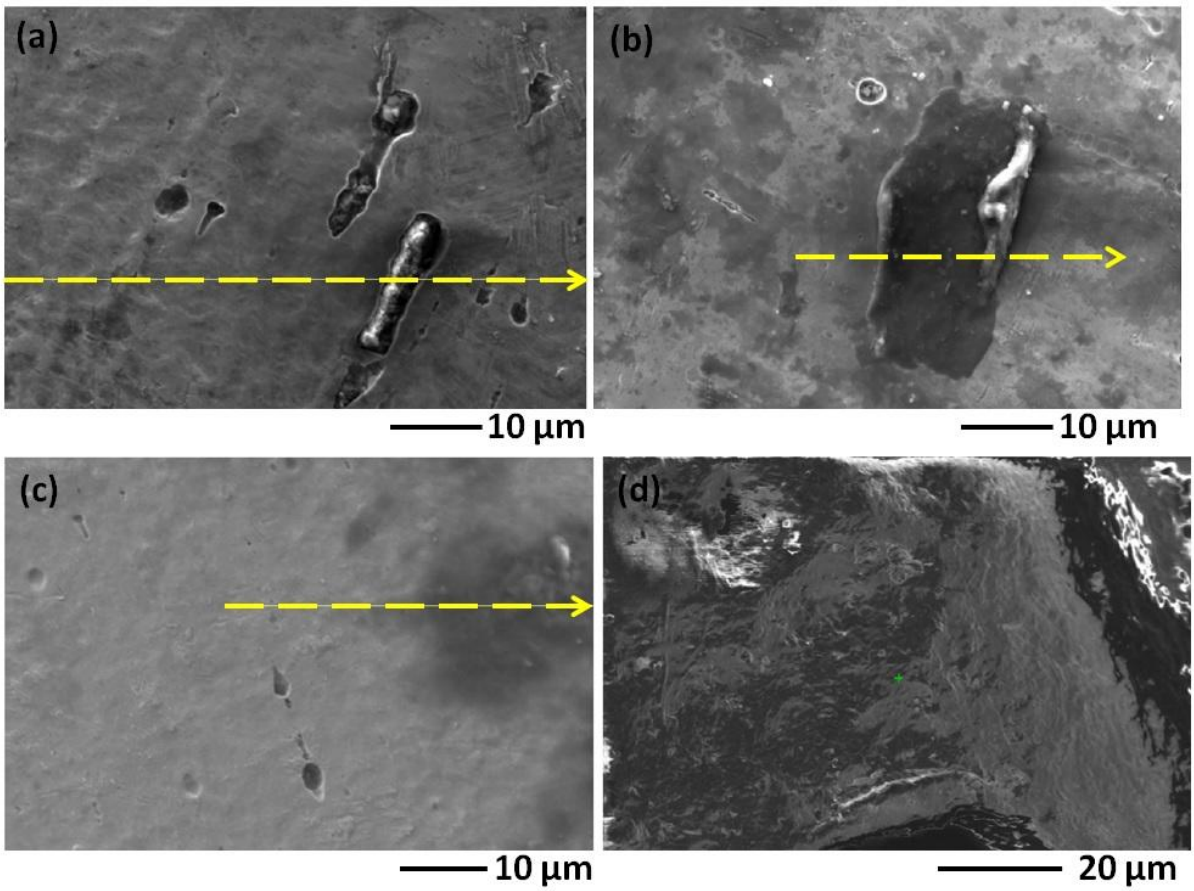


**Figure 3.2.** SEM images of the orthodontic wires: **(a)** as-is wire, **(b)** wire immersed in artificial saliva for 30 days, **(c)** wire retrieved from the patient after 30 days of intraoral exposure, **(d)** the new structure that formed on the wire retrieved from the patient after 30 days of intraoral exposure at higher magnification. The yellow dashed lines indicate the band along which EDX analysis were conducted [1].

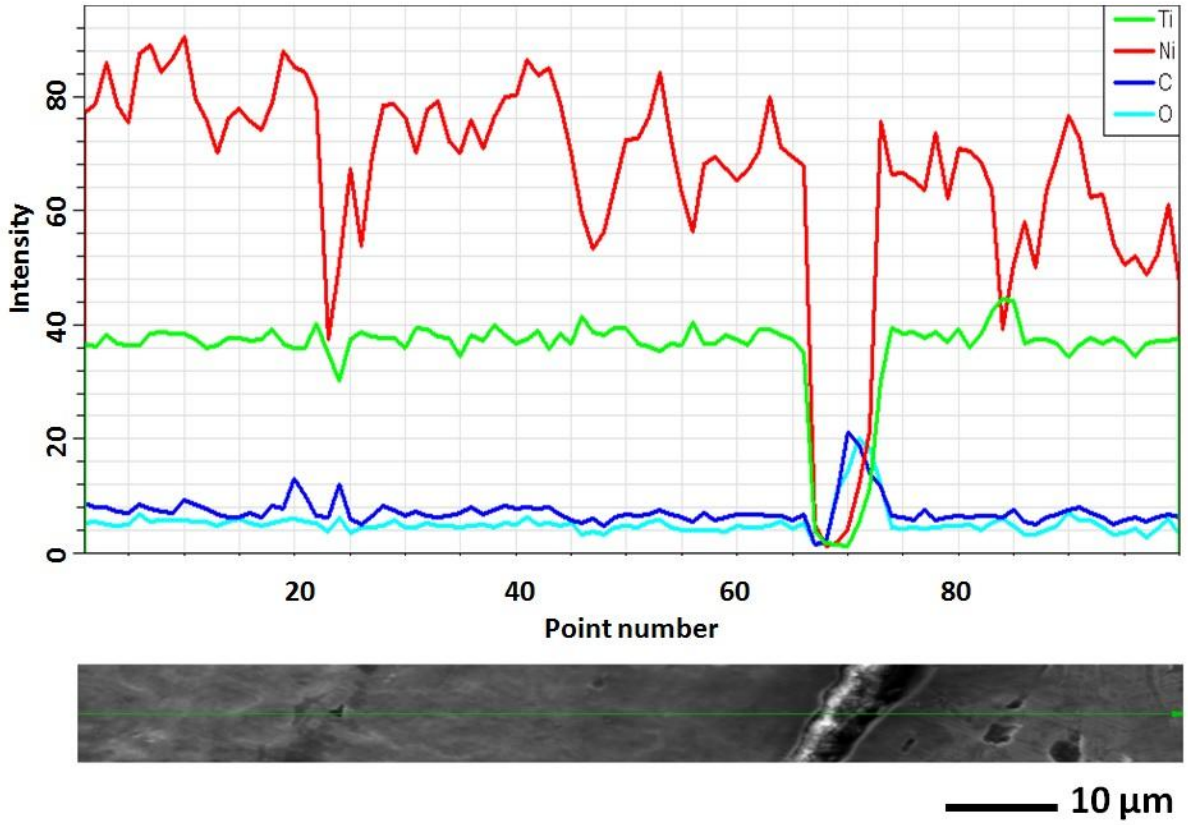


**Figure 3.3.** EDX profile of as-is dental wire [1].

## 3.3 Results and Discussion

The surfaces of wires both retrieved from the patients and those tested *ex situ* were investigated via EDX in order to examine the changes on the specimen surfaces and determine the chemical composition of new structures that formed on the specimens during exposure to artificial saliva or natural oral environment. The EDX line profiles of representative regions of the as-is, immersed and retrieved wires are presented in Figures 3.3-3.7. In the current EDX line profiles, instead of concentration plots, intensity plots of Ni, Ti, C and O elements were used, in order to compare the relative amounts of the analyzed elements. Representative regions, which contain significant new structures, were examined by

EDX to identify these structures. The SEM images are presented below the corresponding EDX profiles in Figures 3.3-3.7.

A detailed examination of the EDX results revealed that the EDX profile of the as-is wire exhibits stable trends of signals for all the analyzed elements (Figure 3.3). The two fluctuations observed in the Ni signal correspond to the regions with impurities, such as P and Ca containing foreign particles as identified by the quantitative EDX analysis (Table 3.2). The SEM observation of the as-is wire surface evidences traces of processing marks in addition to rare impurities (Figure 3.2(a)). Besides the impurities and processing marks, the as-is wire exhibits a quite smooth surface, which indicates the absence of any special structures or features on the as-is wire surface that should be taken into account while making a comparison to the wires immersed in artificial saliva or retrieved from the patient.

**Table 3.2.** Relative quantities of the elements in weight and atomic percentage (wt.% and at.%), which were detected on the impurity regions on the as-is orthodontic wire [1].

| **Element** | **wt.%** | **at.%** |
|---|---|---|
| Nickel | 0.60 | 0.40 |
| Titanium | 0.60 | 0.50 |
| Oxygen | 0.00 | 0.00 |
| Nitrogen | 0.00 | 0.00 |
| Chlorine | 0.60 | 0.67 |
| Fluorine | 0.00 | 0.00 |
| Sodium | 0.60 | 1.03 |
| Calcium | 86.57 | 85.67 |
| Magnesium | 0.60 | 0.98 |
| Potassium | 9.83 | 9.98 |
| Phosphorus | 0.60 | 0.77 |
| Carbon | 0.00 | 0.00 |
| Sum | 100 | 100 |

The EDX profiles of the wires immersed in artificial saliva for 1, 7 and 14 days demonstrate similar trends to each other, and thus, the EDX profile of only the 7-day sample is provided as the representative profile (Figure 3.4). Specifically, the Ni signals of these three wires exhibit slight fluctuations in the vicinity of the dark structures present on the surface, however; none of the other three elements analyzed (Ti, O, C) have significant signals or peaks associated with these dark structures (Figure 3.4), indicating that these structures belong to a Ni-rich inner phase rather than precipitates originating from the immersion fluid. It has been previously shown that, diffusion of Ni atoms from surface into the inner layers is triggered during the oxidation process of NiTi [20]. This process causes some of the diffusing atoms to join the existing inner $Ni_3Ti$ layer and some to exist as free Ni underneath the oxide layer [20]. In the case of current samples immersed into artificial saliva for 1, 7 and 14 days, the inner $Ni_3Ti$ layer or the free Ni underneath the surface could have come out during the immersion due to the electrochemical dissolution of the wire surface facilitated by the acidic and aggressive nature of the artificial saliva. Thus, considering the increased Ni signal originating from the dark structures and the previous evidence on the formation of $Ni_3Ti$ layer or accumulation of free Ni right underneath the surface due to oxidation [20], it can be argued that the observed dark structures belong to a $Ni_3Ti$ layer or free Ni, which emerge as a result of surface erosion. Moreover, the quantitative EDX data evidenced that, the dark structures observed on the day 1, 7 and 14 samples have a chemical composition with about 45 at. % Ni and 55 at. % Ti (Table 3.3). According to the Ti-Ni phase diagram, the phase corresponding to the detected atomic percentages is $Ti_2Ni+TiNi_3$ [21], which agrees well with the EDX line profile findings.

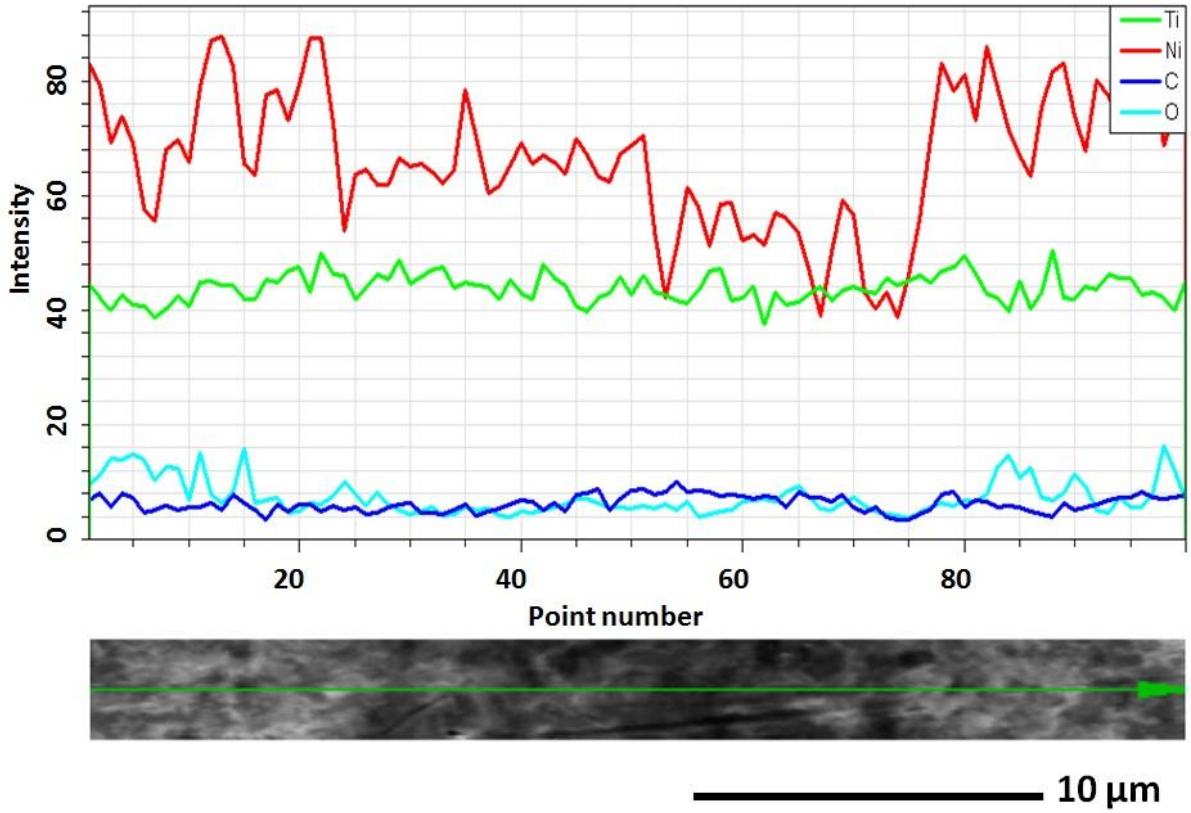


**Figure 3.4.** EDX profile of dental wire immersed in artificial saliva for 7 days [1].

**Table 3.3.** Relative quantities of the elements detected on the dark structures present on the dental wires immersed in artificial saliva for 1, 7 and 14 days., given in weight and atomic percentage (wt. % and at. %) [1].

| Element | wt.% | at.% |
|---|---|---|
| Nickel | 50 | 44.93 |
| Titanium | 50 | 55.07 |
| Carbon | 0 | 0 |
| Oxygen | 0 | 0 |
| Sum | 100 | 100 |

The sample subjected to static immersion for a 30-day period, on the other hand, exhibited particles on the surface (Figure 3.2(b)). The corresponding EDX profile reveals that this particle is a C-rich structure as evidenced by the increased C signal in its vicinity (Figure 3.5). Considering the C-rich chemical formulation of artificial saliva, formation of a new

structure with high C content on the wire surface due to immersion is reasonable. Formation of this structure upon a 30-day immersion and its absence in the samples subjected to static immersion for shorter periods implies that the acidic erosion reaches a saturation point in the later stages of immersion, allowing new structures to form on the wire surface. In clinical conditions, the chemistry of the intraoral environment can be altered due to the interaction between the metal, micro-organisms and metabolic by-products [12]. Over time, a proteinacious film forms on the wire due to exposure to saliva [17]. This film acts as a protective layer under acidic conditions, preventing wire surface erosion [17]. Accordingly, it can be deduced that acidic erosion and protective film formation on the wire compete with each other during the early stages of exposure to saliva. At extended periods of exposure, the proteinacious film formation rate overcomes the acidic erosion rate, allowing protein products and new structures to accumulate on the wire surface. Thus, based on the current static immersion experiment results, it can be concluded that the proteinacious film on the wire reaches a stable state upon 30 days of immersion in artificial saliva and leads to the formation of new structures on the surface. The quantitative EDX analysis also evidences that a proteinacious film is present on the dental wire immersed in artificial saliva for 30 days since a remarkable amount of C and N, the constituent elements for proteins, were detected on the 30-day sample (Table 3.4).

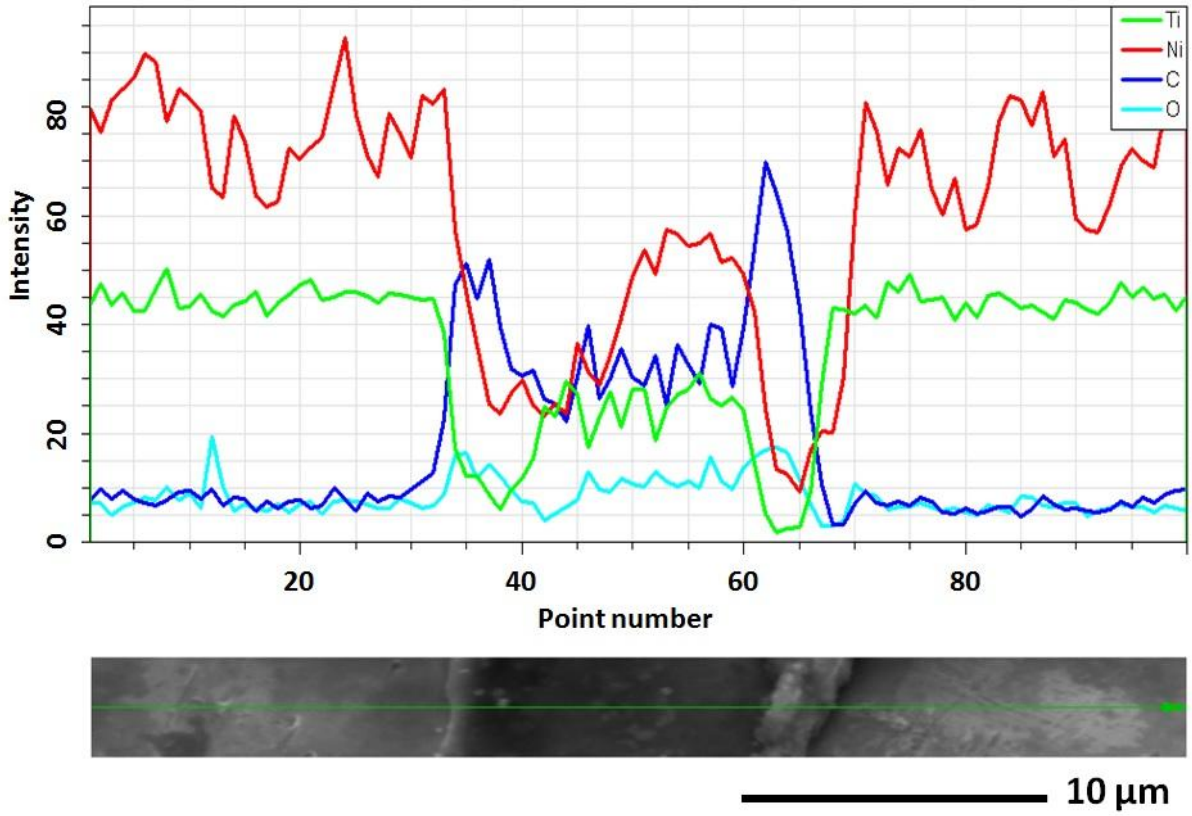


**Figure 3.5.** EDX profile of dental wire immersed in artificial saliva for 30 days [1].

**Table 3.4.** Relative quantities of the elements detected on the particles present on the dental wire immersed in artificial saliva for 30 days, given in weight and atomic percentage (wt. % and at. %) [1].

| Element | wt.% | at.% |
|---|---|---|
| Nickel | 0.00 | 0.00 |
| Titanium | 0.33 | 0.09 |
| Carbon | 31.00 | 34.66 |
| Oxygen | 0.00 | 0.00 |
| Nitrogen | 67.57 | 64.77 |
| Phosphorus | 1.10 | 0.48 |
| Sum | 100 | 100 |

Deposition of foreign particles from the solution on the wire surfaces was also observed on the two wires retrieved from the patient (Figures 3.2 (c) and (d)). Especially on one of the wires, these structures are even visible to the naked eye (Figure 3.1(b)). These new

noteworthy structures on the wire are marked with red arrows in Figure 3.1(b) and an SEM image of one of these structures is provided in Figure 3.2(d). EDX profiles and quantitative EDX data of these two wires evidence that these new structures are also C-containing compounds, specifically fluorocarbon compounds, as they were found to consist of mainly C and F based on the quantitative EDX analysis (Figures 3.6 and 3.7, Table 3.5). Formation of a C containing compound is an expected and reasonable result considering the high C content of natural saliva (as in the case of artificial saliva). The high F content on the other hand, should be a result of the nutritional habits of the patient, as F is not one of the constituents of natural or artificial saliva [19]. However, formation of large piles of these C-containing structures is related to physical factors rather than the chemical content of the natural saliva. Specifically, the contact points of wires with brackets create sites for accumulation of new phases due to both macroscopic and microscopic reasons. At the macroscopic scale, these sites act as protrusions, which the freely flowing particles in the saliva can attach to, forming new structures on the surface. At the microscopic scale, on the other hand, reactivity of the metal increases at the contact sites between the arch wire and the brackets, and the wire becomes more prone to corrosion [12]. Moreover, as the wire and the brackets are exposed to higher amount of stresses at the contact sites due to their interaction with each other, dislocations are generated at these sites beyond the expected pseudolastic behavior of shape memory alloys, and thus, higher energy is concentrated around these contact points [22-23]. Previous studies have shown that such high energy regions constitute ideal sites for the precipitation of new structures, as they are more reactive and require less amount of energy for new structures to form and accumulate [24-25]. Thus, the C pile-ups preferentially form on these high energy regions, which are the contact points between wires and brackets. Localization of these visible structures on the wire with equal intervals (Figure 3.1(b)),

strengthens the argument that the pile-ups form on the contact surfaces of wires with brackets, since wires are attached to brackets on each tooth with equal intervals.

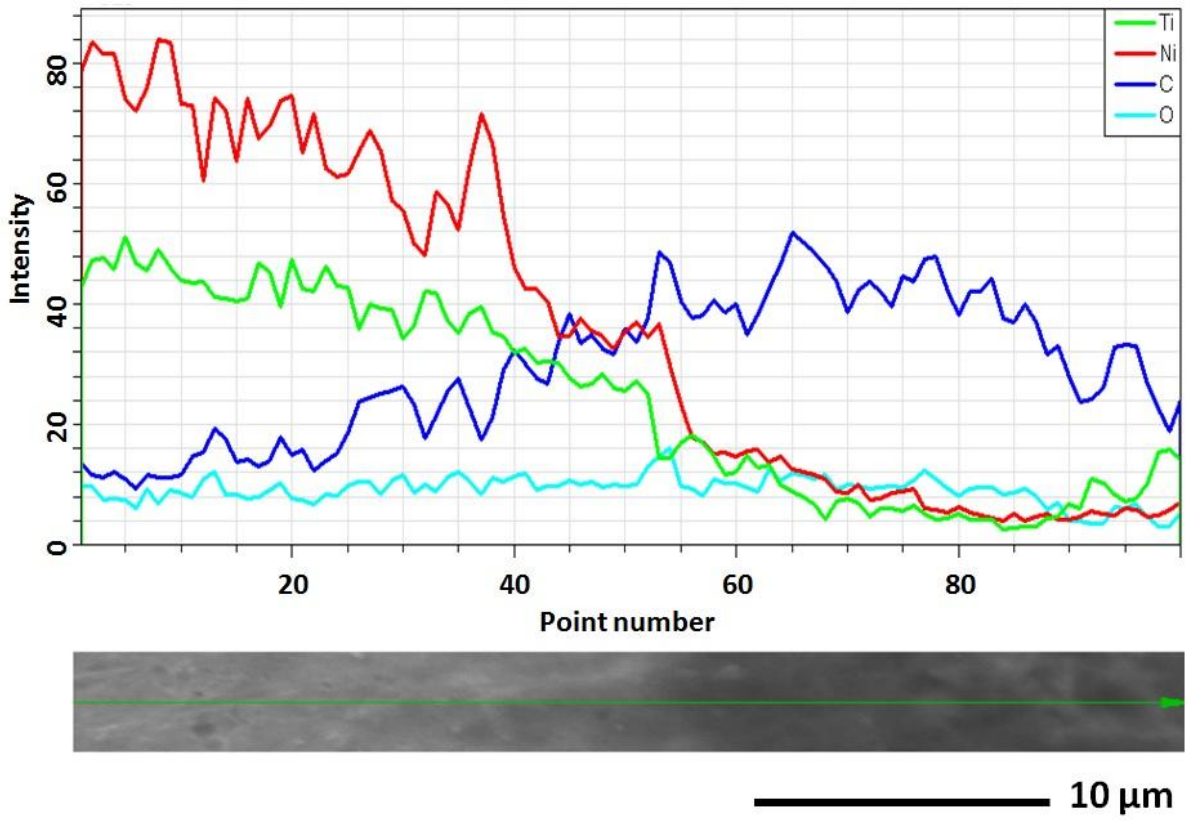


**Figure 3.6.** EDX profile of dental wire retrieved from the patient following 30 days of intraoral exposure [1].

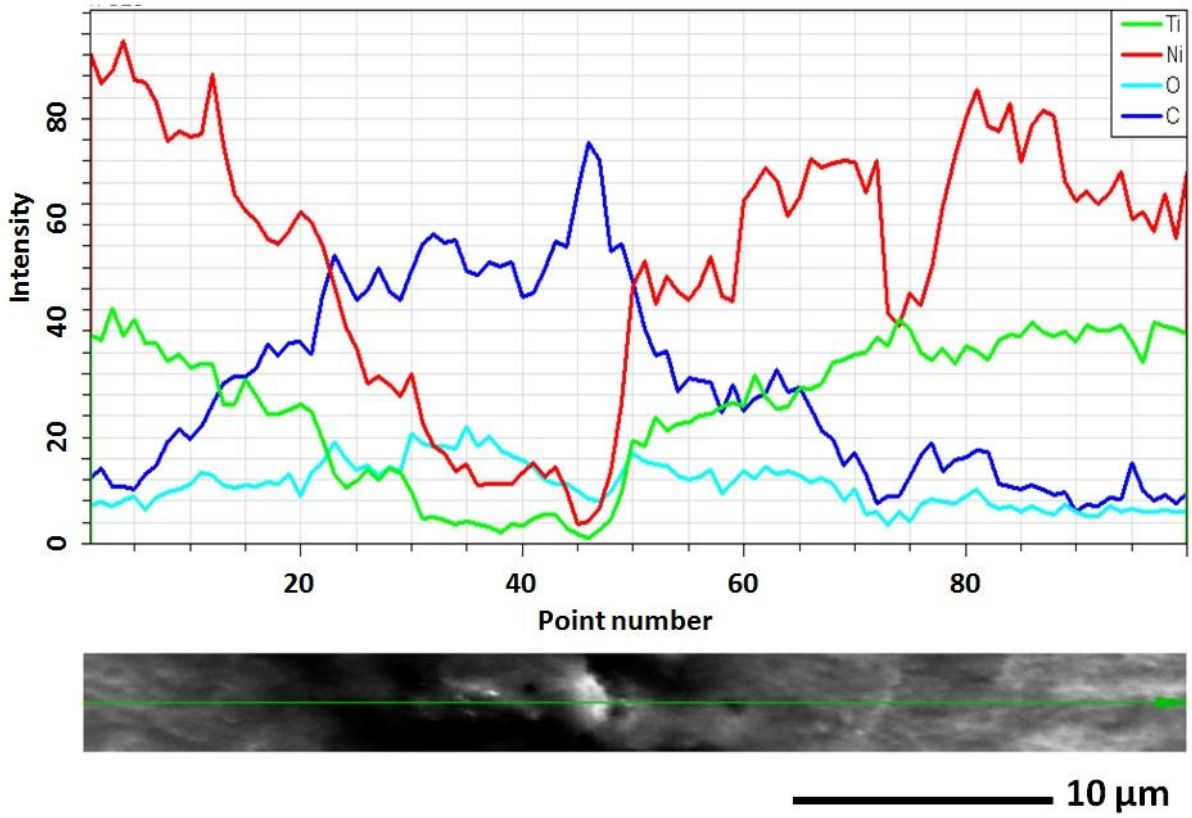


**Figure 3.7.** EDX profile of dental wire retrieved from the patient following 30 days of intraoral exposure [1].

**Table 3.5.** Relative quantities of the elements detected on the particles present on the dental wire retrieved from the patient following 30 days of intraoral exposure, given in weight and atomic percentage (wt. % and at. %) [1].

| Element | wt.% | at.% |
|---|---|---|
| Carbon | 34.59 | 45.55 |
| Oxygen | 0.00 | 0.00 |
| Fluorine | 65.40 | 54.45 |
| Sodium | 0.00 | 0.00 |
| Calcium | 0.00 | 0.00 |
| Chlorine | 0.00 | 0.00 |
| Titanium | 0.00 | 0.00 |
| Nickel | 0.00 | 0.00 |
| Potassium | 0.00 | 0.00 |
| Sum | 100 | 100 |

When the wires retrieved from the patient following a 30-day treatment are compared to those subjected to static immersion for 30 days, formation of C containing dark structures is evident on the surfaces of both types of samples (Figure 3.2(b)-(d)). This observation

indicates that the prepared artificial saliva is successful in terms of simulating the chemical content, especially in terms of the C content of the natural saliva. However, the C-rich pile-ups, which exhibit a significant presence on the wires retrieved from the patient, did not form on the wires immersed in artificial saliva. As these pile-ups form on the available sites for precipitation provided by the contact of wires with brackets, it is reasonable that a similar behavior was not observed on the immersed wires since these wires were not in contact with brackets throughout the immersion experiments. It should also be noted that the wires retrieved from the patient were compared with only the 30-day immersion samples since the intraoral exposure period of the retrieved wires were 30 days.

The current results demonstrated that the orthodontic wires that were immersed in artificial saliva and subjected to natural saliva for 30 days exhibited quite similar behaviors in terms surface degradation. This is an indication that the artificial intraoral conditions utilized in the current study resulted in a proper simulation of the actual clinical conditions in terms of chemical composition, pH and temperature. Results of the immersion experiments revealed that only the effects of the acidic erosion prevailed in earlier periods of immersion, whereas more stable structures formed on the wire surfaces following longer periods of immersion. This is enabled by the prevention of further acidic erosion by the protective layer, implying that accumulation of new structures follows an initial period of stabilization of the surface with the formation of a protective layer. The current data provides information about the time dependency of the formation of new structures on orthodontic wire surfaces during intraoral exposure, however; it is a controversial issue whether formation of new structures on top of the protective layer on the wire surfaces further contributes to the biocompatibility of the wire within the intraoral environment. Thus, further analysis is required to investigate the effect of the formation of new structures on the wires and intraoral cavity.

In addition to the remarkable findings about the behavior of orthodontic wires in artificial saliva which indicate that a certain period is required for the stabilization of the surface during immersion prior to formation of new structures, the current study also provides good evidence that *ex situ* experiments can successfully simulate the intraoral environment under static conditions in terms of C deposition. However, the current findings also demonstrated that these experiments fall short of simulating the additional C deposition and formation of new structures on the wire surfaces promoted by the wire-bracket contact. Thus, for the sake of a more realistic biocompatibility evaluation, the physical parameters the dental wires are subjected to (e.g. stresses) should also be simulated in addition to the chemical conditions of the intraoral environment. Future studies on investigating the biocompatibility of arch wires, should focus on the comparison of clinical conditions with *ex situ* conditions under mechanical loading, where the wires are positioned in contact with brackets.

## 3.4 Conclusions

The *ex-situ* behavior Nickel-Titanium (NiTi) orthodontic arch wires were investigated through static immersion experiments in artificial saliva, and the tested samples were then compared with companion wires retrieved from patients after exposure to intraoral conditions. The results indicated that, *ex situ* experiments provide valuable information about the phenomena that takes place during the immersion procedure, such that surface erosion due to the acidic environment is dominant at earlier stages of immersion, while a proteinacious protective film forms on the surface towards the end of the immersion period, which allows for the formation of C-rich particles that were also evident on the retrieved wires. Accordingly, the *ex situ* conditions applied in the current study successfully simulated the clinical conditions in terms of C deposition on the wire surfaces. However, formation of larger C pile–ups that were observed at the contact surfaces of the (retrieved) wires with

brackets were not detected following the static immersion experiments, indicating that *ex situ* conditions are not sufficient in terms of completely simulating the intraoral environment. Consequently, the current findings demonstrate that, in order to provide a more realistic simulation of the clinical conditions to be used in the biocompatibility evaluation of NiTi orthodontic arch wires, the experiments should simulate the intraoral environment in terms of both physical and chemical conditions, such as carrying out *ex situ* experiments under mechanical loading where the dental wires stay in contact with brackets under applied loading. In the following chapter, this issue was placed under focus and actual mechanical conditions were incorporated into ex situ static immersion experiment conditions for a more realistic biocompatibility testing of NiTi orthodontic archwires.

## 3.5 References


[1] S.M. Toker, D. Canadinc, Mater. Sci. Eng. C, 40 (2014) 142–147.

[2] T. Duerig, A. Pelton, D. Stöckel, Mater. Sci. Eng. A 273 (1999) 149–160.

[3] D. Mantovani, JOM 52 (2000) 36-44.

[4] C. Gıoka, T. Eliades, Hellenic Orthodontic Rev. 5 (2002) 111-127.

[5] G. Mani, M.D. Feldman D. Patel, C.M. Agrawal, Biomaterials 28 (2007) 1689–1710.

[6] A. Bansiddhi, T.D. Sargeant, S.I. Stupp, D.C. Dunand, Acta Biomater. 4 (2008) 773–782.

[7] R.J. Nikolai Semin. Orthodontics 3 (1997) 157-165.

[8] Z. Davidovitch,V. Krishnan, Am. J. Orthodontics Dentofac. Orthopedics 135 (2009) 222-231.

[9] H. Wehrbein, P. Göllner, J. Orofac. Orthopedics 6 (2007) 443-461.

[10] A. VanSchepdael, J.VanderSloten, L.Geris, J. Biomechanics 46 (2013) 470–477.

[11] S.M. Toker, D. Canadinc, H.J. Maier, O. Birer, Mater. Sci. Eng. C, 36 (2014) 118–129.

[12] K. House, F. Sernetz, D. Dymock, J.R. Sandy, A.J. Ireland, Am. J. Orthodontics Dentofac. Orthopedics 133 (2008) 584-592.

[13] T.H. Lee, C.C. Wang, T.K. Huang, L.K. Chen, M.Y. Chou, H.H. Huang J. Alloys Comp. 488 (2009) 482–489.

[14] O. Prymak, A. Klocke , B. Kahl-Nieke, M. Epple, Mater. Sci. Eng. A 378 (2004) 110–114.

[15] X. Li, J. Wang, E. Han, W. Ke, Acta Biomater. 3 (2007) 807–815.

[16] H.H. Huang, Y.H. Chiu, T.H. Lee, S.C. Wu, H.W. Yang, K.H. Su, C.C. Hsu, Biomaterials 24 (2003) 3585–3592.

[17] T. Eliades, G. Eliades, A.E. Athanasiou, T.G. Bradley, European J. Orthodontics 22 (2000) 317-326.

[18] N. Pandis, C P. Bourauel Semin. Orthodontics, 16 (2010) 249-257.

[19] R.R. Al-Hity, H.F. Kappert, S. Viennot, F. Dalard, B. Grosgogeat, Dent. Mater. 23 (2007) 679–687.

[20] H. Tian, D. Schryvers, D. Liu, Q. Jiang, J.V. Humbeeck, Acta Biomater. 7 (2011) 892–899.

[21] K. Otsuka, X. Ren, Prog. Mater. Sci. 50 (2005) 511–678.

[22] J. Hou, Q.J. Peng, T. Shoji, J.Q. Wang, E-H. Han, W. Ke, Corrosion Sci. 53 (2011) 2956–2962.

[23] T. Tsuru, Y. Kaji, T. Tsukada, Y. Shibutani, Prog. Nucl. Sci. Technol. 2 (2011) 20-23.

[24] R. Huang, Y. Han, Mater. Sci. Eng. C 33 (2013) 2353–2359.

[25] Y. Estrin, E.P. Ivanova, A. Michalska, V.K. Truong, R. Lapovok, R. Boyd, Acta Biomater. 7 (2011) 900–906.

# 4 CHAPTER 4: A CRITICAL APPROACH TO THE BIOCOMPATIBILITY TESTING OF NITI ORTHODONTIC ARCHWIRES [1]

## 4.1 Introduction

Nickel-Titanium (NiTi) alloys continue to attract significant attention in medicine due to their superior shape memory and pseudoelastic properties, especially in the fields of cardiovascular surgery and orthodontics [2–5]. The pseudoelastic behavior stands out in dental applications: for instance, in the case of orthodontic archwires, the pseudoelastic property of NiTi makes the application of constant stress possible over large tooth displacements [2,3], which not only minimizes tissue damage during treatment [6], but also eliminates expensive and troublesome readjustment procedures required for wires made of conventional materials, such as medical grade stainless steel [2,7–10]. Specifically, the austenite-to-martensite phase transformation above the austenite finish temperature and under straining beyond the elastic limit of the NiTi alloy leads to a state of constant stress, which is known as pseudoelasticity [11].

Despite their remarkable pseudoelastic capacity and wide utility in medical applications, the biocompatibility of NiTi alloys is still subject to debate, mainly due to potential Ni release from the surface, which can lead to serious health problems, especially in Ni-allergic patients [12,13]. In the case of dental applications, Ni ions released into the intraoral cavity may cause complications, such as burning sensations and inflammation around or in the mouth, and gingival hyperplasia [13]. The Ni ion release depends mainly on the applied stress state, and the properties of both the sample surface and the body fluid (or tissue) the sample comes into contact with. Specifically, it has been demonstrated that Ni ion release increases concomitant with both acidity of the fluid and plastic deformation due to applied stress [12,14]. Furthermore, the geometry of the sample has been demonstrated to

play a vital role in the ion release behavior, where the corresponding surface finish and properties dictate the amount of ion release along with the fluid contacting the material [12]. As for the effect of applied stress on the Ni ion release behavior, biocompatibility experiments featuring both static [6,14] and cyclic [15,16] loads on NiTi samples have been carried out, where the loading was restricted to simple three-point bending, which does not represent the actual stress state of archwires during clinical treatments. The importance of adopting a more realistic loading scenario becomes more clear once the possibility of stress-assisted corrosion cracking (SCC) is realized, where applied stress enhances crack initiation on the surface, and then crack propagation through the surface in corrosive environments [15]. In the case of NiTi alloys, the core of the material becomes exposed directly to the corrosive environment if the protective film that formed during the initial processing is damaged under applied stress, which leads to Ni decomposition and release [17]. In addition, the chemically-, thermally- or stress-induced changes in the surface properties, such as surface roughness and morphology, promote crack initiation and/or propagation due to dissolution [18–20].

Despite the findings forwarded on the Ni ion release and corrosion behavior of NiTi orthodontic wires [6,12–16,20–25], to the best of the authors' knowledge, an investigation focusing on the biocompatibility and Ni ion release behavior of NiTi alloys in the presence of SCC, and under realistic chemical and mechanical loading conditions has not been forwarded yet. The current work was undertaken with the motivation of addressing this issue, such that laboratory experiments closely simulating the actual clinical conditions were designed and carried out on commercially available NiTi orthodontic archwires. For this purpose, static immersion experiments in artificial saliva (AS) were carried out, such that the NiTi wires were subjected to AS for 31 days while attached to brackets fixated on upper dental arch mold model of an actual patient. Following the immersion experiments, both the NiTi archwires and the immersion fluids were thoroughly inspected for changes in surface properties and

chemical contents. The current results indicate that the deposition of new structures on the surface, such as C- and Ca-rich corrosion products, differs significantly between the undeformed and bound archwires. Specifically, the stress concentration building up at the contact points of archwire with the brackets induces SCC, which leads to micro-crack formation on the archwire surface. Moreover, these micro-cracks constitute ideal sites for the deposition of the aforementioned new structures and dictate ion release from the wire owing to the high surface energy they possess. Overall, the current findings clearly demonstrate that a realistic biocompatibility assessment of orthodontic archwires necessitates the incorporation of both mechanical and chemical conditions of the intraoral cavity into the laboratory experiments.

## 4.2 Experimental Procedure

The current work employed static immersion experiments in AS in order to investigate the stress-assisted corrosion-induced changes in the surface properties of and possible ion release from NiTi orthodontic archwires in intraoral cavity. Specifically, 18' slot 3M Unitek Gemini Roth metal brackets[1] were fixated to a dental mold model of the upper dental arch of an actual patient. Metal brackets were bonded with light cure adhesive (3M Unitek Transbond XT). The dental mold models were obtained from standard plastic upper jaw models for duplication, where alginate was used as impression material. Dental plaster was then cast into the alginate model and the obtained hard dental plaster was used as the dental mold.

The commercially available NiTi archwires[2] were placed into the bracket slots with the following sequence: both bonding of the brackets and the binding procedure were performed from upper left second premolar to upper right second premolar. The NiTi

[1] 18' slot 3M Unitek Gemini Roth brackets and the corresponding metallic bases were manufactured from17-4PH and 304L stainless steels, respectively.
[2] 3M Unitek Smart Clip Nitinol heat activated archwires were used in the experiments.

archwire was bound conventionally with ligature wire. The archwire was inserted passively because there were no crowding or rotations on plaster models. Two sets of identical dental mold models were prepared with brackets attached onto them, and NiTi archwires were attached to one model only. Dental molds both with and without archwires were subjected to static immersion for 31 days in separate containers, where the model without the archwires was utilized for obtaining a control fluid sample to detect the ion release only from the NiTi archwires via Inductively Coupled Plasma-Mass Spectroscopy (ICP-MS). The ingredients and the pH value of the AS employed in the current work are presented in Table 4.1. It should be noted that the pH of the natural saliva is about 7, however; a lower pH value (2.3) was preferred for AS in this study in order to incorporate the effects of acidic environment caused by possible dental plaque, and simulate the aggressive environment that would potentially stem from nutritional habits, and the corresponding organic depositions and intraoral microorganisms [10,12,26]. While preparing the AS, 1M of HCl was slowly added to the initial AS solution with pH value of near 7 until a level of acidity corresponding to a pH value of 2.3 was attained [23,24,26]. The prepared fluid was initially observed to be stable and remained the same throughout the experiments confirming the absence of salt deposition. Each model was immersed in a separate sealed beaker with 150 ml of prepared AS. The immersed samples were kept in an electronically controlled water bath sustaining the temperature at 37 °C, corresponding to the body temperature. Four sets of AS were used in the experiments: an as-prepared AS solution, AS with immersed undeformed wire in it, AS with only brackets attached to the mold, and AS with the wire attached onto the mold with brackets.

**Table 4.1.** Properties of the AS utilized in the current immersion experiments [1].

| Ingredients | Amount of Ingredients (g/l) | pH |
|---|---|---|
| **NaCl** | 0.4 | 2.3 |
| **KCl** | 0.4 | |
| **$CaCl_2 \cdot 2H_2O$** | 0.906 | |
| **$NaH_2PO_4 \cdot 2H_2O$** | 0.690 | |
| **$Na_2S \cdot 9H_2O$** | 0.005 | |
| **Urea** | 1 | |

Following an immersion period of 31 days, the immersed undeformed and bound archwires were comparatively investigated using scanning electron microscopy (SEM) and Energy dispersive X-ray spectroscopy (EDX) in order to detect SCC and the corresponding surface changes, as well as the C deposition on the bracket-archwire contact sites. The SEM and EDX analyses were conducted on a Zeiss Ultra Plus field emission scanning electron microscope and compared to a companion as-is archwire sample. The immersion fluids, on the other hand, were analyzed with a Perkin Elmer DRC II model ICP-MS in order to investigate the possible Ni or Ti ion release from the alloys into the fluids. The observable mass interval was 2-270 amu and the observation limit was in the ng/L level.

## 4.3 Results and Discussion

The surfaces of the as-is NiTi archwire and the undeformed and bound NiTi archwires immersed in artificial saliva for 31 days were investigated via SEM, EDX and optical microscopy following the immersion experiments and compared with the as-is archwire surface. The SEM images of the as-is, and immersed undeformed and bound archwires are presented in Figures 4.1-4.4. Figure 4.1 demonstrates that the as-is archwire features a relatively smooth surface, except for the processing marks and rare impurities, implying that

any foreign particle observed on the immersed archwire surfaces must be new structures that formed upon immersion in AS.

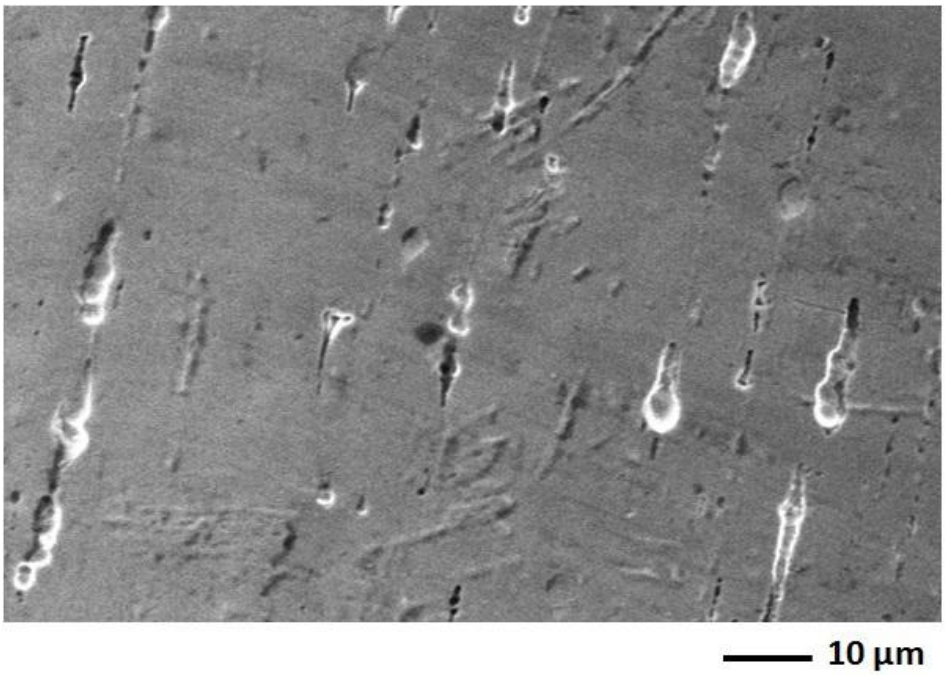


**Figure 4.1.** Representative SEM image of the as-is orthodontic archwire surface [1].

The SEM images of the immersed undeformed wire show rare dark spots which are randomly located on the wire surface (Figure 4.2). Quantitative EDX analysis from these regions indicated that these dark spots are mainly C containing structures (Table 4.2). Considering the high C content of AS and the previous experience on the C deposition on NiTi upon immersion in AS [10,12], it can be argued that the observed C-rich particle formation on the immersed undeformed NiTi archwires is reasonable. The random localization of these particles on the wire surface stems from the uniformity of the wire and the lack of distinctive and repetitive structures on the wire surface. Specifically, the only available sites for nucleation of new structures were the impurities, which were randomly distributed on the wire surface, leading to this observed random deposition of corrosion products.

**Table 4.2.** Relative quantities of the elements (provided in both wt.% and at.%) detected on the new structures present on the undeformed archwire immersed in AS for 31 days (Figure 2) [1].

| Element | wt.% | at.% |
|---|---|---|
| Carbon | 16.50 | 40.87 |
| Oxygen | 9.37 | 17.41 |
| Titanium | 36.25 | 22.52 |
| Nickel | 37.88 | 19.20 |
| | 100 | 100 |

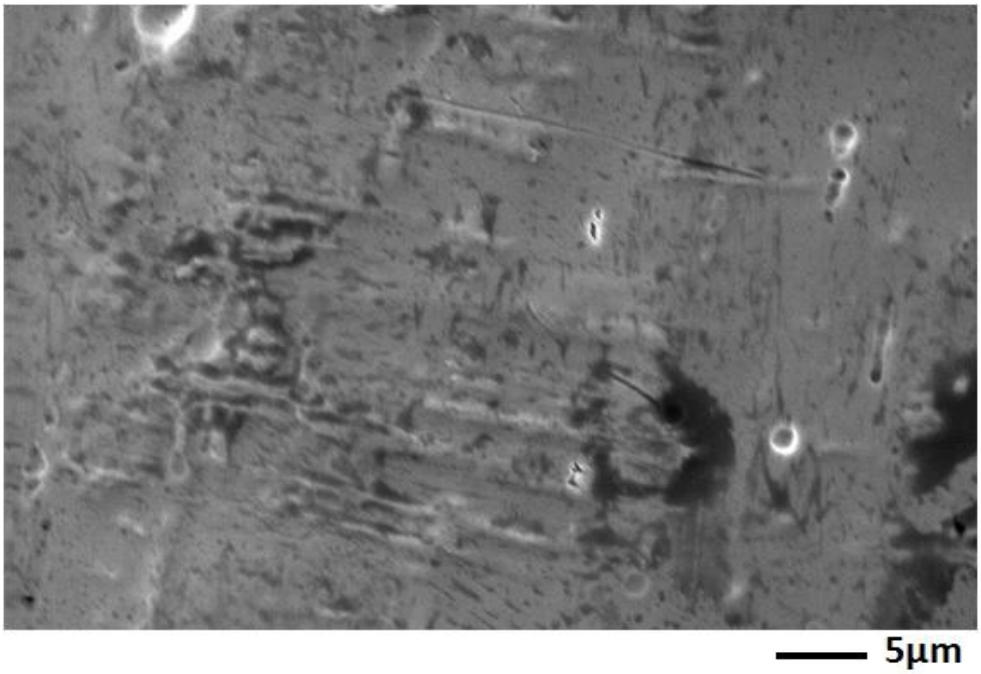


**Figure 4.2.** Representative SEM image of the undeformed orthodontic archwire surface immersed into AS [1].

The SEM examination of the immersed bound archwire also demonstrated presence of dark spots, which, however; were located with certain intervals on the surface rather than a random localization (Figure 4.3). Furthermore, each spot occupied a wider area (Figure 4.3) as compared to those observed on the immersed undeformed wire (Figure 4.2). The

quantitative EDX analysis indicated that these dark spots were also C-rich structures similar to those present on the undeformed immersed wire (Table 4.3). However, in addition to the dark structures, some white-colored salt-like precipitates were also observed on the immersed bound archwire (Figure 4.4). These salt-like precipitates were investigated via EDX in order to identify their chemical compositions, which demonstrated that they were Ca-rich particles (Table 4.4) stemming from the Ca release from the Ca-rich mold plasters. However, these Ca-rich particles also formed on certain locations, similar to the C-rich structures. Thus, in order to track the localization of all these corrosion products with certain intervals on the immersed bound archwire, the sample was also investigated with optical microscope, from which several images were gathered together for a more comprehensive picture of the overall wire surface (Figure 4.5).

**Table 4.3.** Relative quantities of the elements (provided in both wt.% and at.%) detected on the new structures present on the bound archwire immersed in AS for 31 days (Figure 3) [1].

| **Element** | **wt.%** | **at.%** |
|---|---|---|
| Carbon | 14.72 | 36.48 |
| Oxygen | 10.30 | 19.15 |
| Titanium | 33.35 | 20.73 |
| Nickel | 33.19 | 16.83 |
| Calcium | 5.94 | 4.41 |
| Phosphorus | 2.50 | 2.40 |
| Sum | 100 | 100 |

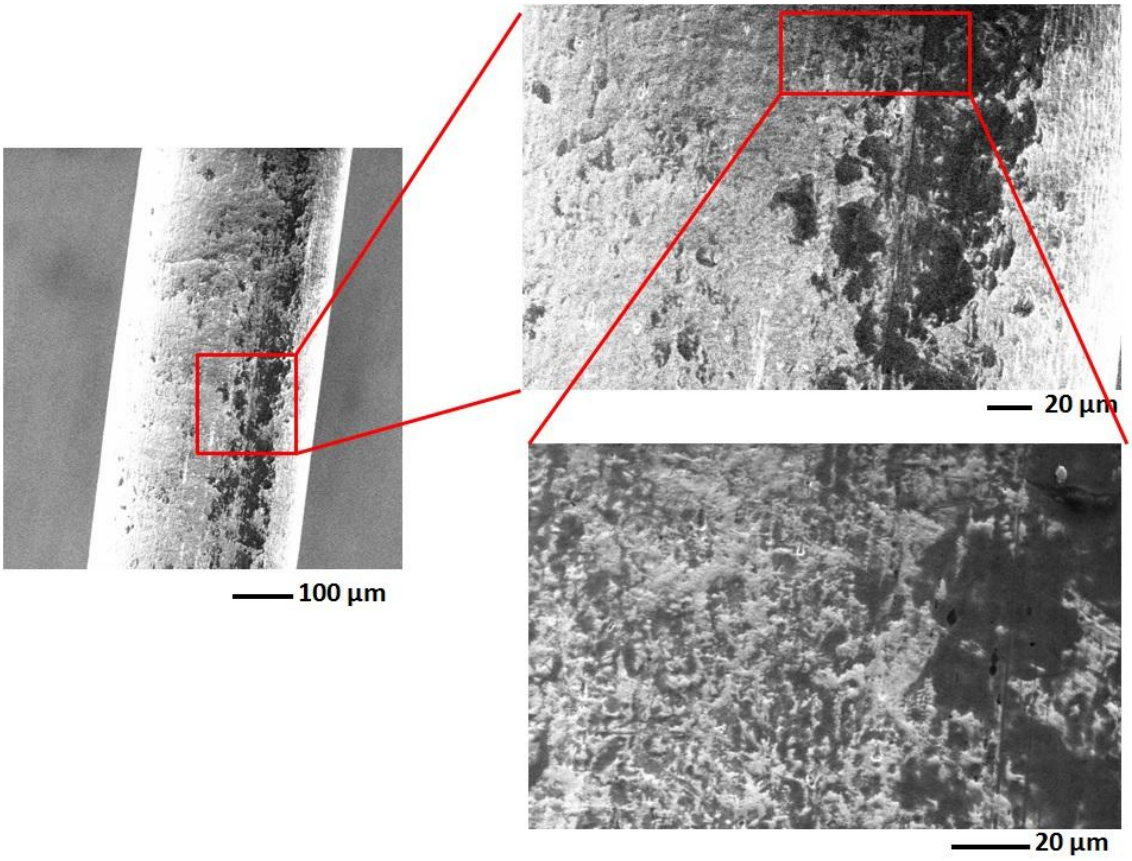


**Figure 4.3.** SEM images demonstrating C deposition on the bound orthodontic archwire immersed in AS [1].

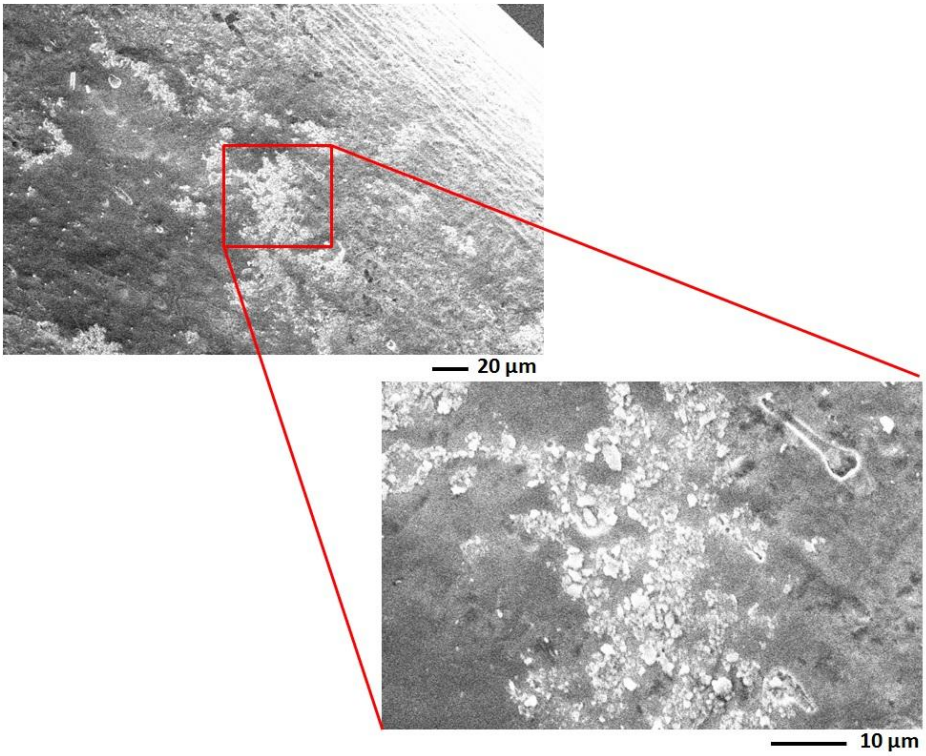


**Figure 4.4.** SEM images demonstrating Ca-rich phase deposition on the bound orthodontic archwire immersed in AS [1].

**Table 4.4.** Relative quantities of the elements (provided in both wt.% and at.%) detected on the salt like structures present on the bound archwire immersed in AS for 31 days (Figure 4) [1].

| Element | wt.% | at.% |
|---|---|---|
| Carbon | 4.59 | 11.15 |
| Oxygen | 26.92 | 49.14 |
| Nickel | 29.61 | 14.73 |
| Titanium | 28.27 | 17.25 |
| Calcium | 10.61 | 7.73 |
| Sum | 100 | 100 |

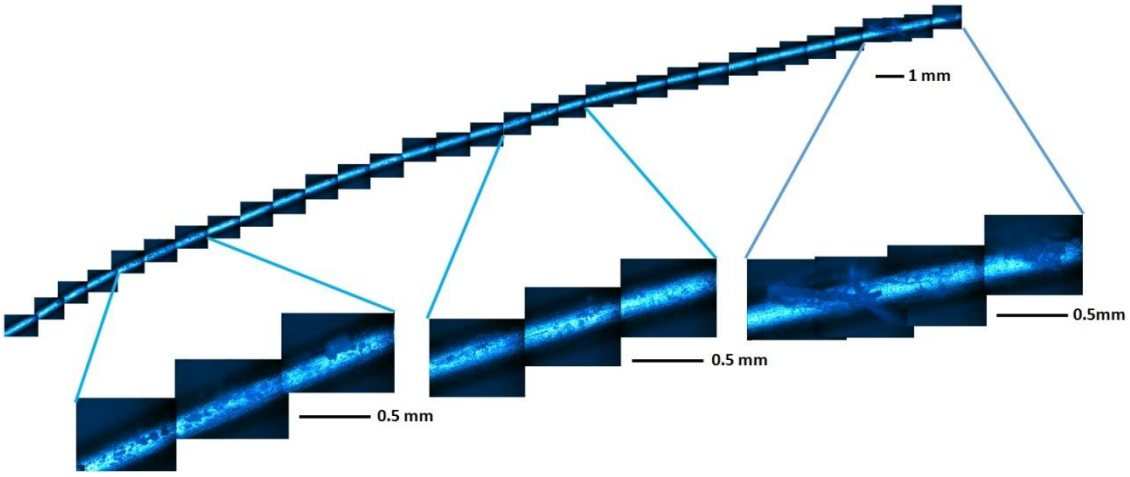


**Figure 4.5.** Optical microscope images of the bound orthodontic archwire immersed in AS Multiple high resolution images were gathered together to show the status of a meaningful segment of the wire upon being released from the mold.

The optical microscopy images clearly evidence the newly formed structures on the immersed bound archwire are located with almost equal intervals to each other (Figure 4.5). Moreover, measurement from the optical microscopy images demonstrates that the length of these intervals (about 1 cm) is close to the average distance between the brackets bonded to two consecutive teeth on the mold. This result justifies that the new particles are mainly deposited around the archwire-bracket contact zones. This localized precipitation of corrosion products is in good agreement with the findings of a similar study that compared an as-is archwire immersed in AS with a companion archwire that was retrieved from a patient after exposure to actual intraoral conditions for the same time interval [10]. Specifically, C-rich structure formation was observed on both wires, however; the depositions on the retrieved wires, which were localized at the archwire-bracket contact sites were dense enough to be visible to the naked eye. On the contrary, the deposition was random and observable only under SEM in the case of the immersed archwire [10]. This finding was attributed to the stress concentration induced by the contact of wire and brackets, which created more available sites for the nucleation of corrosion products [10]. Similar observations were also made in a work where in-service SCC based fracture of NiTi archwires were examined [6]. Specifically, the

microstructural and elemental analyses of the fracture surfaces showed that corrosion products composed of Na, K, Cl, P, S, and O precipitated in the vicinity of the crack tip, which constituted one of the highest stress concentration sites on the wire [6].

The preferential particle deposition at stress concentration zones have been subject to several studies, which evidenced that grain boundaries, impurities and other stress concentration points create ideal sites for nucleation of new phases, where the existing high energy facilitates precipitation of new structures by spending minimum energy [27,28]. Similarly, the current results showed that the C and Ca ions within the AS solution preferentially pile up on the wire-bracket contact sites in the form of C- and Ca-rich particles on the immersed bound archwire. Moreover, a closer look into these sites demonstrated that the stress induced by the contact of the wire with brackets causes formation of micro-cracks on the wire surface as a result of SCC (Figure 4.6(a)). Specifically, the wire surface becomes more prone to the stress created at the bracket contact sites due to the corrosive nature of AS, which enables crack initiation and propagation. Similar to the aforementioned stress concentration sites, cracks also constitute high energy regions, and thus, favor deposition of corrosion products in their close vicinity. Figure 4.6(b) evidences that the precipitates preferentially nucleate around the cracks on the immersed bound archwire. This argument is further strengthened by the random localization of corrosion products on the surface in the absence of micro-cracks in the case of the immersed undeformed archwire, which was not loaded during the immersion period. Therefore, formation and localization of new particles at certain locations with almost equal intervals, which correspond to the wire-bracket contact sites, can be explained with the stress concentration created at these contact sites due to SCC and the resulting micro-cracks. Yet, in contrast to the archwire that was exposed to actual intraoral conditions [10], the C-rich structures nucleated on the immersed bound archwire were not visible to naked eye. This difference can be attributed to the more complex

composition and variable constituents of actual intraoral environment, which involves not only the saliva but also the nutrients that are specific to the patient, implying that eating habits of the patient also significantly influence particle accumulation on the archwires in actual clinical conditions.

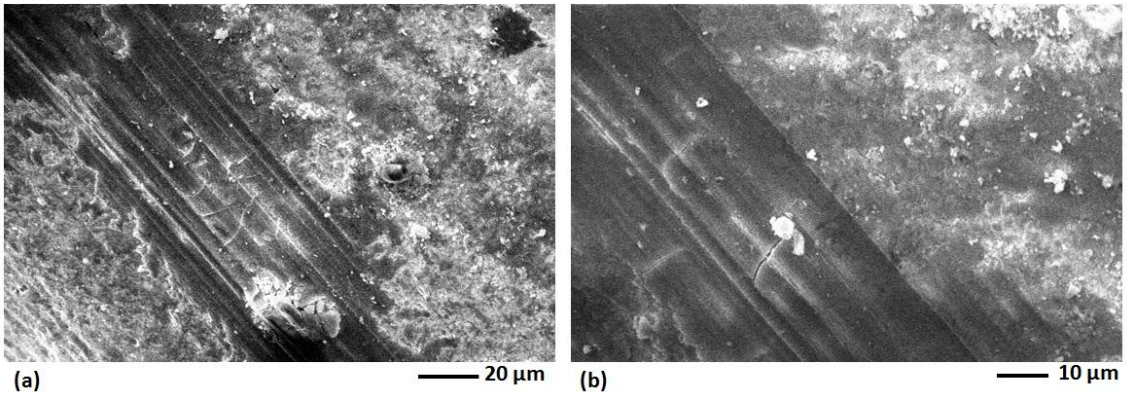


**Figure 4.6.** SEM images demonstrating **(a)** the crack formation due to SCC, and **(b)** the localization of the corrosion products near the cracks on the bound orthodontic archwire immersed in AS.

For the detection of potential Ni and Ti ion release from the archwires into the AS solutions and to investigate the effect of SCC on the ion release behavior of the archwires, all the AS solutions were subjected to ICP-MS following the experiments. Considering the Ca-rich precipitates observed on the immersed bound archwire, the solutions were also analyzed for possible Ca or P release from the mold. The Ni, Ti, Ca and P amounts measured in the four test solutions are presented in Table 4.5. Accordingly, the Ni and Ti contents in all four solutions were below the detection limits of 0.1 mg/L Ni and 0.005 mg/L Ti, respectively. The Ni release values were also below the critical limit of Ni intake (0.12-0.5mg/L) that can be harmful for the human body [25], indicating that the commercially available NiTi archwires can be considered safe for the patients within the immersion period considered in the current experiments. This finding also demonstrated that the archwire-bracket contact zones did not significantly enhance ion release despite being ideal sites for deposition of corrosion products. This can be attributed to the micron-size cracks promoted by SCC, which were not large

enough to lead to significant ion release, in addition to becoming blocked by the deposited corrosion products, further preventing ion release. As the new particle nucleation preferentially takes place at the contact regions and in the vicinity of cracks, the ion release from these zones was prevented by the particles deposited on the cracks. This finding is in good agreement with previously forwarded evidence for reduction in ion release due to oxide layer deposition on the stress-induced cracks [14].

**Table 4.5.** ICP-MS results demonstrating the Ni, Ti, Ca and P contents reselased into the AS solutions used in the experiments. The "–" indicates that measured ion concentration was below the detection limit [1].

| **AS solution** | Ni | Ti | Ca (mg/L) | P (mg/L) |
|---|---|---|---|---|
| as-preparesd AS | - | - | 247±4 | 164±2 |
| AS with undeformed wire | - | - | 253±3 | 167±4 |
| AS with brackets | - | - | 623±11 | - |
| AS with bonded wire | - | - | 658±10 | - |

In contrast to Ni and Ti, there was a significant amount of Ca in all four immersion fluids (Table 4.5). In addition, P was also present in AS solutions that did not contain molds, while no P was detected and the amount of Ca was significantly higher in AS solutions that contained molds, as compared to those in solutions without the molds. Considering that the molds are made of Ca-based plaster, the high amount of Ca detected in solutions that contained molds is reasonable. This also explains the Ca-rich precipitates on the immersed bound archwire, especially at the contact regions of archwire with the brackets. Moreover, the absence of P in solutions, in which undeformed and bound archwires were immersed, implies that the large amount of Ca released from the molds reacted with the P present in the solution

itself, and the detected Ca in these solutions are the excess Ca released from the molds. On the other hand, the presence of both Ca and P in solutions in the absence of the mold evidences that the detected Ca and P in these solutions belong to the ingredients of the solution itself (Table 4.1).

Overall, the current results indicate that the stress concentration stemming from the wire-bracket contact dictates both deposition of corrosion products on the surface and the ion release from orthodontic archwires. Moreover, the current set of experiments demonstrated that the actual intraoral conditions the orthodontic archwires become exposed to can be successfully simulated in terms of both physical and chemical conditions through static immersion experiments when wire-bracket contact is provided. Therefore, it can be concluded that *ex situ* experiments are critical and representative for biocompatibility testing of orthodontic archwires, as long as realistic mechanical and chemical conditions are provided, as accomplished in the current study.

## 4.4 Conclusions

The biocompatibility of commercial Nickel-Titanium (NiTi) orthodontic archwires was evaluated through *ex situ* experiments incorporating realistic chemical and mechanical conditions the archwires become subject to during actual intraoral stay. The results indicated that the archwire-bracket contact sites constitute critical regions for the deposition of corrosion products owing to elevated stress concentration, while these products prevented significant Ni or Ti ion release from the archwires. Moreover, the results of the experiments involving wire-bracket contact significantly differed from the experiments where mechanical contact was not provided, such that the former set of experiments successfully simulated the actual intraoral cavity in terms of formation and localization of corrosion products at the archwire-bracket contact sites. Overall, the current study demonstrates that the incorporation

of both chemical and mechanical conditions of the actual intraoral cavity is necessary for a reliable biocompatibility experiment.

The analyses presented in the last three chapters clearly demonstrated the significant influences of mechanical interactions, surface quality and microstructure on the biocompatibility of metallic biomaterials. For a better understanding of the microstructure-mechanical property relationship in metallic biomaterials, specifically texture and anisotropy, further experimental work focusing on the impact response of a potential biomedical alloy was undertaken. The corresponding analyses and results are presented in Chapter 5 of this thesis.

## 4.5 References


[1] S.M. Toker, B. Gumus, D. Sahbazoglu, B. Uzer, D. Saher, D. Canadinc, Mater. Sci. Eng. C Submitted (2014).

[2] R.J. Nikolai, Orthodontic wire: a continuing evolution., Semin. Orthod. 3 (1997) 157–165.

[3] T. Duerig, A. Pelton, D. Sto, An overview of nitinol medical applications, 275 (1999) 149–160.

[4] G. Mani, M.D. Feldman, D. Patel, C.M. Agrawal, Coronary stents: a materials perspective., Biomaterials. 28 (2007) 1689–1710.

[5] A. Bansiddhi, T.D. Sargeant, S.I. Stupp, D.C. Dunand, Porous NiTi for bone implants: a review., Acta Biomater. 4 (2008) 773–782.

[6] J. Wang, N. Li, G. Rao, E.-H. Han, W. Ke, Stress corrosion cracking of NiTi in artificial saliva., Dent. Mater. 23 (2007) 133–137.

[7] Z. Davidovitch, V. Krishnan, Role of basic biological sciences in clinical orthodontics: a case series., Am. J. Orthod. Dentofacial Orthop. 135 (2009) 222–231.

[8] H. Wehrbein, P. Göllner, Skeletal anchorage in orthodontics--basics and clinical application., J. Orofac. Orthop. 68 (2007) 443–461.

[9] A. Van Schepdael, J. Vander Sloten, L. Geris, Mechanobiological modeling can explain orthodontic tooth movement: three case studies., J. Biomech. 46 (2013) 470–477.

[10] S.M. Toker, D. Canadinc, Evaluation of Biocompatibility of NiTi Dental Wires: A Comparison of Laboratory Experiments and Clinical Conditions, Mater. Sci. Eng. C. 40 (2014) 142–147.

[11] S. Miyazaki, K. Otsuka, Development of shape memory alloys., ISIJ Int. 29 (1989) 353–377.

[12] S.M. Toker, D. Canadinc, H.J. Maier, O. Birer, Evaluation of passive oxide layer formation-biocompatibility relationship in NiTi shape memory alloys: Geometry and body location dependency., Mater. Sci. Eng. C. Mater. Biol. Appl. 36 (2014) 118–129.

[13] K. House, F. Sernetz, D. Dymock, J.R. Sandy, A.J. Ireland, Corrosion of orthodontic appliances--should we care?, Am. J. Orthod. Dentofacial Orthop. 133 (2008) 584–592.

[14] J.-K. Liu, T.-M. Lee, I.-H. Liu, Effect of loading force on the dissolution behavior and surface properties of nickel-titanium orthodontic archwires in artificial saliva., Am. J. Orthod. Dentofacial Orthop. 140 (2011) 166–176.

[15] O. Prymak, A. Klocke, B. Kahl-Nieke, M. Epple, Fatigue of orthodontic nickel–titanium (NiTi) wires in different fluids under constant mechanical stress, Mater. Sci. Eng. A. 378 (2004) 110–114.

[16] A. Milheiro, C. Kleverlaan, J. Muris, A. Feilzer, P. Pallav, Nickel release from orthodontic retention wires-the action of mechanical loading and pH., Dent. Mater. 28 (2012) 548–553.

[17] E.M. Al-Waheidi, Allergic reaction to nickel orthodontic wires: a case report., Quintessence Int. 26 (1995) 385–387.

[18] M.R. Grimsdottir, A. Hensten-Petterseri, Surface analysis of nickel-titanium archwire used in vivo, Dent. Mater. 13 (1997) 163–167.

[19] H.-H. Huang, Variation in surface topography of different NiTi orthodontic archwires in various commercial fluoride-containing environments., Dent. Mater. 23 (2007) 24–33.

[20] D.K. Pun, D.W. Berzins, Corrosion behavior of shape memory, superelastic, and nonsuperelastic nickel-titanium-based orthodontic wires at various temperatures., Dent. Mater. 24 (2008) 221–227.

[21] C. Heßing, J. Frenzel, M. Pohl, S. Shabalovskaya, Effect of martensitic transformation on the performance of coated NiTi surfaces, Mater. Sci. Eng. A. 486 (2008) 461–469.

[22] O. Mockers, D. Deroze, J. Camps, Cytotoxicity of orthodontic bands, brackets and archwires in vitro., Dent. Mater. 18 (2002) 311–317.

[23] T.-H. Lee, C.-C. Wang, T.-K. Huang, L.-K. Chen, M.-Y. Chou, H.-H. Huang, Corrosion resistance of titanium-containing dental orthodontic wires in fluoride-containing artificial saliva, J. Alloys Compd. 488 (2009) 482–489.

[24] X. Li, J. Wang, E. Han, W. Ke, Influence of fluoride and chloride on corrosion behavior of NiTi orthodontic wires., Acta Biomater. 3 (2007) 807–815.

[25] H.-H. Huang, Y.-H. Chiu, T.-H. Lee, S.-C. Wu, H.-W. Yang, K.-H. Su, et al., Ion release from NiTi orthodontic wires in artificial saliva with various acidities, Biomaterials. 24 (2003) 3585–3592.

[26] R.R. Al-Hity, H.F. Kappert, S. Viennot, F. Dalard, B. Grosgogeat, Corrosion resistance measurements of dental alloys, are they correlated?, Dent. Mater. 23 (2007) 679–687.

[27] R. Huang, Y. Han, The effect of SMAT-induced grain refinement and dislocations on the corrosion behavior of Ti-25Nb-3Mo-3Zr-2Sn alloy., Mater. Sci. Eng. C. Mater. Biol. Appl. 33 (2013) 2353–2359.

[28] Y. Estrin, E.P. Ivanova, A. Michalska, V.K. Truong, R. Lapovok, R. Boyd, Accelerated stem cell attachment to ultrafine grained titanium., Acta Biomater. 7 (2011) 900–906.

# 5 CHAPTER 5: ANISOTROPY OF ULTRAFINE-GRAINED ALLOYS UNDER IMPACT LOADING - THE CASE OF BIOMEDICAL NIOBIUM ZIRCONIUM [1]

## 5.1 Introduction

NbZr alloys, whose main constituents Nb and Zr were separately reported to be biocompatible, have recently come under focus in the biomedical field, as they also exhibit superior corrosion resistance and biocompatibility [2-5]. In addition, it has been demonstrated that an optimum combination of mechanical properties, high strength and good fatigue resistance, can be obtained when an UFG microstructure is induced [3-7]. This good combination of biocompatibility and mechanical properties promote the use of UFG NbZr alloys as implant material especially in orthopedic and dental treatments. Such applications demand not only corrosion resistance; but also high strength, improved fatigue resistance and fracture toughness, as the envisaged implants are supposed to function under various loading scenarios [8-11], warranting a thorough program of diverse mechanical experiments prior to their utility. It is known that impact loads prompted by falling or jumping may cause serious injuries and bone fractures in various body parts, such as hip or knee joints [12-16], emphasizing the need for impact testing within such an experimental program. However, to the best of the authors' knowledge, no studies focusing on the impact response of UFG NbZr have been reported yet.

The overall fracture behavior of a material is dictated by both the impact strength and the ductile-to-brittle transition temperature (DBTT) [17], where the decrease of the latter has been associated with grain refinement, delaminations and precipitates [18, 19]. Specifically, both grain boundaries and delaminations may act as obstacles against crack propagation depending on the orientation of the crack, increasing the necessary energy barrier. The

increased misorientation between the neighboring grains in UFG materials might be considered to act in a similar manner, as high-angle grain boundaries (HAGBs) constitute effective barriers against dislocation motion, increasing cyclic stability [20 - 22]. Hence, they are expected to hinder or slow down crack propagation. Accordingly, reduced grain size, which results in an increased number of grain boundaries, the majority of which are HAGBs in efficiently processed UFG materials, leads to improved fracture toughness and lower DBTT values as compared to microstructures dominated by low-angle grain boundaries [18 - 22]. These observations evidence that the UFG microstructure plays a major role in the improvement of fracture toughness of a material, and warrant a detailed investigation of the impact response for a complete understanding of the overall mechanical behavior.

Consideration of misorientation of neighboring grains brings anisotropy into discussion, one of the major parameters dictating the overall deformation response. For implants that are designed to replace the living bone tissue, anisotropy attains even higher priority as the bone itself possesses a high degree of anisotropy [23, 24]. Thus, in order to mimic bone tissue as closely as possible and thereby ensure a similar mechanical behavior as that of the bone under the expected loading conditions, an implant material with a similar anisotropy should be preferred. Since impact constitutes one of the most critical loading scenarios for orthopedic implants [12-16], its relationship to anisotropy could serve as an important parameter in implant design.

The current study was undertaken with the motivation of establishing the anisotropy – impact response relationship for UFG NbZr alloys, a promising class of biomedical alloys. In particular, two different NbZr microstructures, one coarse-grained (CG) and one UFG variant, were investigated in terms of their impact response and DBTT values. The UFG variant included four different sub-variants, each extracted from the same severe-plastically deformed NbZr billet with different orientations with respect to extrusion direction (ED), in order to

establish the effects of texture and anisotropy. The current findings constitute the very first results on impact response of UFG NbZr alloys and reveal the strong anisotropy-dependent impact behavior of the UFG microstructure.

## 5.2 Experimental Procedure

The material tested in this study was a NbZr alloy with a chemical composition of 2.33 wt.% Zr, 0.29 wt.% Ta, 76 ppm $H_2$, 44 ppm $O_2$, 63 ppm C, 5 ppm Fe and balance Nb. The NbZr alloy was originally obtained in form of a 30 mm thick hot-rolled plate with a CG microstructure, and then processed by equal-channel angular extrusion (ECAE) along route $8E^3$ to achieve an UFG microstructure [5- 7]. Impact samples were extracted from both CG and UFG alloys with dimensions of 2.8 mm × 25 mm × 4 mm, featuring a 60˚ notch with a radius of 0.1 mm and a depth of 1 mm [27]. While the CG samples were extracted only along the rolling direction, the UFG variants were extracted along three different orientations with respect to the ED: 0˚ (UFG/0˚), 26˚ (UFG/26˚ and UFG/26°×90°) and 90˚ (UFG/90˚), as depicted in the inset of Figure 5.1. The 26° variants were chosen since this specific inclination corresponds to the direction of material flow during ECAE processing. The impact experiments were conducted at five different temperatures: 50 ˚C, 0 ˚C, -50 ˚C, -100 ˚C and -150 ˚C. The specimens were tested with an impact energy of 50 J and at a velocity of 3.8 m/s, where 8000 data points were collected during each experiment with a data acquisition frequency of 2 MHz.

[3] Detailed information about the ECAE procedure can be found in [25, 26].

## 5.3 Results and Discussion

The impact toughness and DBTT values of the CG and UFG NbZr samples are shown in Figure 5.1. The CG sample undergoes a ductile-to-brittle transition as the temperature decreases from 50˚C to -100˚C, and exhibits a typical impact behavior, while significant variations are evident in the impact behavior of the UFG variants. Specifically, impact energies of all the UFG variants are higher as compared to that of the CG sample at lower temperatures. As the temperature increases the situation is reversed, such that the impact energy of the CG sample is higher as compared to the UFG variants. However, when the overall impact responses are examined, a smoother transition pattern is exhibited by the UFG variants, indicating a less temperature sensitive impact behavior and a more stable response, except for the UFG/0˚ and UFG/26°×90° with impact energies that show inverse dependence on temperature.

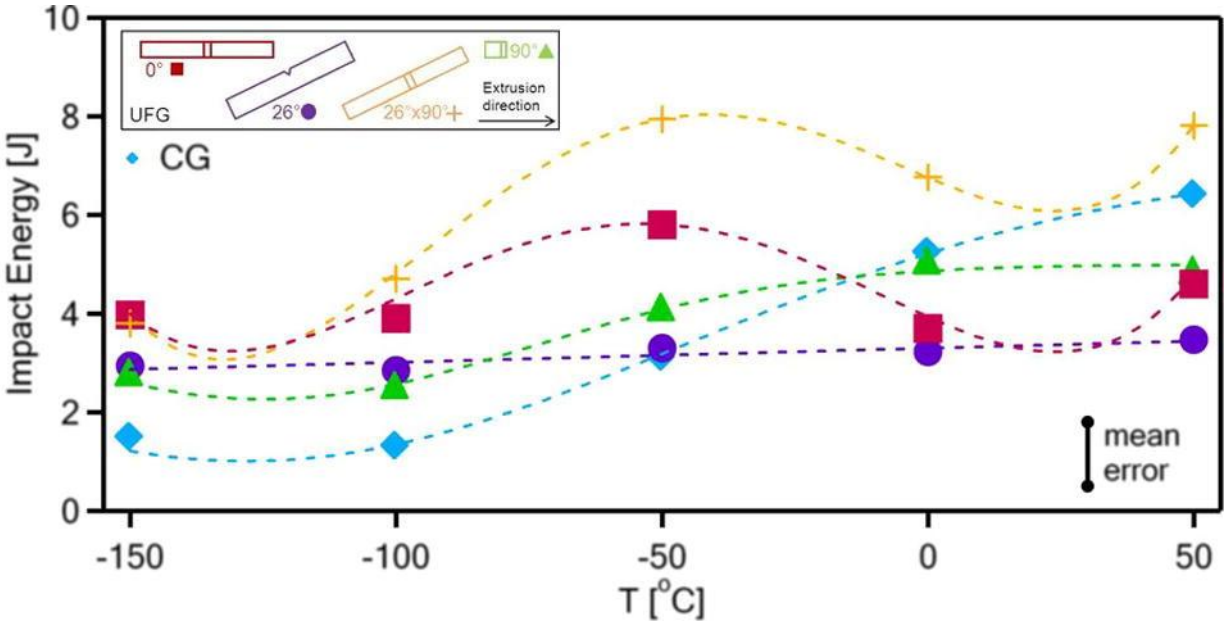


**Figure 5.1.** Impact energy – temperature trends for the five NbZr variants. Each result represents an average of two companion experiments. The inset depicts the UFG specimen orientations with respect to the ECAE flow plane and the extrusion direction [1].

A noteworthy observation is that UFG/26˚ exhibits a very smooth transition in the ductile-to-brittle region with no clear DBTT, and smaller impact energy as compared to UFG/90˚ at all temperatures above -100 °C. This may be attributed to the strong yet brittle behavior of the UFG/26˚ variant, which is also evident from a comparison of fracture zones, where the fracture surface of the UFG/26˚ exhibits less traces of plastic deformation as compared to that of UFG/90˚ (Figure 5.2). In particular, a higher density of cleavage planes is prevalent in UFG/26˚ (Figure 5.3), yielding the observed brittle fracture and a smooth fracture surface. These cleavage planes provide a path for cracks, along which propagation occurs easier (Figure 5.4), resulting in larger cracks and rapid fracture with less energy absorption.

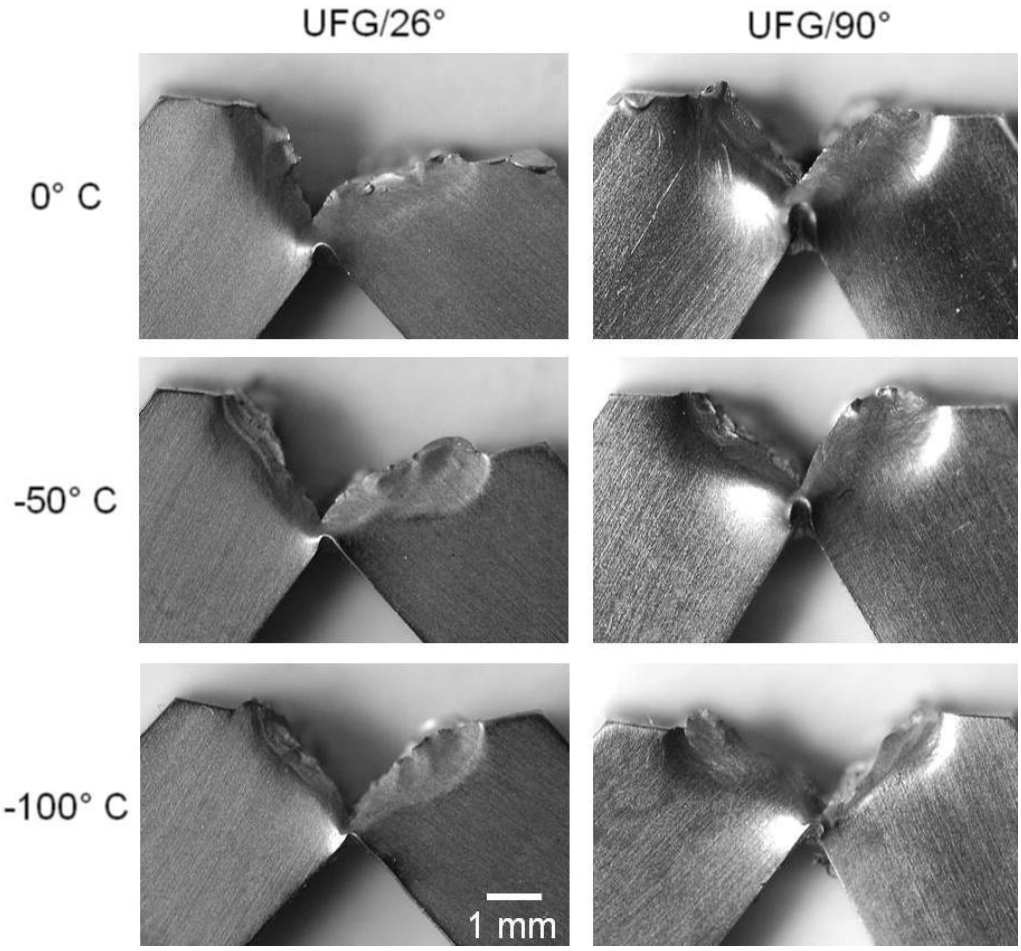


**Figure 5.2.** Fractured UFG/26˚ and UFG/90˚ samples following the impact experiments at 0˚, -50˚ and -100˚C [1].

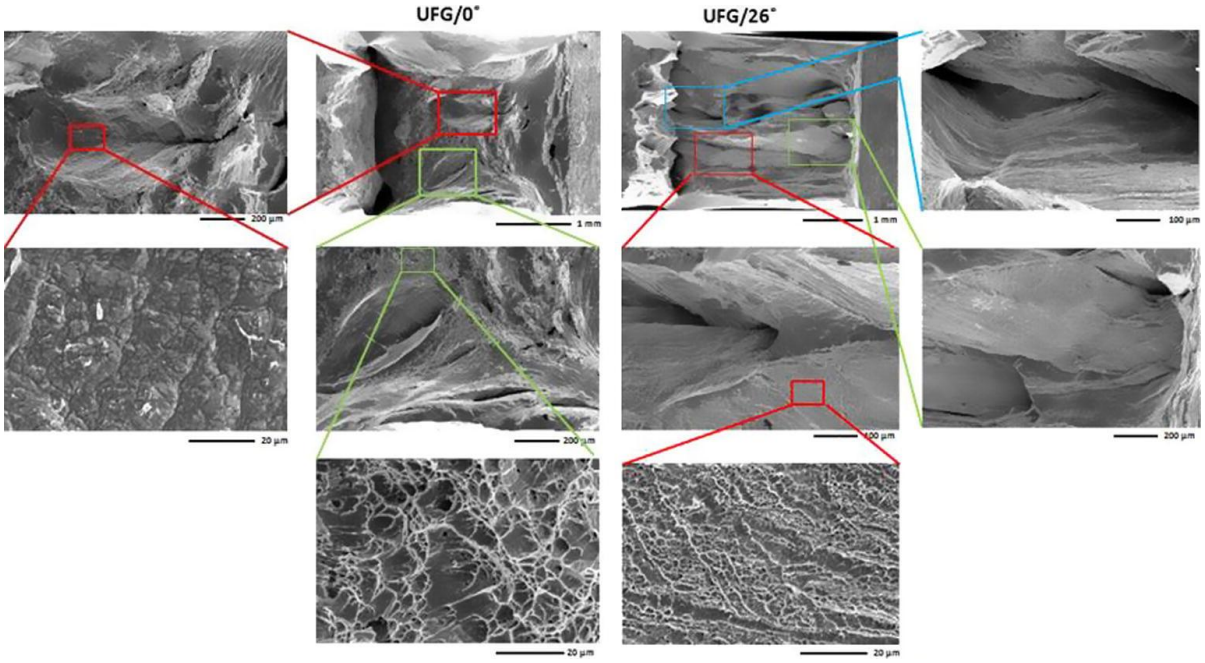


**Figure 5.3.** SEM images of UFG/0˚ and UFG/26˚ fracture surfaces. Examples of delaminations in UFG/0˚ and cleavage planes in UFG/26˚ are demonstrated within the color-framed boxes and in the associated images with higher magnifications [1].

In the case of UFG/90˚, the transition from the ductile-to-brittle region is more obvious, and higher energy absorption is noted (Figure 5.1), implying that this UFG variant is more susceptible to temperature changes and exhibits ductile failure. Specifically, larger plastic strains are attained prior to failure, further promoting slip activity as compared to UFG/26˚, and thus, a more distorted fracture surface is present upon impact loading (Figure 5.2). Furthermore, the elongated grains imposed by severe plastic deformation are aligned with the initial crack growth direction, and the cracks propagate along the grain boundaries (Figure 5.4). It was previously shown that crack propagation is dictated by both the loading direction and elongated grain structures brought about by ECAE processing [28]. Specifically, the stress concentration zones stemming from elongated grains force the crack to deviate from its original path and propagate along grain boundaries. Similarly, for the current material, it is anticipated that the resulting rupture is accompanied by enhanced slip activity within the grains as the crack advances, where the dislocations interacting with the grain boundaries

indeed place them under pressure, delaying the local fracture and allowing for more energy absorption and plastic deformation prior to failure, as compared to UFG/26˚.

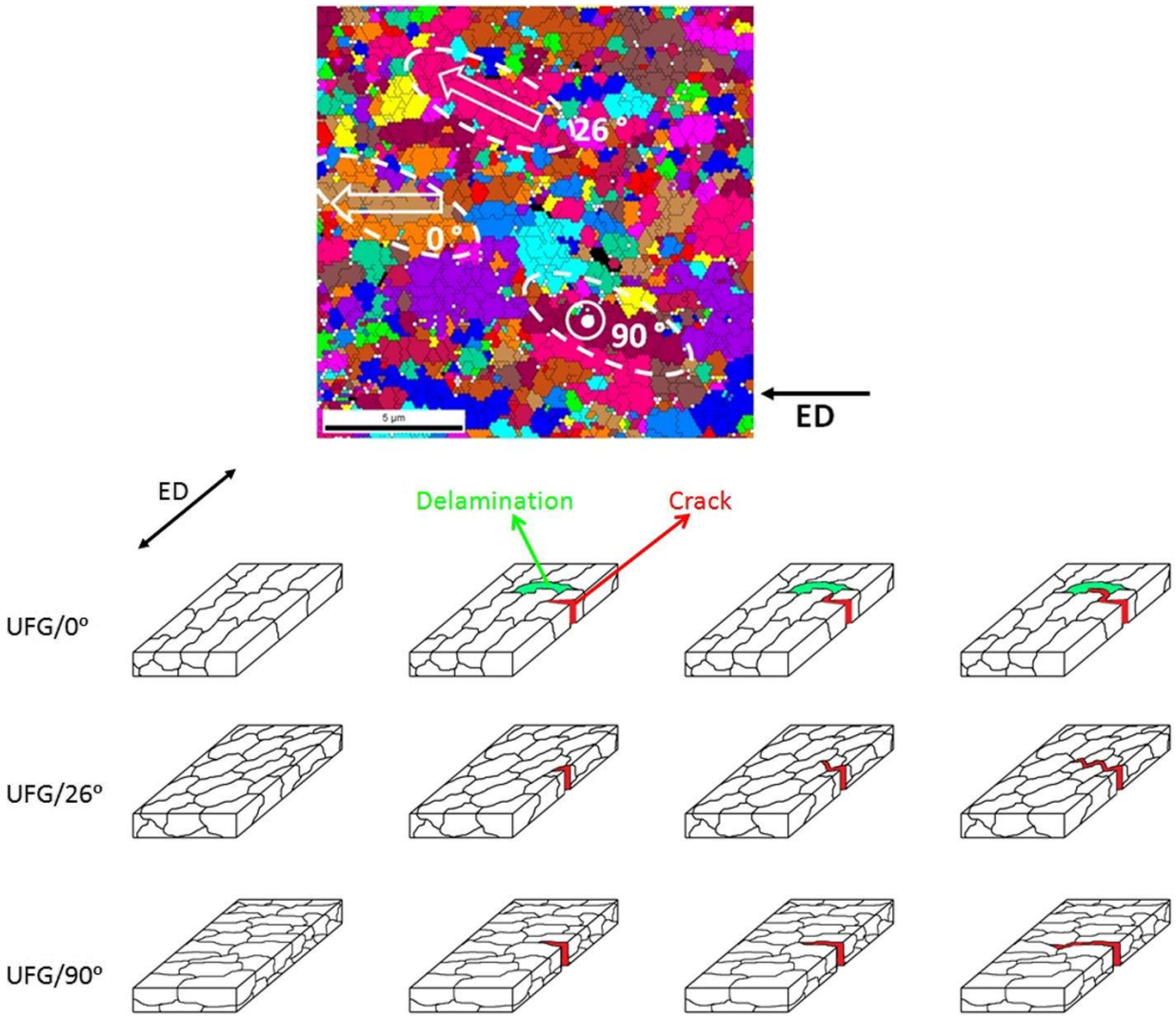


**Figure 5.4.** Schematic detailing the influence of delaminations and cleavage planes on the crack propagation in UFG NbZr. The EBSD grain map shows the relative orientations of the UFG subvariants with respect to the ED [1].

Influence of anisotropy becomes even more evident in the cases of UFG/0˚ and UFG/26°×90°, which behave significantly different as compared to the other UFG variants and the CG sample (Figure 5.1). In particular, the impact energy of UFG/0˚ increases concomitant with temperature up to about -50 ˚C where it reaches a maximum, and decreases sharply afterwards. While the CG and UFG/90˚ samples exhibit a clear distinction between ductile and brittle regions and UFG/26˚ exhibits a completely brittle response, one can argue

that UFG/0˚ acts in a ductile manner, since even the lowest impact energy value observed for UFG/0˚ is higher than those of the other samples in the brittle region (Figure 5.1). Here, the elongated grain boundaries laying perpendicular to the crack path constitute a barrier against crack propagation, and thus, delay failure (Figure 5.4). Specifically, as a propagating crack comes across a grain boundary laying perpendicular to its path, the large grain boundary misorientation angle energetically favors the crack's advance along (rather than through) the grain boundary. This leads to higher energy absorption up to failure, and higher impact energy values are recorded for this sample as compared to other variants.

Similar to grain boundaries, delaminations can also impede crack propagation and result in higher impact energies [18, 19, 28]. Delaminations may stem from anisotropic microstructures, where, for instance, grains are predominantly oriented along the ED [19]. In the current study, the UFG/0˚ variant features a microstructure with grains mostly oriented along the primary shear plane, and more delaminations are prevalent upon impact as compared to other variants, as evident from the fracture surfaces (Figure 5.3). Specifically, as a crack initiates and starts to advance under impact loading, it is eventually diverted by a grain boundary with a large misorientation angle. As it advances along the grain boundary afterwards, the chances that it comes across a delamination increases (Figure 5.4). Rather than cutting through the delamination, the crack diverts again to advance along the delaminated line. Overall, this continuous diversion of the crack delays the failure and enhances the energy absorption prior to failure.

The UFG/0˚ and UFG/26°×90° variants are distinguished from the other samples also by their inverse temperature dependence of impact energy at temperatures around -50 ˚C (Figure 5.1). A similar behavior has previously been reported in an UFG ultrahigh-strength low-alloy steel featuring elongated ferritic grains [19]. The unusual inverse temperature dependence of this material was explained by the dominance of delaminations over cleavage

planes at lower temperatures [19]. Normally, at high temperatures, slip activity increases with enhanced energy, and constitutes the major mechanism leading to failure. However, at low temperatures, the high activation energy values restrict dislocation motion, resulting in a limited amount of plastic deformation and very low energy absorption, and thus, promote brittle failure. This type of brittle fracture in metals usually takes place along specific crystallographic planes called cleavage planes, on which continuous breaking of atomic bonds takes place easily. However, if delaminations are also present in the microstructure as in the cases of UFG/0˚ and UFG/26°×90°, they dominate the system over cleavage planes, such that; while atomic bonds break on the cleavage planes and lead to fracture, delaminations impede crack growth and delay fracture (Figure 5.4). If their density is large enough, delaminations can suppress the effect of cleavage planes, facilitating larger plastic deformation prior to failure and higher energy absorption. As a result, instead of the expected brittle behavior, a ductile behavior with higher energy absorption can be seen at low temperatures (Figure 5.1).

## 5.4 Conclusion

Overall, the current findings demonstrate the significant influence of anisotropy on the impact response of UFG NbZr, a promising candidate implant material for orthopedic and dental treatments. The results are encouraging, such that UFG NbZr implants can be designed to meet the required failure criteria by adjusting the anisotropy of the material prior to replacing the original bone tissue.

For a more detailed understanding of the role of microstructural interactions on the impact response of metals to be utilized in the design of implant materials, the knowledge gained in this part of the thesis work was extended to the study focusing on the impact response of a structural metallic material, which involves a complex microstructure with

intensive slip-twin interactions. The corresponding analyses are presented in the following chapter.

## 5.5 References


[1] S.M. Toker, F. Rubitschek, T. Niendorf, D. Canadinc, H.J. Maier, Scripta Mater. 66 (2012) 435-438.

[2] N.J. Hallab, S. Anderson, M. Caicedo, J.J. Jacobs, J. ASTM Int. 3 (2006) 248-259.

[3] H. Matsuno, A. Yokoyama, F. Watari, M. Uo, T. Kawasaki, Biomaterials 22 (2001) 1253-1262.

[4] H.G. Kim, S.Y. Park, M.H. Lee, Y.H. Jeong, S.D. Kim, J. Nucl. Mater. 373 (2008) 429-432.

[5] F. Rubitschek, T. Niendorf, I. Karaman, H.J. Maier, J. Mech. Behav. Biomed. Mater. 5 (2011) 181-192.

[6] T. Niendorf, D. Canadinc, H.J. Maier, I. Karaman, G.G. Yapici, Acta Mater. 55 (2007) 6596-6605.

[7] T. Niendorf, H.J. Maier, D. Canadinc, G.G. Yapici, I. Karaman, Scripta Mater. 58 (2008) 571-574.

[8] M. Cehreli, S. Sahin, K. Akca, J. Dent. 32 (2004) 123-132.

[9] C. Anunmanaa, K. J. Anusavicea, J. J. Mecholsky Jr., Dent. Mater. 26 (2010) 111-117.

[10] H.S. Gupta, P. Zioupos, Med. Eng. Phys. 30 (2008) 1209-1226.

[11] M. Moazen, A.C. Jones, Z. Jin, R. K. Wilcox, E. Tsiridis, Clin. Biomech. 26 (2011) 13-22.

[12] P. Kannus, J. Parkkar, J. Poutala, Bone 25 (1999) 229-235.

[13] Y. Fukuda, S. Takai, N. Yoshino, K. Murase, S. Tsutsumi, K. Ikeuchi, Y.Hirasawa, Clin. Biomech. 15 (2000) 516-521.

[14] A. Verteramo, B.B. Seedhom, J. Biomec. 40 (2007) 3580-3589.

[15] N. Wakaoa, A. Harada, Y. Matsui, M. Takemura, H. Shimokata, M. Mizuno, M. Itod, Y. Matsuyamaa, N. Ishiguro, Med. Eng. Phys. 31 (2009) 1134-1139.

[16] T.P. Pinilla, K.C. Boardman, M.L. Bouxsein, Myers, W.C. Hayes, Calcif. Tissue Int. 58 (1996) 231-235.

[17] J. W. Morris, Jr., Science 320 (2008) 1022-1023.

[18] R. Song, D. Ponge, D. Raabe, Acta Mater. 53 (2005) 48814892

[19] Y. Kimura, T. Inoue, F. Yin, K. Tsuzaki, Science, 320 (2008) 1057-1059.

[20] P. Gabor, D. Canadinc, H.J. Maier, R.J. Hellmig, Z. Zuverova, J. Estrin, Met. Mat. Trans. A 38A (2007) 1916-1925.

[21] D. Canadinc, H.J. Maier, M. Haouaoui, I. Karaman, Scripta Mater. 58 (2008) 307-310.

[22] T. Niendorf, D. Canadinc, H.J. Maier, I. Karaman, S.G. Sutter, Int. J. Mat. Res. 97 (2006) 1328-1336.

[23] B.B. Martin, D.B. Burr, N.A. Sharkey Skeletal Tissue Mechanics, Springer, Verlag, NY, 1998.

[24] J.Y. Rho, L. Kuhn-Spearing, P. Zioupos, Med. Eng. Phys. 20 (1998) 92-102.

[25] R.E. Barber, T. Dudo, P.B. Yasskin, K.T. Hartwig, Scripta Mater.51 (2004) 373-377.

[26] V.M. Segal, R.E. Goforth, K.T. Hartwig, Texas A&M University US Patent No. 5,400,633; 1995.

[27] ISO 14556:2000 + Amd.1:2006, Steel – Charpy V-notch pendulum impact test – Instrumented test method

[28] T. Niendorf, F. Rubitschek, H.J. Maier, D. Canadinc, I. Karaman, J Mater Sci 45 (2010) 4813-4821.

# 6 CHAPTER 5: ON THE ROLE OF SLIP - TWIN INTERACTIONS ON THE IMPACT BEHAVIOR OF HIGH-MANGANESE AUSTENITIC STEELS [1]

## 6.1 Introduction

Austenitic high-manganese steels, a class of high strength steels, have received considerable attention owing to their exceptional work hardening capacity, high wear and abrasion resistance, and the rare combination of high strength and significant ductility they offer [2-4]. The extraordinary mechanical properties of this class of steels have been subject to several studies [4-10], many of which revealed that the main mechanism underlying the observed mechanical behavior is the presence of twins in the microstructure accompanied by additional deformation mechanisms, such as stacking faults, dynamic strain aging (DSA) and interaction of twins with dislocations [7-10]. All of the aforementioned mechanisms contribute to the improved strength and work hardening capacity of this class of steels by mainly providing obstacles against dislocation motion [7-10]. However, the complexity of the deformation behavior of these materials makes it difficult to clearly distinguish between the relative contributions of the hardening mechanisms.

This is especially true for twinning since twins can interact with dislocations in different ways, which also depends on the dislocation density [5-13]. Twin activity usually starts at the early stages of plastic deformation, which is followed by an increase in twin density and interaction with dislocations. In the presence of a large density of dislocations, further dislocation interaction can facilitate the nucleation of new twins by raising the local stresses in the vicinity of existing dislocations to beyond the critical twinning shear stress level [6, 8, 14]. These newly nucleated twins can form a ladder-like structure, further hindering dislocation activity, which contribute to the overall strain hardening of the material [6, 14]. However, when dislocation density is not large enough to provide the necessary stress for the

nucleation of new twins, dislocations hinder the nucleation of new twins, and instead, favor the growth of the existing ones, yielding thicker twins [6, 14]. This leads to fewer twin boundaries or, in other words, fewer obstacles against dislocation motion, and consequently less interaction between twins and dislocations. Since dislocation density is also smaller in this case, the relatively lower number of dislocations would glide easier in the material, interacting less with obstacles, which is expected to yield lower strain hardening rates, and eventually softening of the material [6, 14].

Another factor that affects the density and thickness of twins is the stacking fault energy (SFE) [3, 4, 8, 15]. The relation between stacking faults and twins becomes especially significant when deformation takes place at different temperatures: at elevated temperatures, SFE increases and prevents partition of dislocations, promoting glide of perfect dislocations instead, which favors slip activity over twining [3, 4]. Thus, twin density is expected to decrease at elevated temperatures while a large twin density is anticipated at lower temperatures [3, 4].

These observations have been made for various loading scenarios, such as monotonic tensile and compressive loading, or cyclic loading. However, there are very few studies exploring the impact response of austenitic high-manganese steels [16-18], and to the best of the authors' knowledge, no findings on the microstructure evolution upon impact in this class of steels have been forwarded so far. The current study was undertaken with the motivation of addressing this issue, and the impact response of an austenitic high-manganese steel containing 12.4 wt. % manganese was systematically investigated for several different temperatures. An additional motivation of the current work was to shed light onto the complicated interaction of micro deformation mechanisms which leads to the strain hardening mechanism observed in high-manganese austenitic steels by utilizing a different mode of loading than those considered in previous investigations, namely the impact loading. For this

purpose, the relative activities of slip and twinning, and their interactions, were monitored by scanning electron microscopy (SEM) and transmission electron microscopy (TEM) following the experiments.

## 6.2 Experimental Procedure

The material tested in this study was an austenitic high-manganese steel with a chemical content of 12.4 wt. % manganese and 1.1 wt. % carbon. The impact samples with dimensions of 2.8 mm × 25 mm × 4 mm featured a 60° notch with a radius of 0.1 mm and a depth of 1 mm. The samples were extracted from the bulk via electro-discharge machining in order to minimize residual stresses. In order to establish the temperature dependence of the impact response, and thereby determine the ductile-to-brittle transition temperature (DBTT) of the material and promote different relative activities of slip and twinning [19], impact experiments were conducted at seven different temperatures: 200, 150, 100, 50, 0, -50 and -100 °C (Figure 6.1). Three samples were tested at each temperature to check repeatability. The specimens were subjected to an impact energy of 50 J at a velocity of 3.8 m/s. During each experiment, 8000 data points were collected with a data acquisition frequency of 2 MHz. The strain gages on the hammer peen enabled the detection of instantaneous forces. The displacement sensor provided information about the angle, speed and position of the hammer, which provided time, force and velocity data. For the calculation of the impact energy absorbed during deformation at each temperature, the area under the force vs. displacement curve was calculated. In order to compare the deformation velocity at each temperature, the change in displacement over time was calculated to determine the average deformation velocity for each temperature, and the corresponding results are tabulated in Table 6.1.

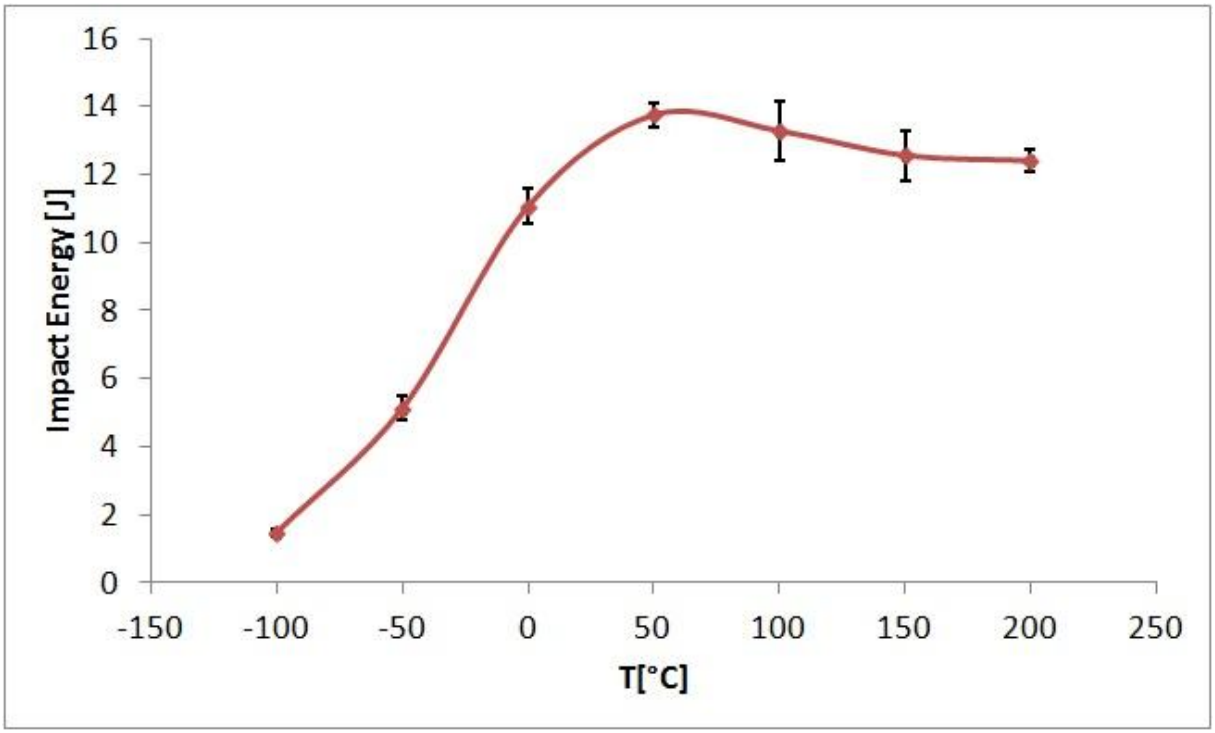


**Figure 6.1.** Impact energy – temperature curve for the austenitic high-manganese steel investigated in this study. Error bars represent standard deviation of three measurements at a given temperature [1].

**Table 6.1.** Average deformation velocities for samples deformed at various temperatures [1].

| Temperature (°C) | Deformation Velocity (m/s) |
|---|---|
| 200 | 3.39 |
| 150 | 3.47 |
| 100 | 3.37 |
| 50 | 3.44 |
| 0 | 3.40 |
| -50 | 3.63 |
| -100 | 3.75 |

Prior to the impact experiments, the samples were examined via SEM in order to observe the microstructure of the as-received material. The SEM images of the as-is specimens did not show the presence of any remarkable microstructural features except for some traces of surface preparation processes, which imply that any new structure observed in the SEM images of the tested specimens stems from the impact deformation. Following the experiments, both SEM and TEM were employed in order to monitor the relative slip and twin activities.

SEM investigations were carried out on a field emission scanning electron microscope. For TEM work, in order to observe the microstructure of the failure zone, following SEM analysis, a 50-100 μm layer of material was removed parallel to the crack surfaces, and the foils were extracted from these new surfaces: the approximate TEM foil extraction locations are indicated with green lines in Figures 6.2-6.5. The TEM foils were in the form of flat disks with a thickness of approximately 250 μm. These disks were then mechanically thinned down to 80 μm, and in order to obtain large electron-transparent areas, electropolished on both sides by conventional twin-jet electropolishing with an electrolyte consisting of 100 ml 40 % perchloric acid, 500 ml butoxyethanol and 400 ml 100 % acetic acid. The electropolishing was carried out at -20 °C under an acceleration voltage of 20.5 V, and two-beam imaging conditions were used whenever possible. All TEM investigations were conducted utilizing a TEM equipped with a 200 kV electron gun.

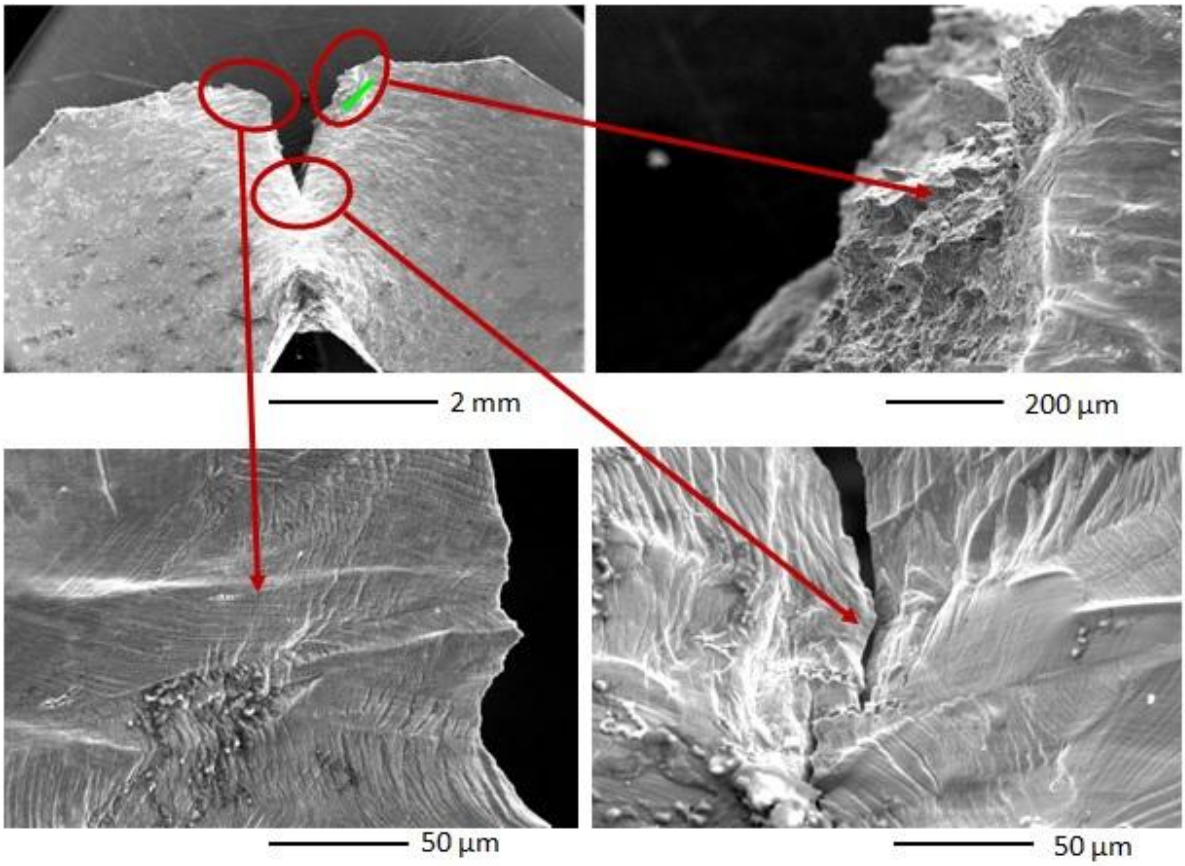


**Figure 6.2.** SEM images showing traces of extensive plastic deformation on the crack surface of the sample tested at 200 °C. The red circles indicate the locations of SEM investigations while the green line shows the approximate locations where the TEM foils were extracted from [1].

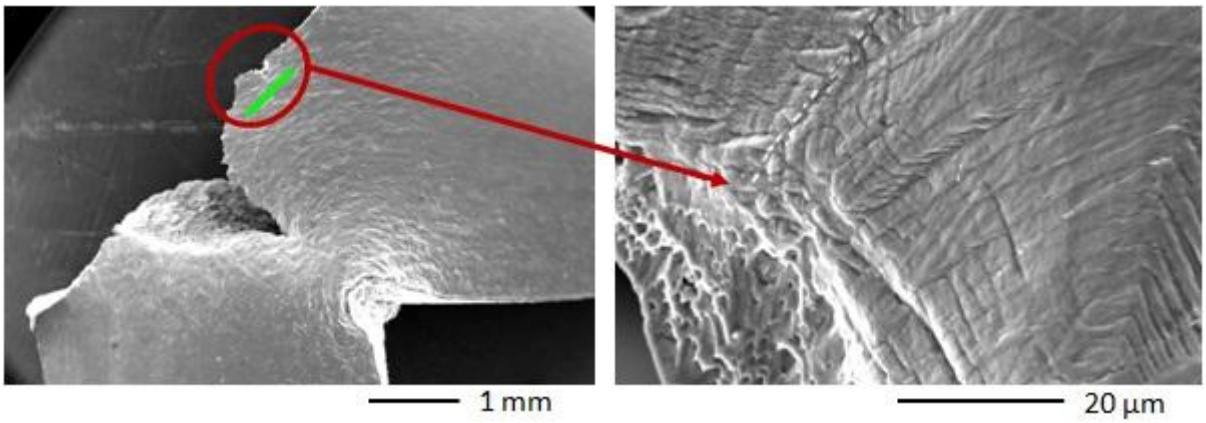


**Figure 6.3.** SEM images showing traces of plastic deformation on the crack surface of the sample impact tested at 50 °C. The red circles indicate the locations of SEM investigations while the green line shows the approximate locations where the TEM foils were extracted from [1].

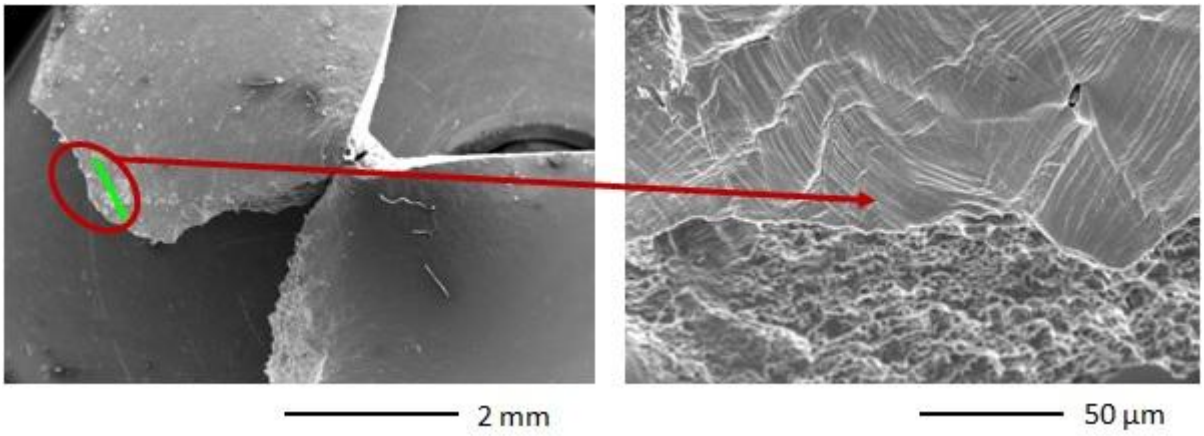


**Figure 6.4.** SEM images showing traces of plastic deformation on the crack surface the sample tested at 0 °C. The red circles indicate the locations of SEM investigations while the green line shows the approximate locations where the TEM foils were extracted from [1].

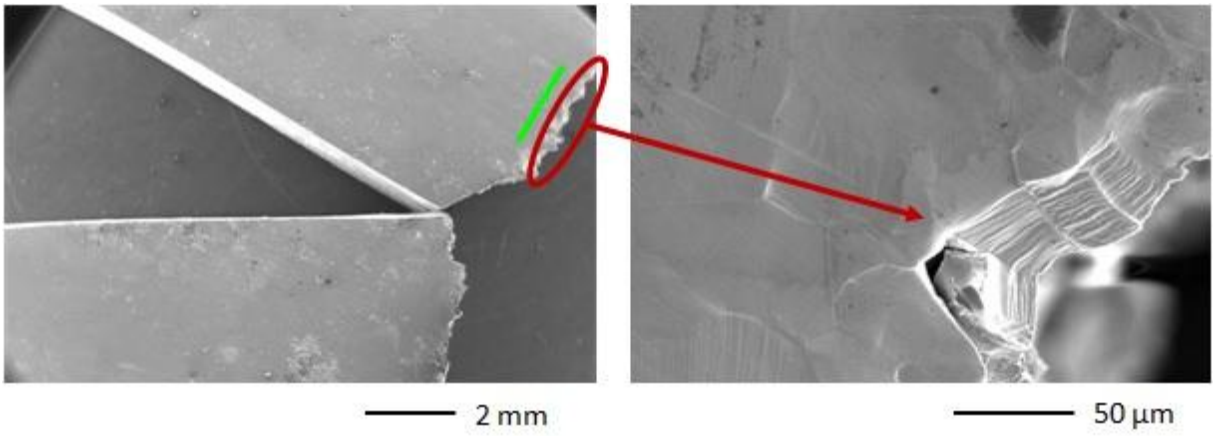


**Figure 6.5.** SEM images showing traces of plastic deformation on the crack surface the sample tested at -100 °C. The red circles indicate the locations of SEM investigations while the green line shows the approximate locations where the TEM foils were extracted from [1].

## 6.3 Results and Discussion

The impact energy – temperature curve for the current austenitic high-manganese steel is presented in Figure 6.1. Accordingly, the material exhibits a typical ductile-to-brittle transition curve between -100 and 50 °C, and a DBTT between -50 and 0 °C. Furthermore, as the temperature exceeds 50 °C, energy absorption seems to decrease slightly. SEM analysis of the samples subjected to impact loading at elevated temperatures (50 and 200 °C) revealed slip lines of extensive plastic deformation in these samples (Figures 6.2 and 6.3). Specifically, these samples were torn from the notch tip to some extent due to the impact loading, rather

than being broken into two separate pieces. The traces of plastic deformation are more significant around these unseparated regions, where crack propagation came to an end (Figures 6.2 and 6.3). These traces indicate that the high-temperature samples dissipated the absorbed energy during loading by extensive plastic deformation, and specifically through dense dislocation activity, resisting crack propagation. This argument is supported by the relatively large dislocation densities observed in the microstructures of samples subjected to impact loading at 50 and 200 °C, as evidenced by the TEM images provided in Figure 6.6. In the separated regions, the observed structure assumes a form similar to the cup-and-cone shape, which is common in ductile tension samples [20]. Thus, Figures 6.2 and 6.3 evidence the ductility of samples tested at elevated temperatures (50 and 200 °C). At higher magnifications, a granular structure can be observed on the cup-and-cone-like regions (Figures 6.2 and 6.3), the size of which decreases with decreasing temperature (Figures 6.2-6.5). Furthermore, the length of the unseparated regions decrease with decreasing temperature, and at very low temperatures (e.g., -100 °C) the samples are broken into two separate pieces (Figure 6.5).

The traces of slip activity are not restricted to the fracture surfaces, but are prevalent throughout the specimens tested at 0, 50 and 200 °C, demonstrating the dominance of the slip mechanism throughout the microstructure (Figures 6.2-6.4). Indeed, traces of slip activity become denser concomitant with increasing temperature (Figures 6.2-6.5), supporting the observed more ductile behavior of the samples subjected to impact loading at higher temperatures (Figure 6.1). Moreover, the slip lines visible under the SEM become more localized and more commonly located in smaller zones rather than spreading over larger volumes, with decreasing temperature (Figures 6.2-6.5). This is an indication of the fact that enhanced twinning promoted at lower temperatures hinders glide dislocation mobility and restricts slip activity, leading to a more brittle behavior at the same time (Figure 6.1). The

major source of the observed behavior is the change in temperature, such that the expected softening at elevated temperatures promotes a ductile behavior. In addition, the competition between the two major micro deformation mechanisms observed in this class of steels, i.e. slip and twinning, demonstrates a significant dependence on temperature. Specifically, as the temperature increases, there is less interaction between glide dislocations and twins, leading to enhanced energy absorption by dislocation glide [7, 12].

In order to focus on the slip and twin activities associated with failure of the samples, TEM foils were extracted directly from the crack zone, as indicated by the green lines in Figures 6.2-6.5. A detailed examination of the microstructure by TEM revealed evidence supporting the above arguments. Specifically, both twinning and dislocation slip were active at all temperatures, and the twin activity increased with decreasing temperature, as expected for this class of steels (Figures 6.7-6.9). An interesting observation is that even though twin density is lower at elevated temperatures, there is a significant increase in the length of individual twins at these temperatures. In particular, individual twins as long as 40 μm were prevalent upon impact loading at 200 °C (Figure 6.7), while this length decreased to 30 μm at 0 °C and 15 μm at -100 °C. This is associated with the fact that the deformation mechanism at elevated temperatures favors slip over twinning [7, 12], such that the twins that had already nucleated continue to grow since the stress relief caused by the increased temperature prevents the local stress levels from reaching that necessary for formation of new twins (Figure 6.10) [6, 7, 13]. Another factor leading to this behavior is the increase in SFE at elevated temperatures. The high SFE prevents the partition of twins and dislocations, and thus, instead of partial dislocations and short twins, formation of perfect dislocations and long twins are promoted (Figures 6.7 and 6.10) [3, 4, 8]. An important observation is that, despite the decreasing twin length with decreasing temperature, twin activity is significantly enhanced at lower temperatures (Figures 6.7-6.10), mainly owing to the increasing twin

density at these temperatures. As a result of systematic TEM observations, it was noted that about 58%, 24% and 19% of the grains featured twins and micro-twins in the samples deformed at 200 °C, 0 °C and -100 °C, respectively. Please note that the percentage of grains exhibiting twinning are provided rather than the twin volume fractions, since it is impractical to accurately quantify a twin volume fraction for each sample utilizing TEM. Furthermore, lower temperatures promote the formation of micro twins within the already twinned regions (Figures 6.8-6.10), leading to increased overall twin density. In face-centered cubic (fcc) materials twinning commonly occurs on {111} planes [21, 22]. However, as it is evidenced by the results of the TEM trace analyses of the 0 °C and -100 °C samples, the newly formed micro-twins grew on different planes than the {111} plane. Previous studies already indicated that planes other than {111} may play a role for twinning in fcc materials [23]. Such micro-twins, which form within the already twinned regions with other orientations than the primary twin, are referred to as second-order twins [22], and since they form on different crystallographic planes and possess different orientations (Figures 6.8-6.9), they are capable of restricting glide dislocation activity along multiple directions (Figure 6.10). As dislocation motion on multiple paths is hindered, dislocation pile-ups form in the vicinity of these micro-twins (Figure 6.11), which further prevents the glide dislocation activity. This multidirectional and intense restriction of glide dislocation activity (Figure 6.10), contributed to the observed brittle behavior at low temperatures (Figure 6.1). Thus, brittleness, which is already expected at low temperatures, is promoted further for the 0 °C and -100 °C samples, with the formation of micro-twins with various orientations (Figures 6.8-6.10).

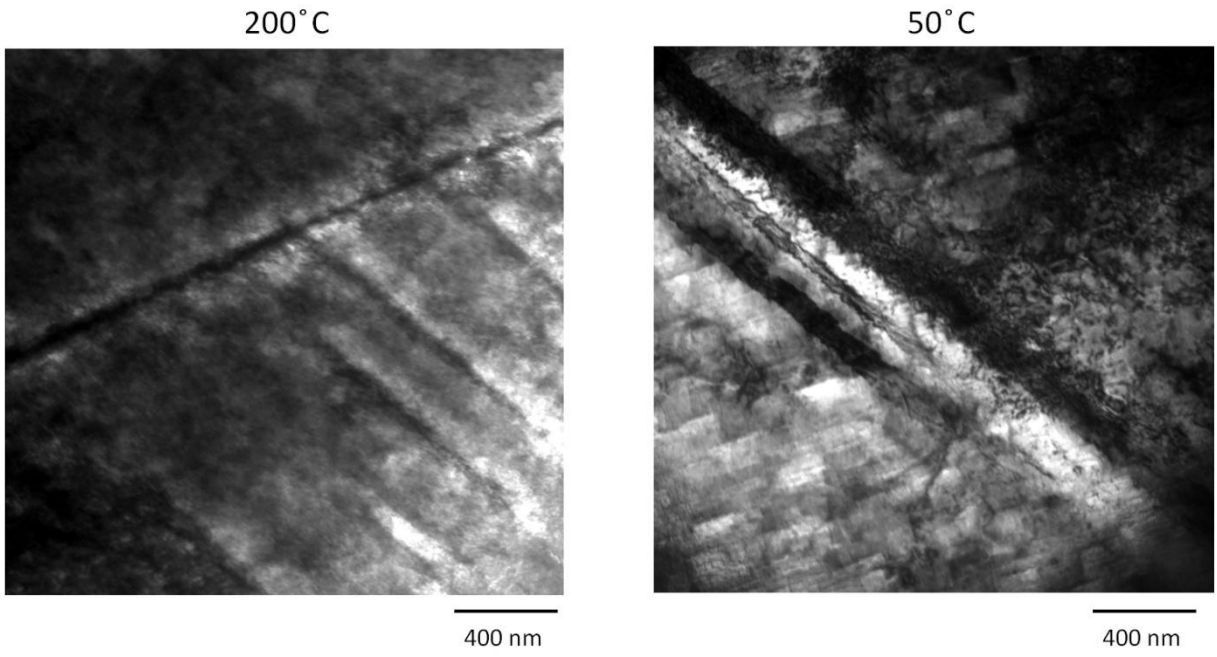


**Figure 6.6.** TEM images demonstrating the dense dislocation activity in samples subjected to impact loading at 50 and 200 °C upon failure [1].

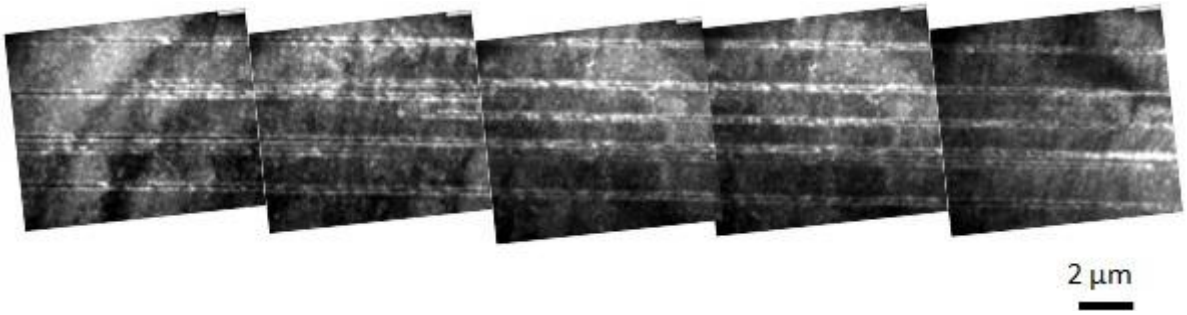


**Figure 6.7.** Composite of TEM images showing extended twins evident in the sample tested at 200 °C [1].

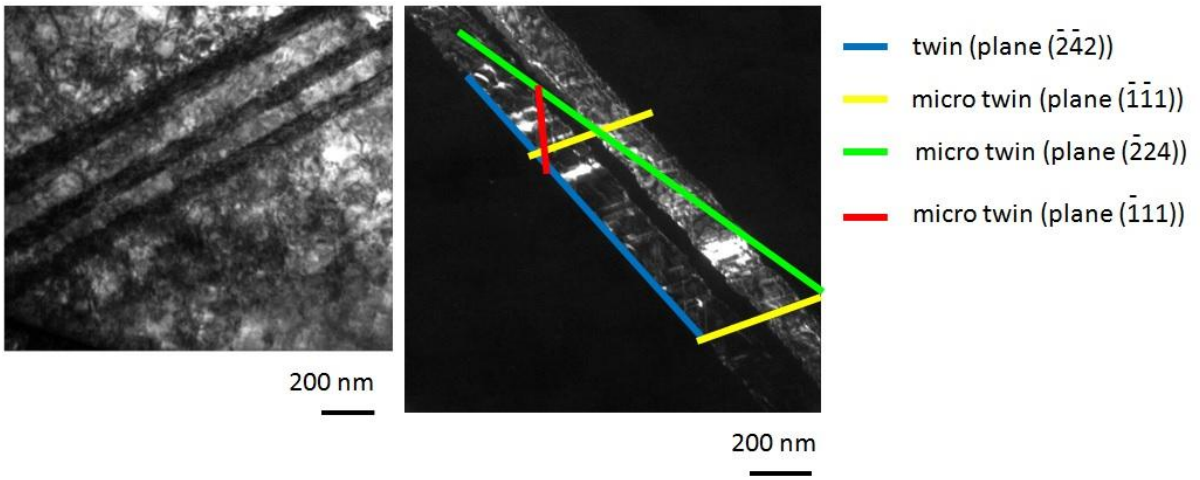


**Figure 6.8.** TEM images showing twins, and micro-twins located on various crystallographic planes inside larger twins in the sample upon impact loading at 0 °C. Note that the images do not show the full length of the twins. The bright-field image shows twins and dislocations, whereas the micro-twins are more visible in the dark-field images, such as the one shown on the right hand side [1].

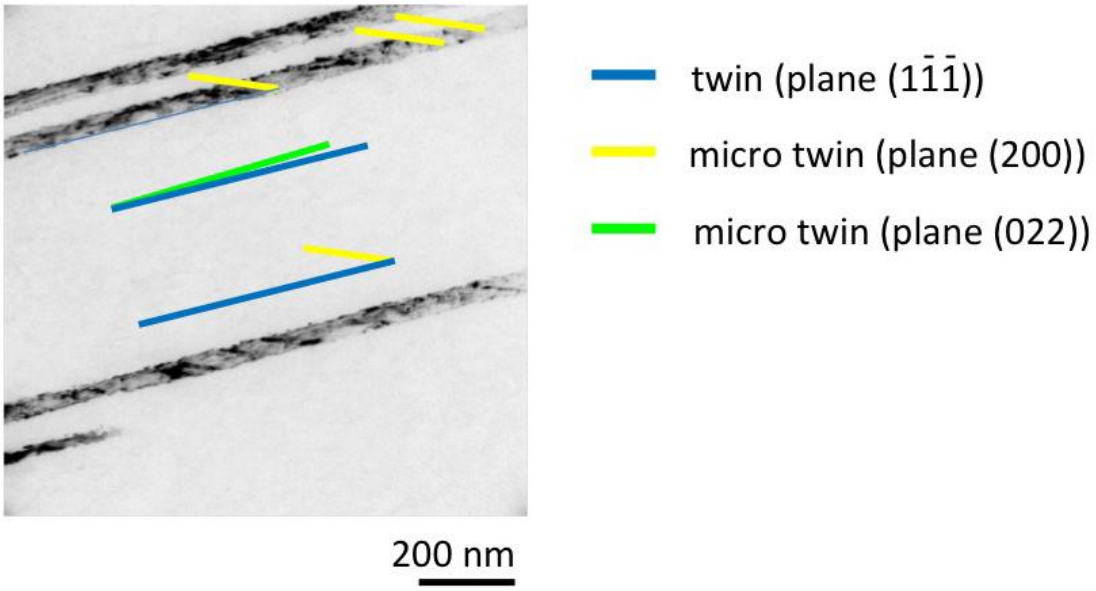


**Figure 6.9.** TEM dark-field image showing the presence of twins, and micro-twins located on various crystallographic planes inside larger twins in the sample deformed at -100 °C. Note that the contrast of the image has been inverted to better bring out the micro-twins [1].

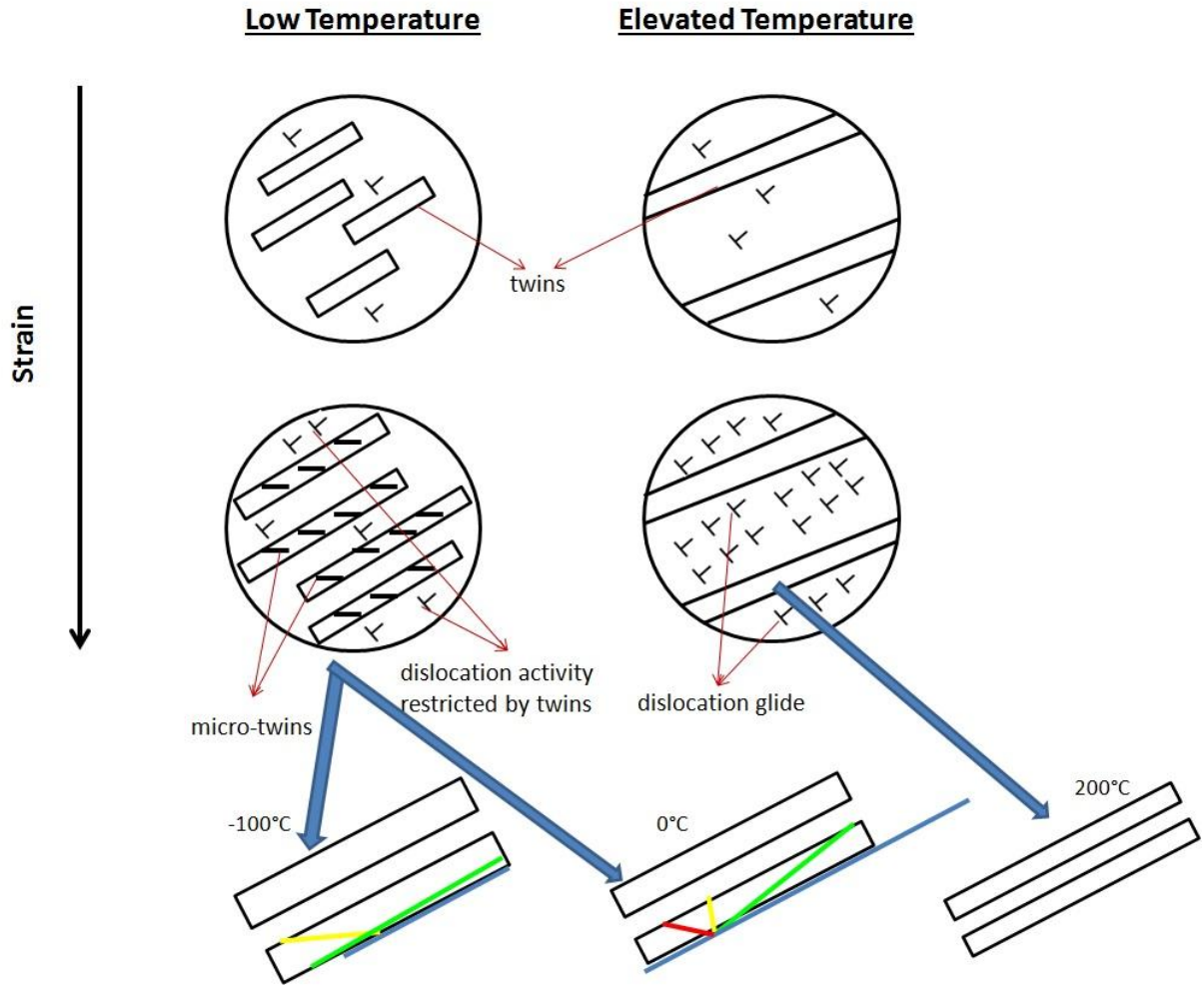


**Figure 6.10.** Schematic summarizing the relative slip and twin activities, and the dependence of twin length and density, and dislocation density and activity on temperature [1].

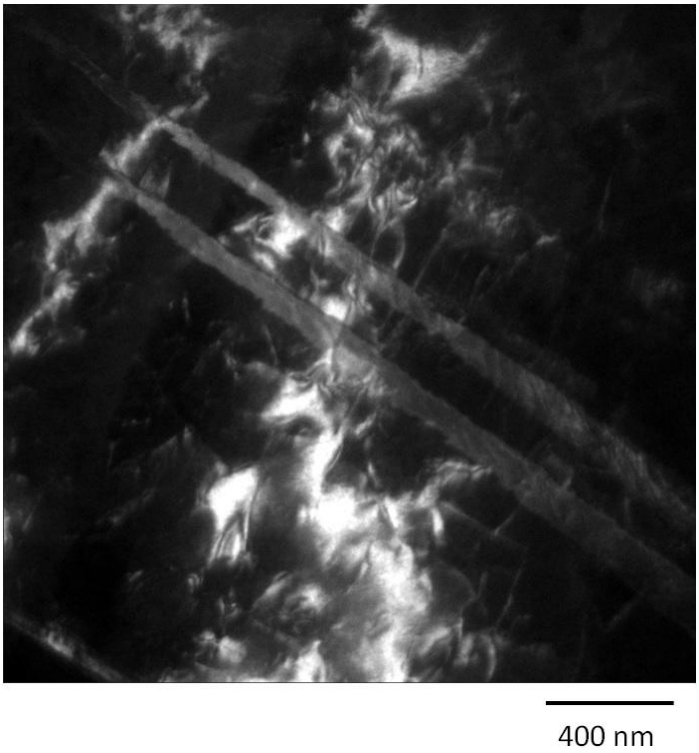


**Figure 6.11.** Weak beam TEM image demonstrating the dislocation pile-ups around micro-twins in the sample deformed at 0 °C [1].

It is important to note that both this restricted dislocation activity and twin formation are quite similar in the microstructures of 0 °C and -100 °C samples upon impact loading, based on the TEM results (Figures 6.8-6.10). However; the -100 °C sample was still much more brittle compared to the one tested at 0 °C. This can be explained with the fact that the same twin density is reached faster, i.e. at a lower strain level, at -100 °C, leaving more room for individual dislocation – twin interactions. Since the dislocation motion is hindered by the existing twins and micro twins, individual dislocations come across twins more frequently, and this increased dislocation-twin interaction contributes more to the hardening in the microstructure in the -100 °C sample, leading to the brittle fracture. This can be observed in both impact energy and fracture surface of this sample (Figures 6.1 and 6.5).

Deformation velocity calculations for the samples deformed at different temperatures (Table 6.1) revealed that deformation velocity was high at all temperatures, which is not unexpected considering that impact is a very rapid process taking place at high strain rates

[16, 18]. However, when the deformation velocities at each temperature were compared to each other, it was observed that the deformation velocity was slightly higher at low temperatures compared to those at elevated temperatures (Table 6.1). This is a reasonable and expected result, since the samples tested at low temperatures exhibit a brittle fracture, which requires relatively lower energy absorption, and thus, occurs within a shorter time span. Similarly, the fracture at elevated temperatures, which is more ductile and absorbs more energy, is expected to occur within a slightly longer period of time, as evidenced by the deformation velocity data (Table 6.1).

Previous work has demonstrated that high-manganese austenitic steels owe their unusually high strain hardening capacity under tensile or compressive loading to slip-twin interaction [11, 13]. However, the current findings clearly evidence that only one deformation mechanism dominates under impact loading, which leads to a much more complicated stress-strain distribution throughout the sample as compared to the aforementioned modes of loading. Furthermore, the temperature dictates the parameters specific to the dominant mechanism, such as twin volume fraction, twin thickness and length, or glide dislocation density. The reason for the unexpected dominance of only one mechanism under impact loading is attributed to the rapid deformation: very high strain rates are attained during impact loading in comparison to classical loading modes, and the corresponding rapid failure of the sample leaves very little room for slip-twin interaction that can significantly affect the overall deformation response. Furthermore, it is well known that this class of steels exhibit notable strain rate sensitivity, such that either slip or twinning dominates at high strain rates even under tensile or compressive loading [24]. Consequently, the impact testing emerges as a promising means for shedding light onto the complicated microstructural activities dictating the overall deformation response of high-manganese austenitic steels.

## 6.4 Conclusion

The relative contributions of slip, twinning, and slip-twin interaction to the deformation response of an austenitic high-manganese steel were investigated under impact loading. Impact experiments were carried out at seven different temperatures within the range of -100 °C to 200 °C, and the corresponding microstructure evolution was characterized by thorough post-experimental transmission electron microscopy and scanning electron microscopy analyses. The current findings show that only one mechanism dictates the deformation response to impact loading, as opposed to the slip-twin interactions typically observed in high-manganese austenitic steels under tension or compression. Specifically, at elevated temperatures slip is the main deformation mechanism, while slip activity is restricted by enhanced twinning at low temperatures. In the case of twinning, micro-twins on three different secondary planes than the primary {111} twin plane in face-centered cubic crystals prevail, further contributing to the brittle behavior by strengthening the primary twins. Moreover, parameters specific to the active deformation mechanism, such as twin volume fraction, twin thickness and length, or glide dislocation density, strongly depend on temperature. The reason for the enhanced activity of only one mechanism rather than the slip-twin interaction is associated with the high-strain rate deformation taking place under impact loading, which does not allow for significant interaction of the two mechanisms. Overall, the current results indicate that loading conditions, such as deformation velocity and deformation temperature, constitute critical parameters dictating the dominant deformation mechanism, and thus, the corresponding mechanical response of high manganese austenitic steels. The current findings not only lay out the impact response of this class of steels for a wide temperature range, but also constitute the first set of results shedding light on the slip-twin competition in these materials under impact loading. The dominant deformation mechanism is dictated by temperature, which also significantly influences the dislocation density, and both

the length and volume fraction of twins in the microstructure. The important finding is that impact loading promotes either slip or twinning as the major deformation mechanism, as opposed to the common slip-twin interaction under uniaxial tensile or compressive loading. Furthermore, as the current evidence suggests that only one mechanism dominates under impact loading, this type of testing can be utilized for shedding light onto the complicated deformation mechanism of this class of steels in future work.

## 6.5 References


[1] S.M. Toker, D. Canadinç, A. Taube, G. Gerstein, H.J. Maier, Mater. Sci. Eng. A 593 (2014) 120–126.

[2] W. S. Owen, M. Grujicic Acta Mater. 47 (1) (1999) 111-126.

[3] O. Bouaziz, S. Allain, C.P. Scott, P. Cugy, D. Barbier, Curr. Opin. Solid State Mater. Sci, 15 (2011) 141-168.

[4] E. Bayraktar, F. A. Khalid, C. Levaillant, J. Mater. Process. Tech. 147 (2004) 145-154.

[5] T. Niendorf, F. Rubitschek, H.J. Maier, J. Niendorf, H.A. Richard, A. Frehn, Mater. Sci. Eng. A 527 (2010) 2412-2417.

[6] T. Niendorf, C. Lotze, D. Canadinc, A. Frehn, H.J. Maier, Mater. Sci. Eng. A 499 (2009) 518-524.

[7] I. Karaman, H. Sehitoglu, K. Gall, Y. I. Chumlyakov, H. J. Maıer, Acta Mater. 48 (2000) 1345-1359.

[8] I. Karaman, H. Sehitoglu, Y.I. Chumlyakov, H.J. Maier, I.V. Kireeva, Scripta Mater. 44 (2001) 337-343.

[9] R. Ueji, N. Tsuchida, D. Terada, N. Tsuji, Y. Tanaka, A. Takemura, K. Kunishige, Scripta Mater. 59 (2008) 963-966.

[10] B. Hutchinson, N. Ridley, Scripta Mater. 55 (2006) 299-302.

[11] D. Canadinc, H. Sehitoglu, H.J. Maier, D. Niklasch, Y.I. Chumlyakov, Int. J. Solids Struct. 44 (2007) 34-50.

[12] H. Beladi, I.B. Timokhina, Y. Estrin, J. Kim, B.C. De Cooman, S.K. Kim, Acta Mater. 59 (2011) 7787-7799.

[13] I. Karaman, H. Sehitoglu, A. J. Beaudoin, Y. I. Chumlyakov, H. J. Maier, C. N. Tome, Acta Mater. 48 (2000) 2031-2047.

[14] S. Allain, J.-P. Chateau, D. Dahmoun, O. Bouaziz, Mater. Sci. Eng. A (387–389) (2004) 272-276.

[15] S. Sato, E.-P. Kwon, M.I, Kazuaki Wagatsuma, S. Suzuki, Mater. Characterization 62 (2011) 781-788.

[16] W.-S. Lee, T.-H. Chen, Proc. Instn. Mech. Engrs. C 216 (2002) 971-982.

[17] Z.-M. He, Q.-C. Jiang, S.-B. Fu, J.-P. Xie, Wear 120 (1982) 305-319.

[18] L. Da-zhao, W. Ying-hui , L Chun-yue, H.Li-feng, L. Dong-Ieng, Xian-zhe, J. Iron Steel Res. Int. 17(6) (2010) 67-73.

[19] J.W. Morris, Jr. Sci. 320 (2008) 1022-1023.

[20] I. Scheider, W. Brocks, Eng. Fracture Mech. 70 (2003) 1943-1961.

[21] C. Efstathiou, H. Sehitoglu, Acta Mater. 58 (2010) 1479–1488.

[22] S. Kibey, J.B. Liu, D.D. Johnson, H. Sehitoglu, Appl. Physics Letters 91 (2007) 181916-1-3.

[23] J.W. Christian, S. Mahajan, Prog. Mater. Sci. 39 (1995) 1-157.

[24] D. Canadinc, C. Efstathiou, H. Sehitoglu, Scripta Mater. 59 (2008) 1103-1106.

# 7 CHAPTER 7: CONCLUSIONS AND FUTURE WORK

## 7.1 Conclusions

The motivation of the work presented herein was investigating the biocompatibility of metallic materials by constructing a relationship between their biocompatibility, microstructure and mechanical properties. For this purpose, conventional and potential biomedical alloys, and structural metallic materials were brought under focus and analyzed in terms of their microstructures, surface and mechanical properties utilizing various experiments, which simulated clinical conditions in terms of chemical and mechanical properties. The findings of these analyses were used for understanding the effect of microstructure on biocompatibility and mechanical properties of the target materials and establish a correlation between these properties.

First, biocompatibility of NiTi SMAs was investigated based on their geometry and body location dependency. Specifically, static immersion experiments were conducted on NiTi SMAs with three different geometries, in three fluids simulating different body parts. Following the experiments, the alloys and fluids were separately analyzed for investigating the ion release and new structure formation during the immersion procedure (Chapter 2). This analysis showed that different surface properties, which are dictated by the processing methods applied to obtain different geometries, strongly influence the alloy behavior in each fluid. Moreover, each different geometry appears to be safer in different body fluids, which indicates that certain geometries are safer for certain body parts.

Next, NiTi SMAs utilized for another application, namely the orthodontic archwires, were brought under focus and analyzed in terms of the biocompatibility testing method utilized to evaluate their biocompatibility. Specifically, *ex situ* static immersion experiments were applied to NiTi orthodontic archwires in artifical saliva. These archwires were then

compared to companion wires that were subjected to actual intraoral conditions (Chapter 3). The following analysis showed that, although static immersion experiments provide important information about events taking place during exposure to artificial saliva and a successful simulation to some extent, the phenomena occurring as a result of the mechanical contact between wires and brackets in actual intraoral environment could not be simulated. These results indicated that, for a more realistic simulation of the clinical intraoral conditions during biocompatibility analysis of orthodontic archwires, the actual conditions should be simulated in terms of both chemical and physical parameters, where mechanical contact of wires and brackets are also present.

This chapter of the study was followed by the incorporation of mechanical loading conditions into *ex situ* testing of NiTi orthodontic archwires. Specifically, a NiTi archwire was bound to brackets on a dental mold and immersed in artifical saliva, which was then compared to an unbound and immersed companion archwire (Chapter 4). The observation of the undeformed and bound archwire surfaces following immersion experiments demonstrated that wire-bracket contact points constitute critical regions for the accumulation of corrosion products due to the stress concentration and stress assisted corrosion at these spots. Therefore, corrosion product formation behavior on the bound wire significantly differed from that of the undefromed wire. Moreover, the preferential new structure pile-up at the wire-bracket contact points on the deformed wire showed that actual intraoral conditions that orthodontic archwires are exposed to can be successfully simulated by providing the wire-bracket contact. The corresponding results evidenced the importance of incorporation of actual loading conditions into the biocompatibility testing environment, in addition to appropriate chemical conditions, for a more realistic and successful simulation of the clinical conditions.

The current chemical investigations on the biocompatibility of NiTi SMAs have demonstrated that processing, and texture and anisotropy of the alloy have a strong influence

on biocompatibility. Therefore, in order to gain a deeper understanding of the mechanical property-biocompatibility relationship of metallic biomaterials, and in particular the role of the anisotropy on the mechanical performance of biomedical alloys, a potential biomedical alloy, namely the Niobium-Zirconium (NbZr) alloy, was also investigated in the current study. As impact loading is a critical type of loading that implant materials can encounter in the case of jumping or falling, it is crucial to investigate this type of loading for potential implant materials. With this purpose, the impact response of coarse grained and ultrafine-grained (UFG) NbZr alloys with different degrees of anisotropy were investigated under various temperatures (Chapter 5). The obtained results suggested that, impact behavior of the potentially biomedical UFG NbZr alloys is strongly dependent on anisotropy and this property can be utilized in designing implants with proper anisotropy to withstand anticipated loads in various directions. This investigation also showed that, impact response of metallic materials is strongly dependent on microstructure.

Following this analysis, in order to further investigate the microstructure-mechanical response relationship of metallic materials, the impact behavior of a conventional metallic material, a high-manganese austenitic steel, was examined at various temperatures (Chapter 6). Since high manganese austenitic steels constitute an important type of structural metallic material with a complex microstructure involving slip-twin interactions, their investigation provided comprehensive information about the role of microstructure on impact response. The outcomes of this investigation showed that, under impact loading, depending on the temperature, only slip or twin mechanism dictates the overall deformation response, rather than the slip-twin interactions that normally takes place during the deformation of high manganese austenitic steels under tensile or compressive loads. This finding is correlated with the high strain rate of deformation under impact loading and lays out the importance of

loading conditions on the microstructural interactions and consequently mechanical response of metallic materials.

Overall, the current study demonstrated that biocompatibility of metallic materials is strongly dependent on microstructure and mechanical properties. Moreover, the results presented herein emphasize the importance of biocompatibility testing under realistic conditions where both chemical and mechanical loading scenarios resemble the actual ones. Consequently, understanding the biocompatibility-microstructure-mechanical property relationship of biomaterials becomes of utmost importance especially when designing new implants.

## 7.2 Future Work

Part of the current study revealed that surface properties are deterministic for the biocompatibility of implant materials, and by modifying the surface cell attachment and tissue growth can be promoted on the implant surface. The new evidence provided in this thesis shows that microstructure has a significant effect on the surface properties, which is eventually expected to affect cell response on the metal surface. With this motivation we have already started to investigate the cell attachment behavior on different metal surfaces, which possess different deformation histories, and thus, exhibit different microstructures. Accordingly, the follow-up work based on this thesis aims to establish the effect of microstructural interactions in metals on the cell response to metal surfaces.